ZORAN CENEV

DESIGN AND IMPLEMENTATION OF DOUBLE H'-GANTRY MANIPULATOR FOR TUT MICROFACTORY CONCEPT

MASTER OF SCIENCE THESIS

ABSTRACT

TAMPERE UNIVERSITY OF TECHNOLOGY
Master's Degree Program in Machine Automation
ZORAN, CENEV: Design and implementation of double H'-gantry manipulator for TUT microfactory concept
Master of Science Thesis, 75 pages, 14 appendices (27 pages)
February 2014
Major: Mechatronics and micromachines
Examiners: Professor Reijo Tuokko, Professor Pasi Kallio
Keywords: double H'-gantry, manipulator, microfactory, design, implementation.

This Master of Science thesis depicts the mechanical design and physical implementation of double H'-gantry manipulator called DOHMAN. The H'-gantry mechanism is belt driven, two dimensional positioning device in which the belt is arranged in capital "H" form, and enables one linear and one rotary movement. The Ball-Screw Spline, in addition, is mechanism that consists of Ball Screw Nut, Ball Spline Nut, and Lead Screw with screw and spline grooves that fit both nuts. This mechanism enables linear and rotary displacement along the same axis. The DOHMAN robot is made of two parallel kinematic H'-gantry structures linked with a miniature Ball Screw-Spline mechanism. The resulting structure is capable of performing four degrees-of-freedom (DOF) displacements along the three Cartesian axes X, Y and Z as well as a rotation W around the Z axis. The size and the other geometries of the DOHMAN robot aim to fit into the microfactory concept (TUT-µF) developed at Tampere University of Technology.

For position control and visual servoing of the robot, an additional module was designed and implemented. Custom design of mechanical parts along with the selection of off-the-shelf components was done for building the robot prototype. The chapters and the appendix of this thesis thoroughly explain the design decisions and the implementation. During the design development a new innovative homing strategy for linear Z and angular W axes was suggested and later implemented. This innovative homing provides efficient use of space for mounting the limit switches, avoiding huge loss in the overall Z-axis movement, and significantly reduces the cabling issues in the moving structure. Besides the innovative homing, other advantages of DOHMAN are distributed actuation and homogeneous workspace. The distributed actuation decreases the overall mass of the moving structure and also reduces the cabling within the overall mechanical system. The consistency in the workspace eases the control of the robot because there are no regions to avoid while moving the end effector.

PREFACE

I joined the Microfactory RG as research assistant in May 2012. At first, my tasks were mainly concerned with design and implementation of machine vision based quality control systems, and mechanical design and prototyping of various devices for research and/or educational purposes. During this time, I was very satisfied from the supervision of Timo Prusi as well as from the collaborative and supportive working environment in the research group as a whole. In March 2013, I started to work on this M.Sc. thesis and due to the interdisciplinary nature of the project, the supervision was spread among three people, i.e. Riku, Timo and Niko. Riku was in charge for mechanical design, manufacturing and ordering of all mechanical parts. The machine vision and writing related issues were supervised by Timo, whereas Niko supervised my work in design and implementation of the controls along with the kinematic modeling and drive dimensioning.

During the whole development phase of the DOHMAN robot, I had the opportunity to learn a complete R&D procedure in robot development as well as gain significant hands-on experience in lab work by operating tools and machines, electronics installations, fast prototyping by utilizing 3D printer, implementing control algorithms, and so on. I greatly enjoyed each phase of the robot development. Although there were tough and mind-blowing moments, I consider this M.Sc. thesis as one of my greatest accomplishments. The DOHMAN project was not only an aim but rather a journey, a journey that I certainly enjoyed to be part of.

This M.Sc. thesis is dedicated to my parents Metodija and Aneta Cenevi.

Tampere, February 2014
ZORAN CENEV

TABLE OF CONTENTS

LIST OF ABBEVIATIONS AND NOTATIONS

3D	Three dimensional
AC-DESK	Adaptive and Collaborative Desktop Factory
Big pulley	Pulley attached either to the screw nut or to the spline nut within the Ball Screw-Spline mechanism.
BM	Base Module
BSS	Ball Screw-Spline
CAD	Computer Aided Design
CAE	Computer Aided Engineering
CNC	Computer Numerical Control
CSEM[1]	Swiss Centre for Electronics and Microtechnology
CVM	Control and Vision Module
CW	Clockwise
DOF	Degrees Of Freedom
DOHMAN	DOuble *H'*-gantry MANipulator, short name of the developed manipulator
EPFL[1]	École Polytechnique Fédérale de Lausanne
et al.[2]	"And others" (et alii)[2], used in referencing a publication with more than two authors
HMI	Human Machine Interface

---

[1] French Abbreviation
[2] Latin Abbreviation

HW	Hardware
i.e.[2]	"That is"
IP	Internet Protocol
IWF[3]	Institute of Machine Tools and Production Technology at the Technical University of Braunschweig
KIT	Karlsruhe Institute of Technology
LSRO	Laboratory of Robotic Systems
MEIS	Mechanical Engineering and Industrial Systems.
MEMS	Microelectromechanical system
micro/meso scale	10 to 10^4 μm scale
minirail	Profiled miniature guideway, a product of Schneeberger GmbH
miniscale	Miniature guideway with integrated measuring system, a product of Schneeberger GmbH
NC	Numerical Control
PID	Proportional-Integral-Derivative control that refers to a generic control loop with feedback link.
PLC	Programming Logic Controller
Plug and play	Specification which refers to automatic discovery of a hardware component in a system, meaning that there is no need for physical device configuration or user intervention such as installing drivers or setting connections via IP addresses.
PM	Process Module
R&D	Research and Development
RG	Research Group

---

[3] German Abbreviation

SCARA	Selective Compliance Articulated/Assembly Robot Arm
Small pulley	Pulley that refer to either a driving or idle pulley. The pulley has same diameter/radius in both cases.
SW	Software
TCP	Tool Center Point
TEKES[4]	Finnish Funding Agency for Technology and Innovation
TUT	Tampere University of Technology
TUT µF	A concept of microfactory developed at Tampere University of Technology (TUT)
UV	Ultraviolet
WP	Work Package
µ	Micro, one millionth
µF	Micro-factory or microfactory

---

[4] Finnish Abbreviation

LIST OF SYMBOLS

$C_{LH}{}'$	Minimum overall circumference of the lower H-like belt structure.
$C_{ML1}{}'$	Circumference of the first middle belt with margins.
$C_{ML2}{}'$	Circumference of the second middle belt with margins.
$C_{UH}{}'$	Maximum overall circumference of the upper H-like belt structure.
h_{sen}	Height of the camera detector.
A_d	Initial direct kinematic matrix (4x4) in which $a_{d11}, a_{d12}, \dots, a_{d44}$ are members of the matrix.
C_{LH}	Overall circumference of the lower H-like belt structure.
C_{ML1}	Circumference of the first middle belt.
C_{ML2}	Circumference of the second middle belt.
C_{UH}	Overall circumference of the upper H-like belt structure.
C_{bp}	Effective circumference of big pulleys.
C_{bp}	Effective circumference of small (idle and driving) pulleys.
F_{IO}	Real data acquisition frequency of the EL5101 digital pulsed input module.
F_{IO_min}	Minimum required data acquisition frequency of the EL5101 digital pulsed input module.
F_{sensor_max}	Maximum frequency of the selected linear encoder.
F_u	Tensile load.
F_z	Vertical force for pulling the load in vertical Z direction.
H_{FOV}	Height of the field-of-view.
J_B	Inertia of the 1524 *mm* long belt.
J_{BP}	Inertia of the big pulley.
J_{BSS}	Inertia of the BSS.

J_{GH}	Inertia of the gearhead.
J_M	Inertia of the motor.
J_{ML}	Inertia of the moving load.
J_{SP}	Inertia of the small pulley.
J_T	Total moment of inertia.
K_s	Safety factor.
M_d	Final direct kinematic matrix (4x4).
R_W	Angular resolution along W axis.
R_X	Linear resolution along X axis.
R_Y	Linear resolution along Y axis.
R_Z	Linear resolution along Z axis.
T_L	Load torque.
T_a	Acceleration torque.
T_{dg}	Final computed driving torque for each motor.
T_{dg1}	Driving torque of each motor for case 1 (Section 3.6.1).
T_{dg1_total}	Total driving torque of both driving gears for case 1.
T_{dg2}	Driving torque of each motor for case 2 (Section 3.6.2).
T_{dg2_total}	Total driving torque of all driving gears for case 2.
T_y	Cumulative motor torque.
T_z	Required torque on the Screw Nut for obtaining F_z.
$V_{X\,max}$	Maximum linear velocity along X axis.
$V_{Y\,max}$	Maximum linear velocity along Y axis.
$V_{Z\,max}$	Maximum linear velocity along Z axis.
a_y	Acceleration along Y axis.

a_z	Acceleration along Z axis.
d_0	Distance from the field-of-view to the lenses.
i_{bt}	Belt transmission ratio.
i_{gh}	Reduction ratio of the planetary gearhead.
i_{le}	Measuring resolution of the selected linear encoder.
m_{ML}	Mass of linearly displaced load.
m_{leads}	Mass of the Lead Screw.
m_{load}	Mass of the Load.
m_{mar}	Marginal mass.
m_z	Manipulated mass in case 1 (Section 3.6.1).
n_{GH}	Maximum recommended number of rotation per minute on the input shaft of the gearhead.
w_{max}	Maximum angular velocity along W axis.
w_{FOV}	Width of the field-of-view (FOV).
$x_{lh1} - x_{lh7}$	Distances in the lower H-like belt structure.
x_{m1}	Distance between the axis of the driving pulley to the axis of the driven pulley in the first middle belt structure.
x_{m2}	Distance between the axis of the driving pulley to the axis of the driven pulley in the second middle belt structure.
x_{mar}	Estimated distance (margin) for tightening middle belts.
$x_{uh1} - x_{uh6}$	Distances in the upper H-like belt structure.
x_{uh7}, x_{uh8}	Distances in the upper belt tensioner.
η_{bss}	Estimated transmission coefficient of a Ball Screw.
η_{bt}	Transmission coefficient of a belt driven mechanism.
$\dot{\theta}$	Angular acceleration of driving pulleys.
$\Delta q_1, \dots, \Delta q_4$	Angular change of driving pulley from 1 to 4 respectively.
$\Delta\theta_1$	Angular change along the big pulley around Z axis in lower H'-gantry mechanism.

$\Delta\theta_2$	Angular change along the big pulley around Z axis in upper H'-gantry mechanism.
ΔW	Angular change along W axis.
ΔX	Linear change along X axis.
ΔY	Linear change along Y axis.
ΔZ	Linear change along Z axis.
$\Delta\theta$	Angular change along of the big pulley around Z axis in H'-gantry mechanism.
D	Effective diameter of the big pulley.
R	Effective radius of the big pulley.
d	Effective diameter of the small (idle and driving) pulleys.
f	Focal length.
g	Gravitational acceleration.
p	Lead Screw Pitch.
r	Effective radius of small (idle and driving) pulleys
α	Angle of inclination of the belt transmission system.
μ	Overall friction coefficient from sliding surfaces.

1. INTRODUCTION

Miniaturized devices and systems have become essential fragments of the commercial market place segments such as consumer electronics, biotechnology, medical engineering, communication infrastructure, avionics and etc. This more than half century lasting tendency in miniaturization relies on the reduction of the quantity of raw material and waste, decreasing of the manufacturing costs and cheaper transportation to name a few. However, while the miniaturizing trend was and still is present in consumer products, the production equipment had maintained its size. Since about two decades ago, researchers across the world started to investigate possible ways how the production facilities can have a commensurate (or at most one order of magnitude greater) size in comparison to the size of the manufactured parts.

1.1. Micro and desktop factories

Micro and desktop factories are general terms that are used to describe a miniaturized production system used for manufacturing and/or assembly of small products and parts at micro/meso scale (10 to 10^4 μm) [1]. According to [2], the desktop and the micro factory concepts refer to the same basic idea, i.e. minimized production equipment scaled down to desktop level so it can be manually moved without any need of lifting aids.

In fact, the downsizing of machine tools and other manufacturing systems emerged in Japan in the 1990's [3]. The initial primer was made by the development of a micro-lathe (Figure 1-1, left) with size smaller than a human palm. Furthermore, manufacturing units such as milling machine, press, transfer arm and manipulator have been miniaturized and integrated into a single portable box (625 x 490 x 380 mm^3) named as portable microfactory (Figure 1-1, right) [3] [4].
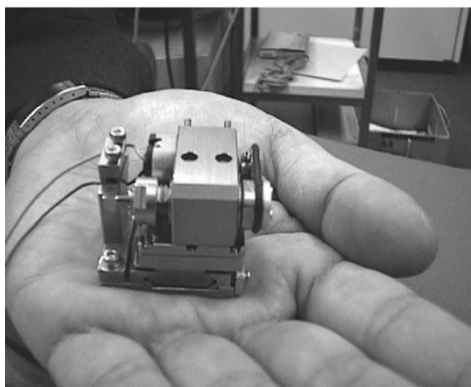

Figure 1-1 Micro-lathe (left) [3]; Portable microfactory (right) [3] [4]

Since the beginning of the 2000's, the micro and desktop factory related research has spread across the world and detailed information about some developed concepts can be found from [5] to [11].

Impacts from the micro and desktop factories

Okazaki et al [3] suggest that micro and desktop factories have significant improvements categorized in several domains.

In the *environmental domain* these technologies enable savings of energy and material resources, then reducing noise and vibration of machines as well as easier waste handling.

The *economic domain* embraces lower capital investment and running costs for the production equipment and facilities such as space, power infrastructure and environmental conditioning. Additionally, the micro and desktop factories increase the portability and re-configurability, thus allowing the shop floor firmly to respond to the fast changing market trends and variable batches.

The *technical domain* involves higher speed and accelerations of moving parts due to reduced masses i.e. inertias; more precise and accurate machines can be made due to increase of structural loop stiffness and resonant frequency so the machines will became more resistant of external vibration and thermal deformation. Another fact that supports the technical improvements is the productivity because of the shorter transfer distances as well as easier material handling.

Last but not least is the *human related* domain. This means that the job of machine operators is expected to be less mentally and physically stressful as well as less harmful potential damages. Another important fact is that the micro and desktop factories can be used for educational and hobby purposes, for example for building do-it-yourself machines and/or 3D printers.

Application fields of the micro and desktop factories

The commercial application of this kind of factories can be found in *micro-machining* of micro/meso scale mechanical components such as small gears, mirrors and other small optical devices, hearing aids, dental components and biodegradable implants. [3][12][13][14]. Further on, these micro-factories can be found in *micro-assembly* operations in high-precision mechanics in watch-making and consumer electronics industry (assembling watches, gearheads, micro-motors, mobile phones and other hand-held devices) [15][16]. Some publications, for example [10], suggest that these factories can be used in production of small batches of micro electro-mechanical systems (MEMS) as well. Additional usage is found in *finishing and quality control* related tasks such as laser marking and carving [17] [18], UV-printing [19], ultrasonic washing [12], dimensional inspection [20] and so on. Beside all this, microfactories can be used in *micro-dosing applications* in industrial and/or laboratory equipment. A few examples of such desktop factories can be found in [21] and [22]. Above all, the most publicly recognized applications of the desktop factory concept are the extrusion type and stereo lithography based additive manufacturing machines or commonly known as 3D-printers [23],[24],[25] and [26] to reference a few.

State of the art

The trend in miniaturization of production equipment is also acknowledged in the future trends in development of nanomanipulation devices as stated in the new book of Dr Xie et al, entitled "Atomic Force Microscopy Based Nanorobotics" [27]. In addition to this, the research group of Professor Dan O Popa from the University of Texas at Arlington, has being investigating the miniaturization of such nano-based manipulators by innovating new mechanical structures for AFM probe manipulation as depicted in [28].

The Laboratory of Robotic Systems LSRO, École Polytechnique Fédérale de Lausanne EPFL has been investigating new sensor technology for pollution monitoring in the microfactories [29] and also suggested new microfactory concepts with circularly arranged production modules around a rotary table with central air inlet [11] [30]. In a similar fashion, a concept improvement of the previous work in Karlsruhe Institute of Technology (KIT) is performed by Hoffman [31]. An extension of this later concept along with the TUT microfactory concept (examined in Section 2.1) into Evolvable Micro Production Systems (EMPS) is reported in [32]. A few groups from Italian technical universities have joined the forces to make performance improvements of some already seen microfactory concepts [33] [34].

1.2. Desktop-size manipulators

Although there is a lot of research work done in micro/meso robotics, the focus of this section goes into description of a few manipulators that are used in micro/meso scale manipulation tasks. Table 1-1 introduces three manipulators out of which two are commercially available and one is developed in the academia for research purposes only.

Table 1-1 Micro/meso scale applicable robot manipulators

Model/Name	Robot Image	Institution	Country
Parvus		Institute of Machine Tools and Production Technology (IWF), Technical University of Braunschweig	Germany
Mitsubishi Robot RP Series		Mitsubishi Automation	Japan
Delta Robot		CSEM/Asyril	Switzerland

Parvus [35][36] is a manipulator with parallel kinematics with maximum cubical workspace of 60 x 45 x 20 mm^3, and it is being developed in Institute of Machine Tools

and Production Technology (IWF) at the Technical University of Braunschweig in Germany. In fact, this manipulator is able to carry a payload of 50 *grams*, and features four DOF with repeatability from 5.9 to 14.1 *µm* (based on different location across its workspace). The displacement along *X* and *Y* directions of the end-effector on Figure 1-2 is realized by interpolation of the two active joints A_1 and A_2 together with the three passive joints denoted as B_1, B_2 and C. The vertical movement along *Z* axis is realized by lifting the whole light-weight structure with conventional ball screw. In addition, the rotation ψ is realized by direct attachment of motor with gearhead in the passive joint C which acts as tool centre point (TCP).
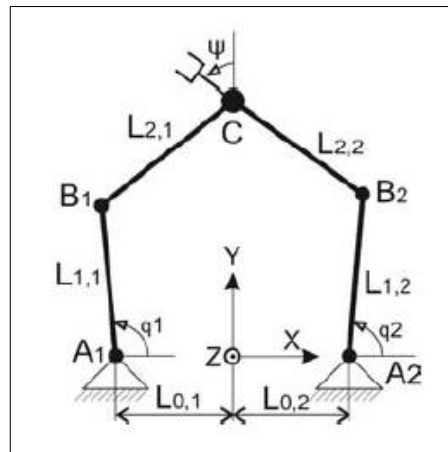
Figure 1-2 Parallel Structure of Parvus [35]

The smallest size of Mitsubishi RP Series [37] has a payload of 1 kg and cubical workspace of 150 x 105 x 25 mm^3. The repeatability of this manipulator is 5 *µm* in *X* and *Y* direction, and 10 *µm* in *Z* direction. The *XY* displacement principle is the same as the one in Parvus, the *Z* and ψ movements are achieved by use of Ball Screw Nut with Spline Nut [38]. This later device is also called Ball Screw-Spline (BSS) mechanism and it enables one rotational and one translational movement along the same axis. The BSS is a key component in all SCARA manipulators as well as in DOHMAN's structure. Detailed examination of the BSS can be found in Chapter 2.4.

The Pocket Delta Robot [39] was developed by Swiss Centre for Electronics and Micro-technology (CSEM) and commercialized by a company called Asyril [40]. Pocket Delta is the smallest robot from the delta family and it features 2,5 *µm* repeatability and 20 *grams* nominal payload. The parallel kinematics enables the manipulator to have workspace of 100 *mm* in diameter in *XY* and 30 *mm* in height (Z direction). The compactness of this manipulator is evident by the fact that the control unit together with the amplifiers is enclosed above the robot.

Common fact for all of the three presented manipulators is the usage of parallel kinematic structure. The advantage of this kinematic arrangement is the possibility to place the motors out of the moving mechanisms, thus to reduce the mass of the dynamic parts. For more desktop-size manipulators, please refer to references from [41] to [44].

1.3. AC-DESK project

Adaptive and Collaborative Desktop Factory AC-DESK is TEKES funded parallel project among five Finnish industrial partners and the Department of Mechanical Engineering and Industrial Systems (MEIS) at Tampere University of Technology (TUT) [45]. The project aims to develop desktop size manufacturing and assembly systems, i.e. desktop factories, used in production and quality control of telecommunication devices and biomedical products. The objective of AC-DESK project is to prepare the participating companies, production system suppliers and device producers, for the global breakthrough of the desktop production systems.

According to the research plan [45] AC-DESK is expected to impact the participating technology provider companies with strong base for design and development of new and competitive products for desktop manufacturing systems. In addition, the end users of desktop manufacturing systems, i.e. the device producers, are expected to implement these desktop systems developed within the project and obtain cost efficient production. The AC-DESK project consists of four work packages. Each work package (WP) contains specific tasks that are expected to be completed during the project. The project layout looks as follows:

1. WP Desktop Production Devices and Systems
    1.1. High performance and cost efficient desktop robots
    1.2. Desktop manufacturing system for medical industry
    1.3. Technologies for desktop manufacturing systems
    1.4. Advanced measurement technologies
2. Desktop Processes
    2.1. Manufacturing processes for desktop platforms
    2.2. Special issues of miniaturisation
3. Modular Reconfigurable Production Systems
    3.1. Modular plug and play type production line
    3.2. Reactive and reconfigurable production system
4. Ecological and Economical Opportunities

DOHMAN's realization belongs to task 1.1. This task encompasses developing new microfactory size prototype robot for the study of the performance and the robot optimization. Typical challenges in development of desktop sized robots are mass optimization, achieving optimal trade-off between accuracy and speed, issues in cable management, spatial enclosing of control system, calibration methods and so on.

1.4. Motivation

Taking into consideration that Microfactory RG had positive experience with the *H*-gantry positioning tables implemented in some of the previously developed robots (Section 2.2), a manipulator design with double *H*-gantry mechanical structure became desirable and challenging step towards making new and innovative desktop size manipula-

tion system. Moreover, one of the main motivations for developing this robot is the aspiration to obtain dexterous desktop robot design without having motors in the moving structure. This distributed actuation was expected to isolate the motor from the mechanical system and thus reduce the cabling issues that were limiting factor in the previous works.

1.5. Thesis objectives and scope

The objective of this Master of Science thesis is to design and implement a double *H'*-gantry four DOF (*X*, *Y*, *Z*, and *W*) manipulator (called DOHMAN) as a constituting process module within TUT-µF cell. This includes making conceptualization and design of the manipulator (robot) and whole µF cell around it, kinematic modeling of the robot, dynamic dimensioning, motion control, setup for visual feedback-ing, and overall physical implementation. Similar implementation of such robot is reported in [46]. The performance parameters such as velocities, resolution and workspace are theoretically estimated as well.

In a nutshell, this thesis is examining the design decisions, meaning what kind of parts are selected, how they are spatially arranged, mutual dependencies and what justifies a specific component selection. The thesis depicts mechanical analysis including the kinematical modeling (required for the motion control of the robot) and drive dimensioning (required for torque calculations for the mechanical drives selection - motors and gearheads). The thesis, in addition, is examining the control and vision related concerns such as control architecture, motion control design, SW and HW implementation, communication protocols and interfaces, and machine vision setup dimensioning and design. Implementation concerns such as manufacturing and/or assembly of the mechanical parts, encountered problems and solutions as well as experimental validation are also being elaborated.

1.6. Robot development methodology and research materials

Robot development methodology in Microfactory RG at TUT is mostly focused in developing and implementing new kinematic concepts for micro/meso scale manipulators. The design procedure of the DOHMAN robot started with defining the desired kinematic structure. Then the initial CAD drawings with possible kinematic realization were made and iteratively redesigned in order to create a concept that becomes easily implementable. The level of the implementation was judged by the maximization of the workspace, number of components and the complexity of the assembly. Once the final CAD design was obtained, the work continued with ordering of the off-the-shelf parts and manufacturing the custom developed ones. During the physical integration many assembly issues appeared due to some missed details form product datasheets and lack of experience of the designer. In addition to this, a huge delay in building the prototype

was caused by long delivery times of the components that were mainly ordered from companies out of Europe.

The development of DOHMAN represents an incremental contribution in the field of miniaturized manipulation systems used in the micro/desktop factories. The reference literature is mainly based on conference proceedings and journals enlisted bellow:

Conferences:

- International Workshop on Microfactories IWMF
- International Workshop on Microfactory Technology IWMT
- International Forum on Desktop Factory in SUWA
- International Precision Assembly Seminar IPAS
- International Symposium on Assembly and Manufacturing ISAM
- International Symposium on Robotics ISR
- JSME/ASME International Conference on Materials and Processing ICMP
- Transactions of North American Manufacturing Research Institution of the Society of Manufacturing Engineers (NAMRI/SME)
- SPIE Proceedings (volume 4568) on Microrobotics and Microassembly III

Journals:

- International Journal on Assembly Automation
- International Journal on Automation Technology
- IEEE Transaction on Mechatronics
- Journal of Manufacturing Science and Engineering

Beside the literature above, several reviews and roadmaps independently published from few research centers and universities were consulted as well. In addition to this, the robot development was affected by following the best practices that came from the robot development work done in the Microfactory RG. Decisions about certain off-the-shelf components were made based on the positive experience from particular manufacturers and distributors familiar to the supervising team.

1.6.1. Software

This section introduces the software platforms used during the design and modeling of DOHMAN.

CATIA

CATIA (Computer Aided Three-dimensional Interactive Application) is a commercial SW suite that supports computer-aided-design (CAD), computer-aided manufacturing (CAM) and computer aided engineering (CAE) [47]. This multi-platform software was used in the mechanical design of DOHMAN, as well as in designing the other modules of the developed TUT µF cell.

MATLAB

MATLAB (**Mat**rix **Lab**oratory) is a SW environment that enables high-level program-ming, visualization and complex numerical computations. This SW platform is well suited for data analysis, developing algorithms and modeling [48]. As such MATLAB was used in the kinematic and dynamic modeling and verification of DOHMAN.

TwinCAT

TwinCAT (**T**he **Win**dows **C**ontrol and **A**utomation **T**echnology) is software suite for PC-based control used in automation systems. This SW environment is produced by Beckhoff Automation GmbH and it enables PC-based systems to perform real-time PLC, NC, CNC and robotics control [49]. TwinCAT was used for programming the motion control of DOHMAN along with the overall control of the developed TUT μF cell.

LabVIEW

LabVIEW (**Lab**oratory **V**irtual **I**nstrument **E**ngineering **W**orkbench) is a graphical pro-graming SW platform that enables system design, development and fast integration [50].This SW platform was used for machine vision applications in Microfactory RG, thus it will be used for machine vision purposes also in DOHMAN.

1.6.2. Hardware

The bill of materials used for development of the DOHMAN as process module in the TUT μF cell and the control and vision module can be found in Appendix 1 and 2 re-spectively. When each component is introduced, its datasheet can be found accordingly in the reference chapter, i.e. Chapter 7. For certain custom-design parts some 3D illus-trations and/or technical drawings are provided as specified in the text, i.e. in the text itself or in the appendices.

1.7. Thesis structure

Chapter 2 depicts the theoretical background of microfactories and miniaturized robot manipulators developed in Department of Mechanical Engineering and Industrial Sys-tems. In addition this chapter explains the mechanical structure of the *H*-gantry and BSS mechanisms. Chapter 3 in the beginning briefly introduces the layout of the developed μF cell and later elaborates the complete design, kinematical modeling and drive dimen-sioning of the mechanical system. Further on, Chapter 4 depicts control and vision re-lated concerns as well as their mutual integration into one unit, i.e. control and vision module. Chapter 5 presents all the challenges that were encountered during the imple-mentation phase, whereas Chapter 6 shows the results and discussion upon them along with a summary of the presented work. Chapters 7 and 8 provide the reference literature and the appendices, respectively.

2. THEORETICAL BACKGROUND

This chapter presents the research in micro-production systems and desktop size robotics done in TUT Microfactory RG. Additionally, this chapter depicts the structure and the working principle of the *H*-gantry and BSS mechanisms.

2.1. TUT microfactory (TUT µF) concept

Microfactory RG from the Department of Mechanical Engineering and Industrial Systems at TUT is an active player within the research of miniaturized production systems. The group developed many concepts and prototypes among which the TUT microfactory[©] concept (shortly: TUT-µF) depicted in detail in [51]. In principle, this microfactory concept represents a modular integration of different kind of modules (base module, process module, control module and etc.) into a *microfactory cell*. The core of the designed concept leans on the idea that the base module provides workspace (cleanroom possibility included) and is able to interface with all the necessary auxiliary modules in order to compose a production or manufacturing unit.

On the figure below, a standardized *base module* (left) and example layout of the TUT-µF cell (right) are illustrated. The standard outer dimensions of the base module are 300 x 200 x 220 mm^3 split into two rooms: the inner workspace with dimensions of 180 x 180 x 180 mm^3, and control unit compartment with dimensions of 190 x 80 x 180 mm^3. A *process module* is a module that performs a particular process, for instance assembly operation, welding, laser marking, and so on. The process module in right figure below consists of the Pocket Delta Robot and the interface frame, and its role is to perform assembly of small components.
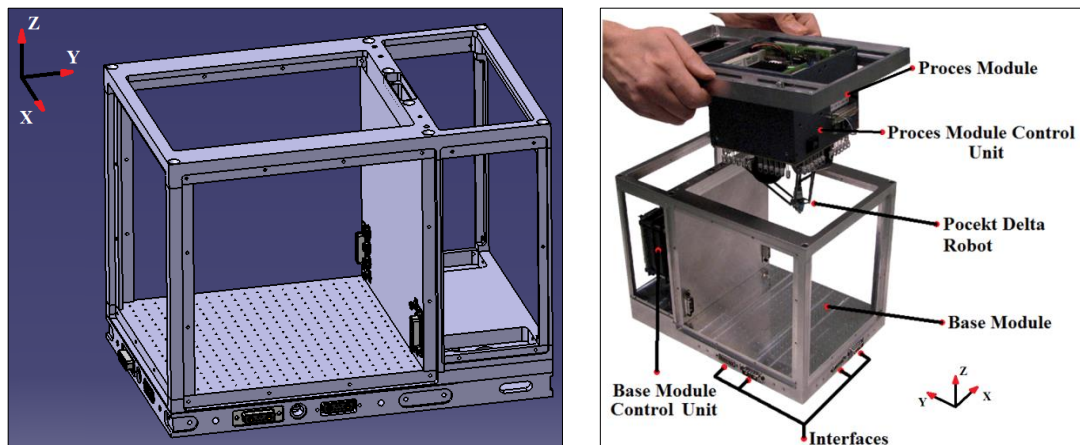
Figure 2-1 TUT µF cell: Base module (left) and sample implementation (right [51]).

Each module has its own control unit. The control unit of the base module is located in the control cabinet in the back side of the base module. For the process module on Figure 2-1, the control unit is located above the robot itself. However, for more advanced implementations with more complex control, an additional module i.e. *control module* is dedicated for that, and thus the control decision making operations are distributed to that module.

The TUT µF cells can be utilized for manufacturing and/or assembly operations. More cells can be connected to each other and thus form a small sized manufacturing and/or assembly line. Such organization enables nearly unlimited ways of factory layout creations [51]. One example of a possible microfactory layout is illustrated on the Figure 2-2. The base modules of each µF cell can be connected one next to each other in side by side order, and/or side by front order, and/or front by front order.
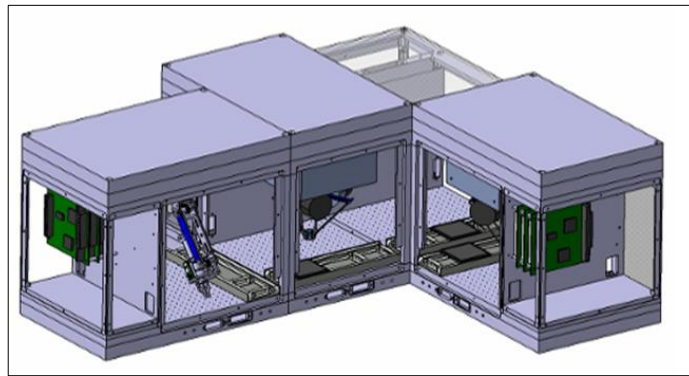
Figure 2-2 Modular integration of TUT µF [51]

These modular miniaturized production systems can be utilized in manufacturing of medical implants, laser marking and cell phone loudspeaker assembly, see Figure 2-3. The microfactories with such small geometries feature easy and rapid re-configurability and mobility. The re-configurability refers to the possibility for performing fast changes into an existing assembly line thus adopting it for production of entirely new types of products. The mobility refers to the possibility of these microfactory cells to be displaced across different places within the production facilities.
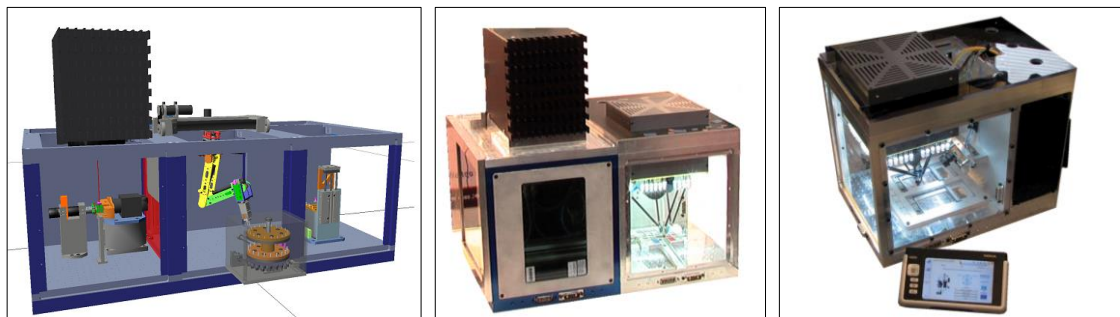
Figure 2-3 TUT µF for: medical implant manufacturing (left); laser marking (center); loudspeaker assembly (right). [51]

More demo applications of TUT-µFs are flexible screwing cell [52] (see Figure 2-4 right), gas sensor assembly [53] (see Figure 2-6), and etc.

2.2. Desktop size robotic manipulators developed by Microfactory RG

This section depicts three manipulators that were successfully designed and implemented in the TUT microfactory concept.

Figure 2-4 (left) shows *H-gantry Cartesian manipulator* used in miniaturized flexible screwing cell [52]. The manipulator is able to realize *X* and *Y* movements because of the *H*-gantry mechanism (explained in detail in the next section). The displacement along the *Z* direction is achieved by small ball screw, and additional extra stroke in the same direction is realized by small pneumatic cylinder. The pressure that comes from the pneumatic cylinder is used for provision of constant pressing force for performing the screwing operation.
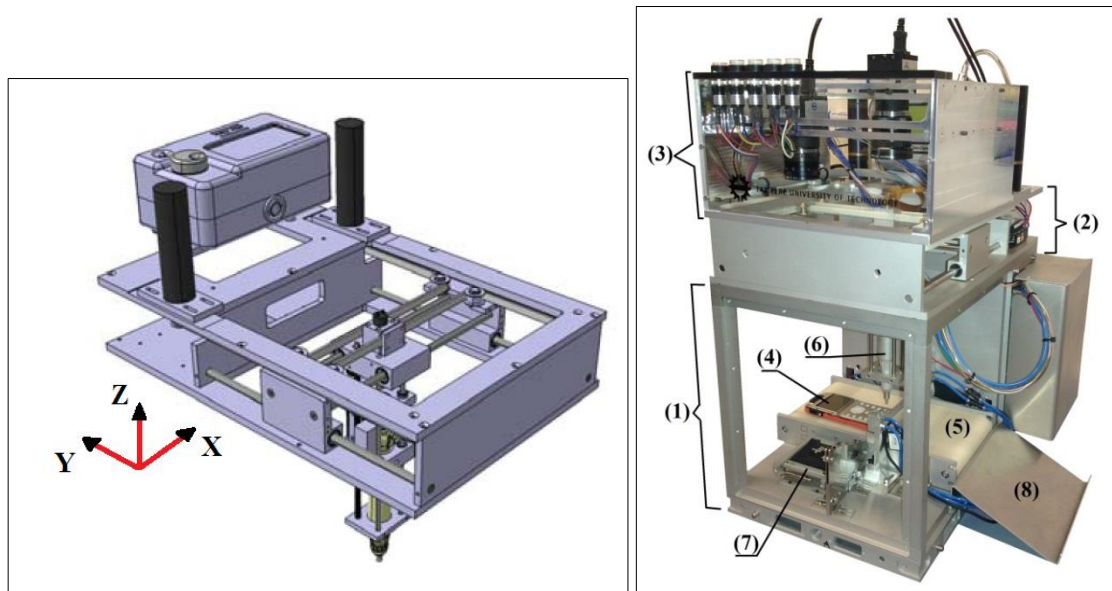
Figure 2-4 CAD-model of the *H*-gantry Cartesian manipulator (left); Manipulator's implementation within the TUT-µF cell (right). Images remodeled from [52].

The implementation of this *H*-gantry manipulator in the miniaturized flexible screwing microfactory cell is shown on Figure 2-4 (right). This µF cell layout consists of base module (1), robot module (2), and control and vision module (3). The working principle is as follows: A mobile phone (4) is brought by a conveyor (5) under the working envelop of the manipulator (6). The manipulator is using an automatic screw driver for screw insertion and it feeds with screws from the screw feeding container (7). Once all the screws are being fitted into the mobile phone, the mobile phone is moved out of the cell (8) and the cell is ready to receive a new mobile phone.

The *H-gantry Cartesian* robot operates in 101 x 123 x 46 mm^3 cube-like workspace and its payload capabilities are up to 100 *grams*. The maximum velocity along *X* and *Y* axes is 700 *mm/s*, and 13 *mm/s* along *Z* axis. The maximum acceleration along *X* and *Y* axes is ~3g, and along *Z* is ~0.03 m/s^2. The robot features resolution of 0.9 *µm* and 0.03 *µm* along the first two axes and the remaining one, respectively. [55]

The second example of successful manipulator development is shown on Figure 2-5. The so called *H-SCARA robot* is a four DOF manipulator with parallel kinematics that consist of two parallel structures: The first one is the *H*-gantry planar mechanism that enables displacement along the *X* and *Z* axis; and the second one is the parallel two-arm SCARA-type mechanism (similar as in Parvus manipulator, Chapter 1.2) that enables XY displacement. In addition to the obtained *XYZ* movement from the combined parallel structures, the *H*-SCARA manipulator is able to perform rotation around the *Z* axis (torque transmitted through belt drive). The workspace of this robot is ~300 x 250 x 100 mm^3, however the recommended workspace is not exactly stated.[53]
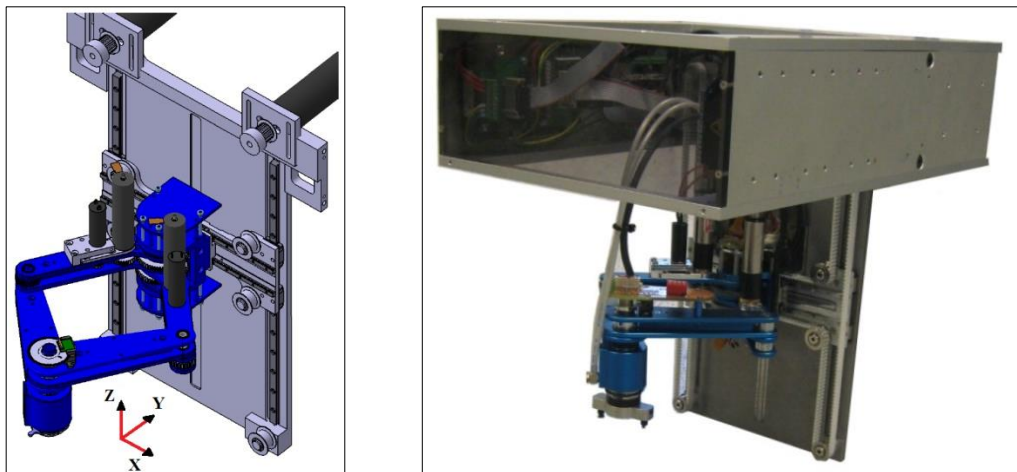
Figure 2-5 CAD-model without the belt (left) [53] and modular physical implementation (right) [54] of the *H*-SCARA manipulator

The implementation of the *H*-SCARA manipulator within the TUT µF is illustrated on Figure 2-6. The manipulator together with the motors, amplifiers and the I/O interfaces comprises the robot (process) module in this µF cell layout. The robot module interfaces below with the base module and above with the control/vision module.
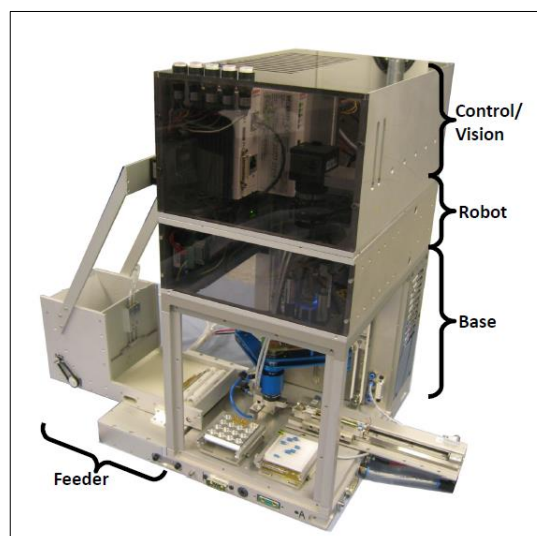
Figure 2-6 *H*-SCARA in TUT µF [53]

The control/vision module contains cameras for visual feedback, main level controls and buttons for human-machine-interface (HMI). The feeder is interfacing with the base

module from the left side. The application case of this microfactory is for automated assembly operation of gas detection sensors. [53]

The *H*-SCARA manipulator is capable to carry load up to 50 *grams*. The maximum velocity in *XZ* and *XY* planes are 630 *mm/s* and 200 *m/s* depending of which mechanism, either the *H*-gantry or either the two-armed SCARA structure, provides the drive. In addition, the maximum angular velocity is 3.1 rev/s around the *Z* axis of the robot. In similar fashion, the robot features maximum accelerations of 3.1 m/s^2 and 1 m/s^2 in *XZ* and *XY* planes, and angular acceleration of 9.4 $rev/^2$. The smallest incremental steps are 1 and 14.1 *μm* in *XZ* and *XY* planes and 0.18 *degrees* around *Z* axis. [55]

Last but not least is the next generation robot with SCARA parallel kinematic structure, i.e. the *Parallel SCARA robot.* This robot illustrated on Figure 2-7 features direct drive technology, stiffer arm construction, and simpler parallel SCARA structure. The displacement within the *XY* plane is realized by the two arm SCARA structure, and the displacement along *Z* axis by a ball screw. The show case of this robot is expressed through pick and place operation of spherical balls onto the blue matrix on the image below.
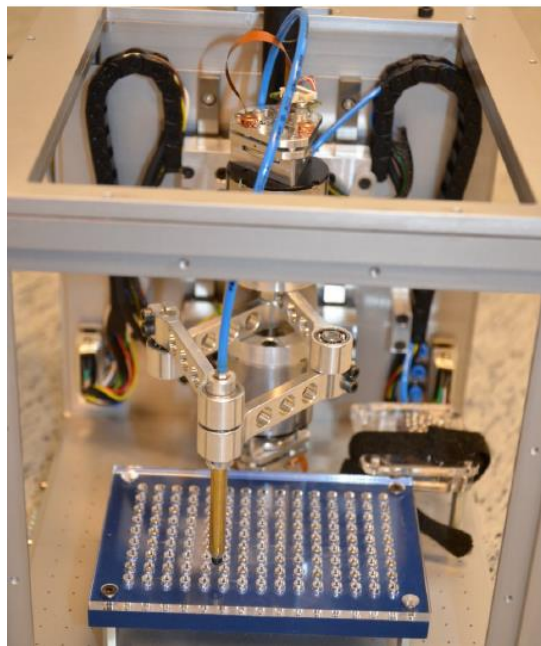
Figure 2-7 Parallel SCARA in TUT μF

The Parallel SCARA robot operates in 224 x 112 x 72 mm^3 workspace and it is capable to carry load up to 200 *grams*. However, the recommended workspace is ~220 x 100 x 50 mm^3 because of the difference in the rigidity and stiffness across the workspace. The maximum velocity and maximum acceleration are 100 mm/s^2 and 0.03 m/s^2. The robot features resolution of 9.9 *μm* along the first two axes. [55]

2.3. *H*-gantry mechanism

H-gantry is a common mechanism in manipulators developed in TUT and reported in [52], [53]. This mechanism is also known as *H*-bot and such notation can be found across several articles, e.g., [56] and [57]. This mechanism is shown on Figure 2-8, it consists of several components such as: driving gears (motor-gearhead-pulley assembly) (1), open loop belt (2), idle pulleys (3), lateral linear guideways (4), lateral linear slides (5), linking gantry i.e. *bridge*, and a *cart*. The *lateral slides* (5) are able to move linearly along the lateral *linear guideways* (4). The *bridge* is a gantry attached between the lateral slides and it contains a *central slide* along which the carrying mass (*cart*) is moving.
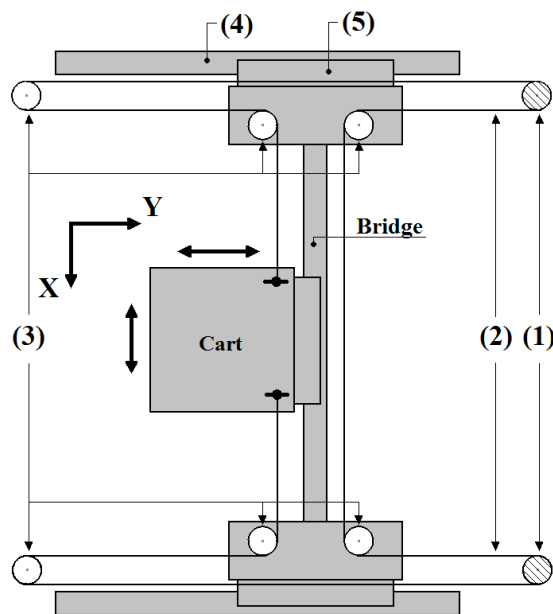
Figure 2-8 Concept of *H*-gantry mechanism with two DOF (XY)

The displacement of the cart is realized through one *open loop belt* (2) (loop starts and ends at the cart). The belt moves through eight pulleys where six are idle (3) and two are driving (1). Each of the latter two is attached to a motor through a gearhead. The gearhead is used as a redactor. The displacement of the cart along *X* axis is realized by moving both driving gears in the same direction. Analogue to that, the displacement along the *Y* axis is realized when both driving gears rotate against each other. A complete *XY* planar *H*-bot design, mathematical model and implementation are described in detail in [58].

2.4. Ball Screw-Spline mechanism

Figure 2-9 illustrates the *Ball Screw-Spline* (BSS) mechanism which comprises of *Ball Screw Nut*; *Ball Spline Nut*; and *Lead Screw* with screw and spline grooves that fit both nuts. This mechanism is able to perform two dimensional (linear and rotary) displacements, hence three types of motion modes (rotary, linear and spiral) are able to be realized.
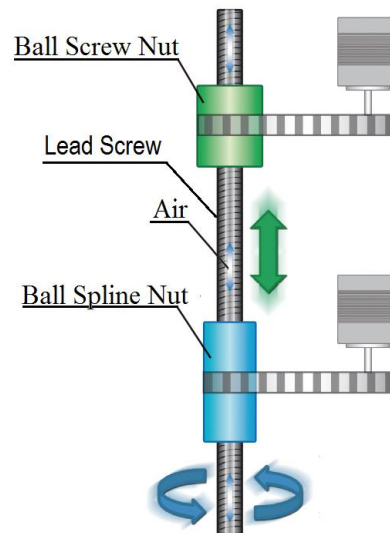
Figure 2-9 Ball Screw-Spline (BSS) component (Remodeled from [38])

The linear mode (green vertical arrow on the Figure 2-9) is accomplished by rotating the ball screw nut, i.e. linear motion of the lead screw is obtained as a result of the angular displacement of the screw nut. By rotation of both nuts in same direction, the rotary mode (blue curved arrows on the Figure 2-9) is achieved. Rotation of the spline nut results in torque in the lead screw and the ball screw nut should rotate in the same direction in order to keep the lead's vertical position unchanged. By rotation of the spline nut alone, the spiral mode is performed.

3. DESIGN OF DOHMAN

The first section of this chapter reveals the great picture of DOHMAN's integration into the TUT-µF cell, and then the later sections describe the mechanical design and component selection of the parts in DOHMAN manipulator. This procedure is known as top down approach. Sections 3.2 and 3.3 examine the kinematics of the two key mechanisms, i.e. *H'*-gantry mechanism and Ball Screw-Spline (BSS) mechanism. By spatial arrangement of two *H'*-gantries and one BSS mechanism, the core mechanical structure of DOHMAN is obtained and examined in detail in Section 3.4. The elaboration of the design continues with derivation of kinematic equations in Section 3.5 and dimensioning of driving gears in Section 3.6. Sections 0, 3.8, and 3.9 depict theoretical performance of the robot, selection of belts and pulleys, and homing procedure, respectively. Last but not least, the chapter ends the design explanation with a brief view towards the overall CAD illustration of DOHMAN, Section 3.10.

3.1. DOHMAN in TUT Microfactory cell

The aim of the section is to familiarize the reader with the idea of how DOHMAN is fitted within the modular structure. Figure 3-1 illustrates the DOHMAN's integration as a process module into the µF cell. The cell consists of the standardized base module, the DOHMAN robot (process module), and the control and vision module.
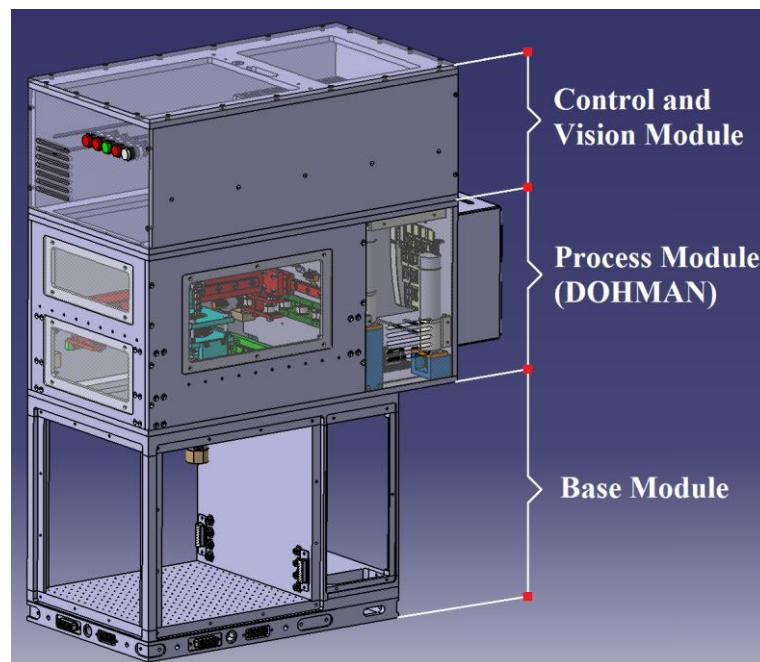
Figure 3-1 DOHMAN within the structure of the TUT uF

The space into the process module (DOHMAN) is divided in three fragments. The first fragment (mechanical part) is above the workspace of the base module and contains the mechanical system of the robot; the second fragment (actuation part) is located on the back side and it contains the motors and drivers or the hardware that enables the robot actuation; the third fragment (control part) is hollow sheet metal cube that is attached in a parasitic way to the actuation part and it contains the IO modules.

    The control and vision module is placed on the top of the cell. This module contains the controller with its unit modules, camera with optics and buttons for human interaction. More detailed explanation of the DOHMAN and the control and vision module are provided in this and the following chapter.

3.2. *H'*-gantry mechanism

    The *H*-bot mechanism used in DOHMAN is NOT with the same structure as the one on Figure 2-8. A sketch of the *H*-bot mechanism that actually is part of DOHMAN is illustrated on Figure 3-2 and in order to be distinguishable from the one on Figure 2-8, it is decided to be called *H'*-gantry or *H'*-bot. Therefore, the *H'*-bot is two dimensional $Y\theta$ mechanism that consists of two lateral slides (5) attached to linear guideways (4). The bridge represents linking gantry between the lateral moving slides. The carrying mass (cart) resides on the bridge and it contains a big pulley (6) and two small idle pulleys (3). The actuation in the system is provided by the two driving pulleys (1) which are attached to two motors through two gearheads thus forming the driving gears. The torque is transmitted by the closed loop belt (2) and the idle pulleys (3).
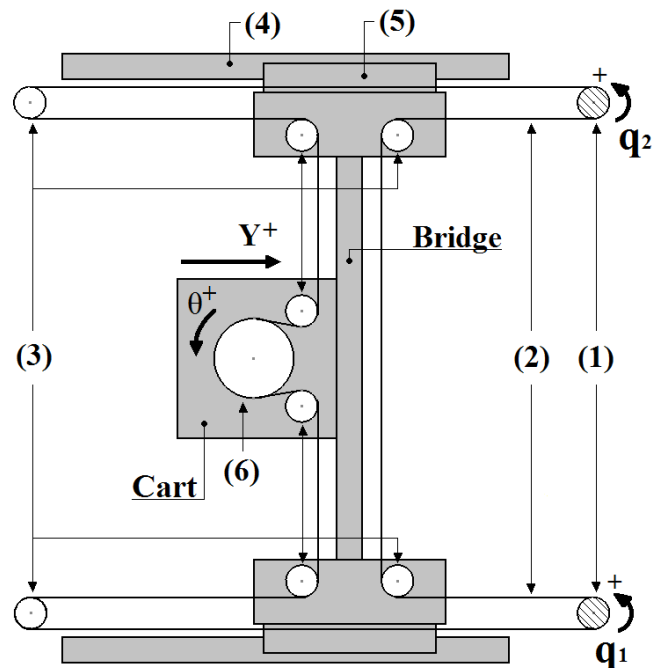
Figure 3-2 Concept of *H'*-gantry mechanism with two DOF (Yθ)

H'-bot kinematics

The displacement of the cart along the *Y* axis is realized by rotating the driving gears in opposite directions. When the rotations are realized in the same direction, the big pulley rotates around the *Z* axis (the axis pointing out of the paper). Table 3-1 provides a complete overview of all *Yθ* motion modes. Displacement along the *Z* axis can be achieved by plugging a lead screw or ball screw to the big pulley (6). In that case the *H'*-bot becomes able to perform two dimensional *YZ* displacements. However, *YZ* movement is not subject of interest now.

Table 3-1 *H'*-bot Motion Modes. Positive and negative rotations are denoted by positive and negative arrows respectively; and no movement of pulleys and cart is denoted by dot.

Motion Mode Number	Input: Pulley rotation		Output: Cart displacement and/or rotation of big pulley	
	Driving Pulley 1	Driving Pulley 2	Linear Displacement ΔY	Angular Displacement $\Delta \theta$
1.	+↻	●	← −	+↻
2.	●	+↻	→ +	+↻
3.	−↺	●	→ +	−↺
4.	●	−↺	← −	−↺
5.	+↻	+↻	●	+↻
6.	+↻	−↺	← −	●
7.	−↺	+↻	→ +	●
8.	−↺	−↺	●	−↺

The kinematic model of the *H'*-bot can be easily derived from the Figure 3-2 as well as from the motion modes illustrated in the table above. The first motion mode tells that turning driving pulley 1 while keeping the driving pulley 2 still results in linear movement along negative *Y* and positive rotation of the big pulley around *Z*-axis. Mathematically this can be expressed as

$$\Delta q_1 * r = -\Delta Y + R * \Delta \theta, \qquad (3.1)$$

where

- r is the effective radius of the small pulley,
- R is the effective radius of the big pulley,
- Δq_1 is angular change of the driving pulley 1,
- ΔY is linear change of the cart along *Y* axis, and
- $\Delta \theta$ is angular change of the big pulley around *Z* axis.

Thus

$$\Delta q_1 = -\frac{1}{r}\Delta Y + \frac{R}{r}\Delta\theta. \tag{3.2}$$

The same can be applied for the second motion mode, thus

$$\Delta q_2 = \frac{1}{r}\Delta Y + \frac{R}{r}\Delta\theta, \tag{3.3}$$

where

- Δq_2 is angular change of the driving pulley 2.

Equations (3.2) and (3.3) compose the **inverse kinematic model** and in more compact form it can be written as

$$\begin{bmatrix} \Delta q_1 \\ \Delta q_2 \end{bmatrix} = \begin{bmatrix} -1/r & R/r \\ 1/r & R/r \end{bmatrix} \begin{bmatrix} \Delta Y \\ \Delta\theta \end{bmatrix}. \tag{3.4}$$

The **direct kinematic model** can be solved by inverting the 2x2 matrix in (3.4), thus the following is obtained

$$\begin{bmatrix} \Delta Y \\ \Delta\theta \end{bmatrix} = \begin{bmatrix} -r/2 & r/2R \\ r/2R & r/2R \end{bmatrix} \begin{bmatrix} \Delta q_1 \\ \Delta q_2 \end{bmatrix}. \tag{3.5}$$

CAD of the lower H'-bot

Figure 3-3 provides CAD illustration in greater detail of one of the two *H'*-gantry mechanisms that are implemented in the design of DOHMAN.
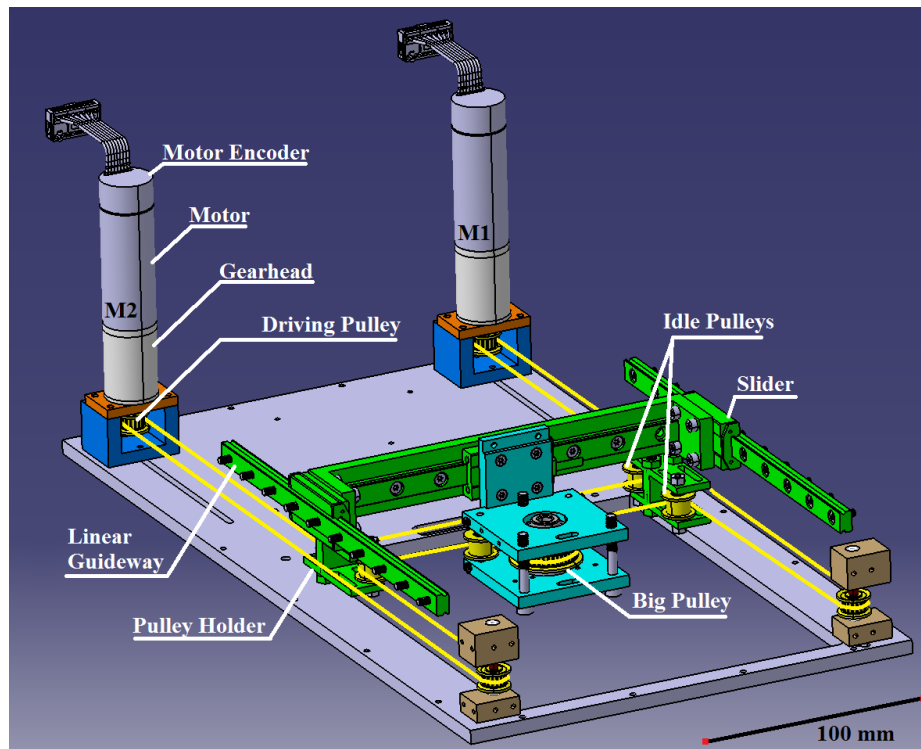
Figure 3-3 CAD illustration of lower *H'*-gantry mechanism (N.B. Guideways are attached to plates that are not shown in the figure because of visual purposes)

In fact, the Figure 3-3 illustrates the so called lower *H'*-gantry and it enables linear displacement along *Y* axis and/or rotation of the *big pulley*. The *π-like profile* acts as a bridge and connects the two *sliders* that are opposite to each other with same direction of displacement. On the bottom side of the π-like profile a *pulley holder* is attached and its role is to hold the central idle pulleys. The third slider with integrated *encoder* is mounted on the inner front side of the π profile. This slider interfaces with the cart colored in cyan that contains the big pulley.

The role of the integrated encoder is to measure the displacement of the cart caused from the other *H'*-gantry, i.e. the upper one. This might be vague at this point, but it is more carefully explained in Section 3.4.

The consisting parts of the *H'*-gantry mechanism are depicted in greater detail in Appendix 3.

3.3. Ball Screw-Spline selection and kinematics

There are two companies in the world, i.e. THK [59] and KSS [60] , both from Japan, which can manufacture the component in small dimensions as they could fit within the TUT microfactory concept. The second company was able to provide the BSS mechanism with smaller dimensions compared to the first one. On top of that, the KSS had offered about 30 % lower price and thus their product was selected as best offer.

Kinematics of the BSS mechanism

Table 3-2 depicts each motion mode in detail with its appropriate nut actuation(s).

Table 3-2 BSS Motion Modes

Motion Mode		Input: Nut rotation		Output: Shaft Motion	
		Ball Spline Nut	Ball Screw Nut	Vertical Displacement	Rotational Displacement
	1	●	−	+ ↑	●
	2	●	+	− ↓	●
	1	−	−	●	−
	2	+	+	●	+
	1	−	●	+ ↑	−
	2	+	●	− ↓	+
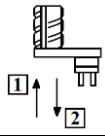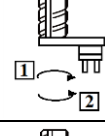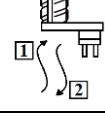
Let's assume that $\Delta\theta_1 [rad]$ is the *angular displacement (change) of ball spline nut* and $\Delta\theta_2 [rad]$ is the *angular displacement (change) of ball screw nut*. Let's also assume that $\Delta Z [mm]$ is the *shaft linear displacement* and $\Delta W [rad]$ is *shaft angular change*, thus the relation of $\Delta\theta_1$ and $\Delta\theta_2$ to ΔZ and ΔW can be mathematically expressed as

$$\Delta W = \Delta\theta_1,$$
$$\Delta Z = \frac{p}{2\pi}(\Delta\theta_1 - \Delta\theta_2),$$ (3.6)

where $p[mm]$ is the pitch of the lead screw.

A technical drawing of the implemented BSS component together with a CAD design of the overall BSS sub-assembly can be found in Appendix 4.

3.4. DOHMAN's mechanical structure

For obtaining four DOF kinematic structure, the H'-gantry mechanism (Figure 3-2) is doubled, shifted and rotated for 90 *degrees* in CW direction. In fact, Figure 3-4 illustrates the design of the core mechanical structure of the DOHMAN robot. The upper H'-gantry is colored in red and the lower in green. The BSS component is placed between the two big pulleys of the upper and lower H'-gantries. The BSS sub-assembly is colored in cyan. The upper H'-gantry mechanism reassembles the "H" letter in vertical orientation and its comprising belt is colored in white. The lower H'-gantry reassembles the "H" letter in the horizontal orientation and its belt is colored in yellow.
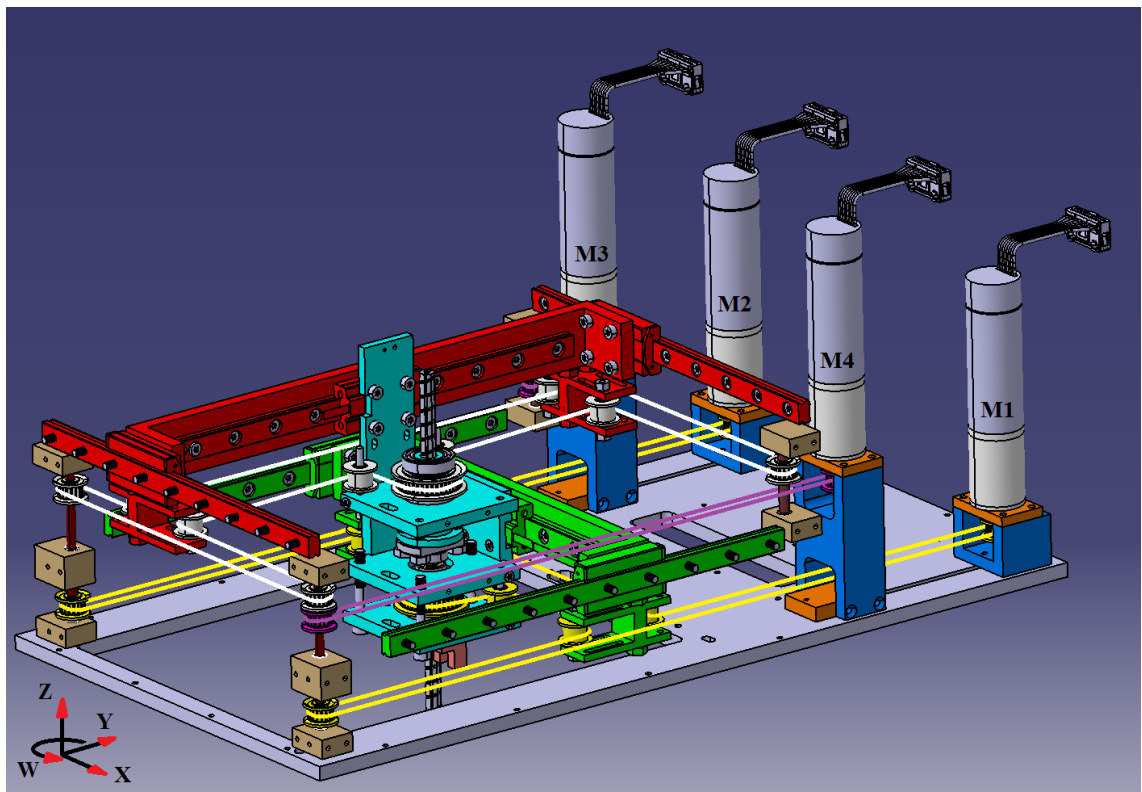
Figure 3-4 CAD of core mechanical structure of DOHMAN (many structural parts are hidden in order to illustrate the robot's working principle)

The lower H'-gantry is actuated by motors M1 and M2. The torque is transferred through the belt and pulleys colored in yellow. This H'-bot enables translation along Y axis and rotation of the spline nut. The power transmission in the upper H'-bot is arranged through the white colored pulleys and the white colored belt. This mechanism is

indirectly actuated by motors M3 and M4. The motors M3 and M4 drive the pink colored pulleys which are transferring the torque from the motors through the common axis shared with the white colored pulleys, see Figure 3-14 for more detailed illustration. This way, displacement along all three Cartesian axes X, Y and Z and one rotation around the Z axis, i.e. W is enabled.

One can infer that the spatial arrangement of the pulleys and belts is done in three levels. First level (closest to the bottom plate) is colored in yellow, second level is colored in pink, and third in white.

The linear sliders along the guideways of the bridges in both H'-bots contain integrated linear encoders. The role of the linear encoder in the upper H'-gantry structure is to precisely measure the linear displacement along the Y axis, or in other words the drive caused by the lower H'-gantry. Likewise, the linear encoder of the lower H'-gantry measures the displacement along X which is caused by the upper H'-gantry.

3.5. DOHMAN's kinematic modeling

This section depicts the kinematics of DOHMAN. It starts by obtaining the *initial forward kinematic model*, meaning that linear displacement ΔX and ΔY as well as angular changes $\Delta \theta_1$ and $\Delta \theta_2$ of the ball spline nut and ball screw nut respectively, are obtained as function from angular change of each driving gear $\Delta q_1 \ldots \Delta q_4$. By expressing ΔZ and ΔW as functions from $\Delta \theta_1$ and $\Delta \theta_2$ the *final forward kinematic model* is obtained. The inverse kinematic equation is then easily determined by simple inversion of the previously defined *final direct kinematic* model. At the end of this section, further derivation of the kinematic models yield the Jacobian matrices of the DOHMAN robot.

Initial forward kinematics

The initial forward or direct kinematic representation of DOHMAN has the following form

$$\begin{bmatrix} \Delta X \\ \Delta Y \\ \Delta \theta_1 \\ \Delta \theta_2 \end{bmatrix} = \begin{bmatrix} a_{d11} & a_{d12} & a_{d13} & a_{d14} \\ a_{d21} & a_{d22} & a_{d23} & a_{d24} \\ a_{d31} & a_{d32} & a_{d33} & a_{d34} \\ a_{d41} & a_{d42} & a_{d43} & a_{d44} \end{bmatrix} \begin{bmatrix} \Delta q_1 \\ \Delta q_2 \\ \Delta q_3 \\ \Delta q_4 \end{bmatrix} \tag{3.7}$$

where $[\Delta X \ \Delta Y \ \Delta \theta_1 \Delta \theta_2]^T$ is *initial position and orientation vector*, $[\Delta q_1 \ \Delta q_2 \ \Delta q_3 \ \Delta q_4]^T$ is *vector with angular displacements* of all driving pulleys, and A_d is *initial direct kinematic matrix* in which $a_{d11}, a_{d12}, \ldots, a_{d44}$ are members of the matrix.

The H'-bot kinematics part in the Section 3.2 showed that each rotation at the driving pulley Δq_1 results in linear displacement ΔY and angular displacement $\Delta \theta$ of the big pulley with appropriate magnitudes given in the equation (3.5).
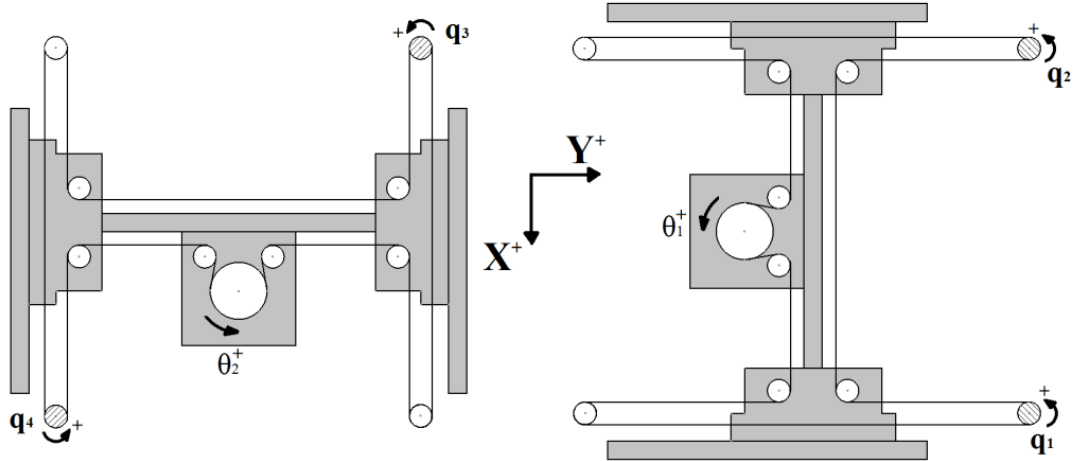
Figure 3-5 Unfolded view of the two *H'* bots

However, if the mechanical arrangement of DOHMAN is observed on Figures 3-4 and 3-5 and the same case is considered (rotating Motor 1), it can be inferred that the linear change ΔY will cause rotation at the other big pulley i.e. $\Delta \theta_2$ with the same magnitude as in $\Delta \theta_1$. Therefore the change Δq_1 will result with linear displacement $(^{-r}/_2)\Delta Y$, and rotation of both big pulleys $(^r/_{2R})\Delta \theta_1$ and $(^r/_{2R})\Delta \theta_2$. So the first column of the A_d matrix will be as follows:

$$a_{d11} = 0; \ a_{d21} = {}^{-r}/_2; \ a_{d31} = {}^r/_{2R}; \ a_{d41} = {}^r/_{2R}. \tag{3.8}$$

Same approach can be applied for each displacement change Δq_2, Δq_3 and Δq_4, and thus the following is obtained:

$$
\begin{aligned}
a_{d12} &= 0; \ a_{d22} = {}^r/_2; \ a_{d32} = {}^r/_{2R}; \ a_{d42} = {}^{-r}/_{2R}; \\
a_{d13} &= {}^r/_2; \ a_{d23} = 0; \ a_{d33} = {}^{-r}/_{2R}; \ a_{d43} = {}^r/_{2R}; \\
a_{d14} &= {}^{-r}/_2; \ a_{d24} = 0; \ a_{d34} = {}^r/_{2R}; \ a_{d44} = {}^r/_{2R}.
\end{aligned}
\tag{3.9}
$$

Substituting (3.8) and (3.9) into (3.7) the initial direct kinematic form will be:

$$
\begin{bmatrix} \Delta X \\ \Delta Y \\ \Delta \theta_1 \\ \Delta \theta_2 \end{bmatrix} =
\begin{bmatrix}
0 & 0 & {}^r/_2 & {}^{-r}/_2 \\
{}^{-r}/_2 & {}^r/_2 & 0 & 0 \\
{}^r/_{2R} & {}^r/_{2R} & {}^{-r}/_{2R} & {}^r/_{2R} \\
{}^r/_{2R} & {}^{-r}/_{2R} & {}^r/_{2R} & {}^r/_{2R}
\end{bmatrix}
\begin{bmatrix} \Delta q_1 \\ \Delta q_2 \\ \Delta q_3 \\ \Delta q_4 \end{bmatrix}
\tag{3.10}
$$

Equation (3.10) can be validated from Table 3-3.

Table 3-3 Initial kinematic motion modes of DOHMAN

Motion Mode Number	Input: Driving pulley rotation				Output: BSS displacement or rotation of big pulleys			
	Δq_1	Δq_2	Δq_3	Δq_4	ΔX	ΔY	$\Delta \theta_1$	$\Delta \theta_2$
1.	$+\circlearrowright$	•	•	•	•	← (−)	$+\circlearrowright$	$+\circlearrowright$
2.	•	$+\circlearrowright$	•	•	•	→ (+)	$+\circlearrowright$	$-\circlearrowleft$
3.	•	•	$+\circlearrowright$	•	↓ (+)	•	$-\circlearrowleft$	$+\circlearrowright$
4.	•	•	•	$+\circlearrowright$	↑ (−)	•	$+\circlearrowright$	$+\circlearrowright$

Final forward and inverse kinematics

As already shown in (3.6), ΔZ and ΔW can be expressed as functions from $\Delta\theta_1$ and $\Delta\theta_2$. Therefore substituting (3.6) into (3.10) yields the final forward kinematic model, i.e. for given angular change at each driving pulleys $\Delta q_1 \dots \Delta q_4$, the position $(\Delta X, \Delta Y, \Delta Z)$ and orientation (ΔW) of the tool center point (TCP) is obtained. Thus:

$$
\begin{bmatrix} \Delta X \\ \Delta Y \\ \Delta Z \\ \Delta W \end{bmatrix} =
\begin{bmatrix}
0 & 0 & r/2 & -r/2 \\
-r/2 & r/2 & 0 & 0 \\
0 & pr/2\pi R & -pr/2\pi R & 0 \\
r/2R & -r/2R & -r/2R & r/2R
\end{bmatrix}
\begin{bmatrix} \Delta q_1 \\ \Delta q_2 \\ \Delta q_3 \\ \Delta q_4 \end{bmatrix}
\tag{3.11}
$$

where $[\Delta X\ \Delta Y\ \Delta Z\ \Delta W]^T$ is called *final position and orientation vector* and the obtained matrix can be named as *final direct kinematic matrix M_d*.

$$
\begin{bmatrix} \Delta X \\ \Delta Y \\ \Delta Z \\ \Delta W \end{bmatrix} = M_d
\begin{bmatrix} \Delta q_1 \\ \Delta q_2 \\ \Delta q_3 \\ \Delta q_4 \end{bmatrix}
\tag{3.12}
$$

Tabular view of the final direct kinematics is provided in Table 3-4.

Table 3-4 Final direct kinematic motion modes of DOHMAN

Motion Mode Number	Input: Rotation of driving pulleys				Output: Axis position			
	Δq_1	Δq_2	Δq_3	Δq_4	ΔX	ΔY	ΔZ	ΔW
1.	$+\circlearrowright$	•	•	•	•	← (−)	•	$+\circlearrowright$
2.	•	$+\circlearrowright$	•	•	•	→ (+)	+	$-\circlearrowleft$
3.	•	•	$+\circlearrowright$	•	↓ (+)	•	−	$+\circlearrowright$
4.	•	•	•	$+\circlearrowright$	↑ (−)	•	•	$+\circlearrowright$

The final inverse kinematic geometry can be determined as:

$$
\begin{bmatrix} \Delta q_1 \\ \Delta q_2 \\ \Delta q_3 \\ \Delta q_4 \end{bmatrix} = M_d{}^{-1} \begin{bmatrix} \Delta X \\ \Delta Y \\ \Delta Z \\ \Delta W \end{bmatrix}
\tag{3.13}
$$

Hence:

$$
\begin{bmatrix} \Delta q_1 \\ \Delta q_2 \\ \Delta q_3 \\ \Delta q_4 \end{bmatrix} = \begin{bmatrix} 1/r & -1/r & 0 & R/r \\ 1/r & 1/r & 0 & R/r \\ 1/r & 1/r & -2\pi R/pr & R/r \\ -1/r & 1/r & -2\pi R/pr & R/r \end{bmatrix} \begin{bmatrix} \Delta X \\ \Delta Y \\ \Delta Z \\ \Delta W \end{bmatrix}
\tag{3.14}
$$

The matrix in (3.14) is named as *final inverse kinematic matrix* $M_i = M_d{}^{-1}$. Tabular representation of the inverse kinematics is given below.

Table 3-5 Final inverse kinematic motion modes of DOHMAN.

Motion Mode Number	Input: Axis position				Output: Rotation of driving pulleys			
	ΔX	ΔY	ΔZ	ΔW	Δq_1	Δq_2	Δq_3	Δq_4
1.	↓+	●	●	●	+↻	+↻	+↻	−↺
2.	●	→+	●	●	−↺	+↻	+↻	+↻
3.	●	●	+	●	●	●	−↺	−↺
4.	●	●	●	+↻	+↻	+↻	+↻	+↻

Jacobian matrices

The conversion of joint velocities into generalized end-effector velocities (linear and angular) is represented by the derivative of the kinematic mapping or forward kinematics. In the robotics literature, this linear transformation is generally denoted as Jacobian of a manipulator [61]. Therefore *Jacobian matrix* of the manipulator can be obtained by applying time derivative of the final forward kinematics equation, i.e. equation (5.11). Hence:

$$
\begin{bmatrix} \Delta \dot{X} \\ \Delta \dot{Y} \\ \Delta \dot{Z} \\ \Delta \dot{W} \end{bmatrix} = \begin{bmatrix} 0 & 0 & r/2 & -r/2 \\ -r/2 & r/2 & 0 & 0 \\ 0 & pr/2\pi R & -pr/2\pi R & 0 \\ r/2R & -r/2R & -r/2R & r/2R \end{bmatrix} \begin{bmatrix} \Delta \dot{q}_1 \\ \Delta \dot{q}_2 \\ \Delta \dot{q}_3 \\ \Delta \dot{q}_4 \end{bmatrix} = J \begin{bmatrix} \Delta \dot{q}_1 \\ \Delta \dot{q}_2 \\ \Delta \dot{q}_3 \\ \Delta \dot{q}_4 \end{bmatrix},
\tag{3.15}
$$

where $[\Delta \dot{X}\ \Delta \dot{Y}\ \Delta \dot{Z}\ \Delta \dot{W}]^T$ is the *velocity vector* and $[\Delta \dot{q}_1\ \Delta \dot{q}_2\ \Delta \dot{q}_3\ \Delta \dot{q}_4]^T$ is the *vector with angular velocities of the driving gears*, and J is the Jacobian matrix. In a similar

fashion the *inverse Jacobian matrix* can be obtained by time derivative of the inverse kinematic matrix, thus:

$$\begin{bmatrix} \Delta\dot{q}_1 \\ \Delta\dot{q}_2 \\ \Delta\dot{q}_3 \\ \Delta\dot{q}_4 \end{bmatrix} = \begin{bmatrix} 1/r & -1/r & 0 & R/r \\ 1/r & 1/r & 0 & R/r \\ 1/r & 1/r & -2\pi R/pr & R/r \\ -1/r & 1/r & -2\pi R/pr & R/r \end{bmatrix} \begin{bmatrix} \Delta\dot{X} \\ \Delta\dot{Y} \\ \Delta\dot{Z} \\ \Delta\dot{W} \end{bmatrix} = J^{-1} \begin{bmatrix} \Delta\dot{X} \\ \Delta\dot{Y} \\ \Delta\dot{Z} \\ \Delta\dot{W} \end{bmatrix},$$
(3.16)

where J^{-1} is the inverse Jacobian matrix.

3.6. Selection of driving gears

This section depicts the dimensioning procedure of the driving gears. The robot dynamics should yield the minimum required torques. Such dimensioning can be done through the dynamic characterization of the robot. This means that at first the kinematics of the robot should be derived, and then its dynamic equations to be obtained. However, this dimensioning procedure applies to already known kinematic systems, but this was not the case with DOHMAN because of the questionable reliability of the theoretical defined kinematics due to the lack of heuristic verification. Since the prototype was expected to be built without any dynamics derivation, it was decided to assign case scenarios for calculating minimum required torque for each driving gear (motor and gearhead). For this purpose, two different cases were assigned.

3.6.1. Case 1: Required torque for displacement along *Z* axis

First case refers to an event in which the screw nut through the lead screw pulls the mass of the load in positive *Z* direction (Figure 3-6). The desired linear acceleration in this case is $a_z = 2 * g$ where $g = 9.81$ *m/s²*, i.e. gravitational acceleration.
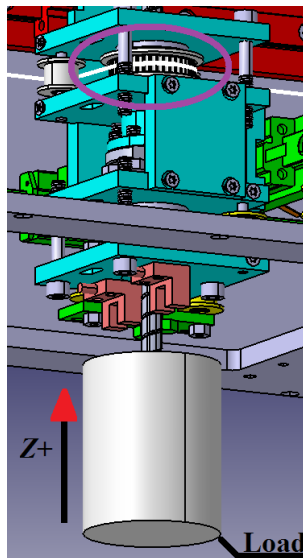
Figure 3-6 Load (illustrated with white cylinder) movement along Z+ direction enabled by rotation of the screw nut (violet ellipse)

The overall mass that should be vertically picked (Z+) is denoted with m_z and it represents a sum of the mass of the lead screw $m_{leads} = 0.02\ [kg]$, the mass of the load i.e. $m_{load} = 0.15\ [kg]$ and certain marginal mass $m_{mar} = 0.02[kg]$. Hence:

$$m_z = m_{slead} + m_{load} + m_{mar} = 0.19\ [kg]. \qquad (3.17)$$

Let us assume that F_z is vertical force that pulls the mass in the upwards direction. In similar way as in [62], the highest F_z is obtained when the mass moves with upward acceleration, thus this is expressed as

$$F_z = m_z * g + m_z * a_z = 3m_z g = 5.5917\ [N]. \qquad (3.18)$$

According to [62] and [63] the total required pulling torque T_z for rotation of the driving pulley attached to the BSS screw nut can be calculated as:

$$T_z = F_z * \frac{p}{2\pi * \eta_{bss}} = 0.0059\ [Nm], \qquad (3.19)$$

where

- $p = 0.006\ [m]$ is the lead screw pitch, and
- $\eta_{bss} = 0.9$ is estimated transmission coefficient of a ball screw [63].

The total required torque provided for the two driving gears T_{dg_total} can be calculated as

$$T_{dg1\_total} = T_z * i_{bt} * \eta_{bt} * K_s = 0.0107\ [Nm], \qquad (3.20)$$

where

- $i_{bt} = 2.5$ Belt transmission ratio calculated as quotient between the number of teeth (40) of the BSS pulley (big pulley) and the number of teeth (16) of the pulley on the driving module (small pulley).
- $\eta_{bt} = 0.9$ is the transmission coefficient of a belt driven mechanisms (Reference Value 0.85-0.95) [64].
- $K_s = 2.0$ is the selected safety factor (Reference Value 1.5-2.0) [64].

The choice of $K_s = 2.0$ is due to the fact that in meso-scale applications, the friction and surface forces become much more dominant and therefore higher safety margin is recommended. The overall required torque T_{dg1_total} should be equally distributed among the two motors that provide the drive. However, usually there are cases in which the distribution of the torque is not always equal. For instance, due certain interpolation there can be a movement in which the motor M1 takes 90 % of the load distribution and the other participating motor(s) take only 10 %. This means that the torque of the driving module should be dimensioned in a way that one motor can withstand the whole

movement of the load with the desired acceleration. Thus the minimum required torque T_{dg1} for each motor in the first case is

$$T_{dg1} = T_{dg\_total} = 10.7\,[mNm]. \tag{3.21}$$

3.6.2. Case 2: Required torque for displacement along *Y* axis

The second case refers to an event in which the load is displaced in positive Y direction (Figure 3-7). The desired linear acceleration in this case is same as in the previous one i.e. $a_y = a_z = 2 * g$.
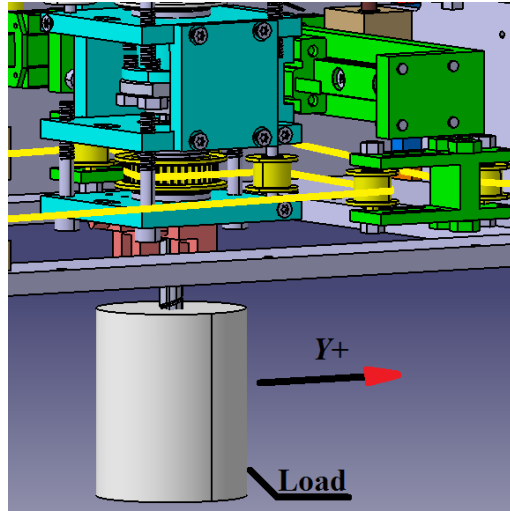
Figure 3-7 Load movement along *Y+* direction

According to [64] the cumulative motor torque T_y can be calculated as sum from the load torque T_L and the acceleration torque T_a, hence:

$$T_y = T_L + T_a. \tag{3.22}$$

To continue, [64] suggests that the load torque T_L mathematically can be expressed as:

$$T_L = m_{ML} * g * d * \frac{(sin\alpha + \mu * cos\alpha)}{2\eta_{bt}} = 0.0399\,[Nm], \tag{3.23}$$

where

- $m_{ML} = m_{BSSA} + m_{axis} + m_{load} = 1.54\,[kg]$ – Mass of linearly displaced load, calculated as sum of the mass of the BSS sub-assembly $m_{BSSA} = 0.6662\,[kg]$, mass of the axis (π-profile and linear guideway) $m_{axis} = 0.624\,[kg]$, and the mass of the load $m_{load} = 0.15\,[kg]$, respectively;
- $d = 0.010\,[m]$ – Effective diameter of the driving pulley;
- $\alpha = 0°$ – Angle of inclination of the belt transmission system; and
- $\mu = 0.48 = 3 * 0.16$ – The multiplier 0.16 stands for frictional coefficient of lubricated and greasy steel to steel sliding surfaces [65]. The factor 3 appears

because of the presence of three sliding surfaces. μ is the overall frictional coefficient from sliding surfaces.

The acceleration torque T_a represents a product from the total moment of inertia $\boldsymbol{J_T}$ and the angular acceleration $\dot{\boldsymbol{\theta}}$ of the driving pulleys.

$$T_a = J_T * \dot{\theta}, \tag{3.24}$$

In fact, the angular acceleration $\dot{\theta}$ is expressed as:

$$\dot{\theta} = \frac{a_y}{r} = 3924 \; [s^{-2}], \tag{3.25}$$

where
- $r = 0.005 \; [m]$ – Effective radius of the driving pulley.

The total moment of inertia J_T is obtained as sum of the total inertia of the moving load $\boldsymbol{J_{ML}}$, small pulleys $\boldsymbol{J_{SP}}$ (10 in total), inertia of the big pulley $\boldsymbol{J_{BP}}$, inertial of the BSS mechanism $\boldsymbol{J_{BSS}}$, inertia of the belt $\boldsymbol{J_B}$ and inertia of the motors and gearheads $\boldsymbol{J_M}$ and $\boldsymbol{J_{GH}}$ (both, 2 in total). Hence:

$$J_T = J_{ML} + 10 * J_{SP} + J_{BP} + J_B + J_{BSS} + 2 * (J_M + J_{GH});$$
$$J_T = 3{,}982 * 10^{-5} \; [kg * m^2], \tag{3.26}$$

where
- $J_{ML} = \frac{1}{4} m_{ML} * d^2 = 3{,}6005 * 10^{-5} \; [kg * m^2]$,
- $J_{SP} = \frac{1}{8} m_{s\_pulley} * d^2 = 2{,}5 * 10^{-8} \; [kg * m^2]$,
- $J_{BP} = \frac{1}{8} m_{b\_pulley} * D^2 = 5{,}4688 * 10^{-7} \; [kg * m^2]$,
- $D = 0.025 \; [m]$ – Effective diameter of the big pulley;
- $J_B = \frac{1}{4} m_B * d^2 = 7{,}5 * 10^{-7} \; [kg * m^2]$ - J_B and m_B are inertia and the mass of the lower belt respectively. The belt mass for the closed loop belt (width of 3 *mm* and length of 1524 *mm*) is 0.03 *kg*, [66].
- $J_{BSS} = \frac{1}{8} m_{BSS} * d^2 = 1{,}35 * 10^{-6} \; [kg * m^2]$ - mass of the BSS mechanism alone is $m_{BSS} = 0.054 \; [kg]$,
- $J_M = 4.09 * 10^{-7} \; [kg * m^2]$ – Inertia of Maxon brushless motor EC22 with power of 100 *W* [67].
- $J_{GH} = 0.5 * 10^{-7} \; [kg * m^2]$ – Inertia of Maxon gearhead compatible with the mentioned motor [68].

The selection of the aforementioned inertias of the motor J_M and gearhead J_{GH} is justified by the fact that as high as possible inertias needed to be selected. A motor with power of 100 *W* was considered as motor with very high inertia based on the experience in already implemented manipulators in the previous work within the project portfolio of Microfactory RG.

Nonetheless, the acceleration torque T_a is:

$$T_a = J_T * \dot{\theta} = 0.1563 [Nm]. \tag{3.27}$$

Substituting (3.23) and (3.27) into (3.22) and thus adding the safety margin K_s, the minimum required drive torque T_{d2} for this case will be:

$$T_{dg2\_total} = T_y * K_s = 392.3 \, [mNm] \tag{3.28}$$

The linear movement along *Y*-axis is obtained by rotation of all four motors as shown in the inverse kinematic transformation. However, two of the motors (M1 and M2) are causing the displacement along *Y* and the other two (M3 and M4) are just compensating the rotation of the big pulley of the Upper *H'*. The displacement is a result of equal torque distribution between the first two driving gears. However, as explained before in case 1, one driving gear should be able to withstand the whole minimum required torque because of the fact that the torque distribution is usually unbalanced in axes interpolation. Hence the minimum required torque T_{dg2} for each motor in the second case is

$$T_{dg2} = T_{dg2\_total} = 392.3 \, [mNm]. \tag{3.29}$$

Considering the two examined cases the overall minimum required torque is the maximum of the two, thus:

$$T_{dg} = \max(T_{dg1}, T_{dg2}) = T_{dg2} = 392.3 \, [mNm] \tag{3.30}$$

The MATLAB code for calculation of both cases is given in Appendix 5.

3.6.3. Selection Method

Two producers of motion drive components were considered i.e. Maxon motors [69] and Faulhaber [70]. Many possibilities and combinations have been examined and five are presented in the Table 3-6. The selection criteria for choosing driving gears are maximum output torque, top linear speed, resolution, maximum linear uncertainty, and price.

Maximum output torque is considered as more valuable than top speed because it enables heavier objects to be manipulated as well as to achieve higher accelerations. Usually in manipulation tasks the acceleration is more appreciated rather than the top speed because in small workspaces the top speed is rarely achieved. The linear resolution and maximum linear uncertainty are parameters that directly influence the performance parameters such as accuracy and repeatability of the robot, and they should be taken with high consideration. Linear resolution is the smallest linear incremental step that the robot can perform and maximum linear uncertainty is the highest deviation that the robot can undergo in one direction.

Table 3-6 Comparison of combinations

	Combination 1	Combination 2	Combination 3	Combination 4	Combination 5
Motor	Maxon EC 22 Ø22 mm, brushless, 100 Watt	Maxon EC 22 Ø22 mm, brushless, 100 Watt	Faulhaber 2250…BX4+Encoder	Faulhaber 2250…BX4+Encoder	Faulhaber 2250…BX4 CSD/CCD
Gearhead	Maxon GP 22 C # 143974	Maxon GP 22 C # 143977	Faulhaber 22f Series	Faulhaber 22f Series	Faulhaber 22f Series
Motor nominal torque	40	40	27	27	20
Gearhead efficiency	0.90	0.90	0.75	0.75	0.75
Gearhead reduction	14.00	20.00	19.00	25.00	25.00
Number of Encoder Pulses	512	512	1024	1024	1024
Max. backlash [°]	**3.50**	**3.50**	3.50	3.50	3.50
Max. output torque [mNm]	392.00	560.00	384.75	506.25	375.00
Max linear speed [mm/s]	299.19	209.43	137.79	104.72	83.77
Linear resolution [µm]	1.1	0.8	0.4	0.3	0.3
Linear Backlash [µm]	0.31	0.31	0.31	0.31	0.31
Max. linear uncertainty [µm]	1.4	1.1	0.7	0.6	0.6
Combination Length [mm]	95.00	95.00	102.40	102.40	102.40
Motor Price (€)	193.6	193.6	267.50	267.50	561
Gearhead Price (€)	90.32	90.32	125	125	125
Encoder Price (€)	82.4	82.4	-	-	-
Driver Price (€)	175	175	175	175	/
Total Price (€)	541.32	541.32	567.50	567.50	686.00

All of the mentioned parameters, except the price, are calculated based on the information from the datasheets of the components. These parameters which serve as selection criteria are enlisted in the first column of the Table 3-6 and they are colored in grey. The maximum output torque is function of the motor torque, gearhead reduction ratio and gearhead efficiency. The maximum linear uncertainty is a sum of the linear resolution and linear backlash. The linear backlash is directly depended on the maximum motor backlash. The computation method of linear top speed and linear resolution are elaborated in Section 0.

From the Table 3-6, it can be seen that the second combination feature best output torque. The first combination, however, has top linear speed. The maximum backlash can be neglected as a parameter since combinations 1 and 2 contain the average back-lash (true value is 1.2) in their datasheet whereas the remaining three combinations con-tain the maximum backlash. The maximum backlash is involved in the calculations for maximum linear uncertainty, thus this parameter for the first two combinations is as-sumed to have the same value, i.e. 3.5 (bolded values in the row of Max. backlash in Table 3-6), as in the remaining three combinations.

Combinations 4 and 5 feature the best linear resolution of 0.3 μm. This parameter af-fects the overall accuracy and repeatability performance of DOHMAN. The combina-tion 5 differs from the other combinations in a way that motor driver is already integrat-ed within the motor structure. In addition to the technical parameters, the selection of the particular combination also depends on the price. Combinations from 1 to 4 are cheaper for more than 100 euros in comparison with the combination 5. In addition, the later three combinations lack the information of the price for encoders. Since four driv-ing modules were expected to be ordered, the price difference should be considered with certain regard as well.

After examining all the aspects of all of the combinations, the best suitable combina-tion is the combination 2. The selection of this combination is justified by the maximum output torque, the good top linear speed and the lowest cost. Additionally the selection of this combination is supported by the fact that Microfactory RG had good experience working with motion drive components from Maxon motors. The advantage of combi-nation 2 over the combination 1 is the maximum output torque since it is more appreci-ated than the speed as explained before.

Four Maxon EPOS 24/2 [71] motor drivers or amplifiers were selected for driving the selected motors.

3.7. Theoretical performance

This section encompasses the theoretical estimations of the maximum velocities and incremental steps (resolutions) along each axis, as well as the overall workspace.

Maximum velocities

The maximum linear velocities along X and Y axes can be calculated according to the following equation:

$$V_{X\,max} = V_{Y\,max} = 2\,\pi\,r\,\frac{n_{GH}}{60 * i_{gh}} = 210.4\,\left[\frac{mm}{s}\right], \tag{3.31}$$

where

- $V_{X\,max}, V_{Y\,max}$ – Maximum linear velocity along X and Y, respectively.
- $n_{GH} = 8000\ rpm$ – Maximum recommended number of rotations per minute on the input shaft of the gearhead.
- $i_{gh} = 20$ – Reduction rate of the planetary gearhead.

Before calculating the *maximum linear velocity $V_{Z\,max}$*, it is required to calculate the maximum angular velocity w_{max} of the screw/spline nut. As function from the later velocity and the lead screw pitch p, one can calculate the top linear speed along Z. Hence:

$$w_{max} = \frac{V_{X,Y\,max}}{R} = 16.8\,\left[\frac{rad}{s}\right] = 2.6\,[rev/s], \tag{3.32}$$

$$V_{Z\,max} = p * w_{max} = 100.8\,\left[\frac{mm}{s}\right]. \tag{3.33}$$

Resolution

Resolution is the smallest incremental step that the TCP can realize. The linear resolution along X and Y axes can be calculated according to the following equation:

$$R_X = R_Y = \frac{2\,\pi\,r * 1000}{n_e * i_{gh} * 4} = 0.7\,[\mu m], \tag{3.34}$$

where

- $R_X = R_Y$ – Resolution along X and Y axis, respectively,
- $n_e = 512$ – Number of pulses of the encoder, and
- 4 – Multiplication factor denoting 2 channels, 2 edges per channel of the encoder.

The angular resolution, however, around the W axis can be calculated as

$$R_W = \frac{360}{n_e * i_{gh} * 4 * i_{bt}} = 0.003[°], \qquad (3.35)$$

where $i_{bt} = 2.5$ is the belt transmission ratio. Thus the linear incremental step along Z is

$$R_Z = \frac{p * 1000}{n_e * i_{gh} * 4 * i_{bt}} = 0.05\ [\mu m]. \qquad (3.36)$$

Estimating the resolution is easy and straight forward job due to the common relations among the motor velocity, encoder pulses, belt transmission, gearhead ratio and the multiplication factor. However, accuracy as a parameter is more important than the resolution. The accuracy is very hard to estimate because of the mechanical load characteristics and dynamics involved, so it is preferred to be heuristically measured rather than theoretically derived.

Workspace

Workspace of a robot is the space volume in which a robot is capable to move, and it can be reachable and dexterous. The reachable workspace includes all of the workspace that can be reached in at least one orientation. The dexterous workspace, in addition, is the volume of space in which a manipulator can be arbitrary oriented.

As already explained, the DOHMAN robot is designed to position itself along the Cartesian axes and to perform one orientation around the *Z*-axis. This means that the workspace of this robot is same as the workspace of any Cartesian robot, i.e. cube-like envelop. The dimensions of the workspace of DOHMAN are ~40 x 115 x 50 *mm³*. Because of the unlimited stroke of the rotational axis and the uniformity of the Cartesian workspace, this robot is dexterous within the all reachable workspace.

3.8. Timing belts and pulleys in DOHMAN

Timing belts and pulleys are very common motion transmission components and as such they are coming in various selections for material and tooth profile. Trapezoidal and curvilinear belts are the main two types of synchronous belts. The trapezoidal belt features stress concentration near the root of the tooth and the strain is less in the remaining part of the tooth profile. On the other hand, in the curvilinear belt the strain is almost constant across the whole belt. The most common trapezoidal and curvilinear belt profiles are listed in table below. [72]

Table 3-7 Timing belt profiles [72]

Pitch Profile	Trapezoidal			Curvilinear		
	MXL	XL	L	GT2		
	0,080"	0,200"	0,375"	2 *mm*	3 *mm*	5 *mm*

Some advantages of the curvilinear over the trapezoidal belts are:

- Prevention of tooth jamming due to deeper teeth
- Larger area contact causes smaller unit pressure on each tooth
- Lighter bearing loads due to smaller installation tensions
- Extremely small backlash due to almost complete overlay of the belt tooth profile with the pulley tooth profile (see Figure 3-8)
- Higher positioning accuracy in motion transfer applications due to the minimized backlash (see Figure 3-9)
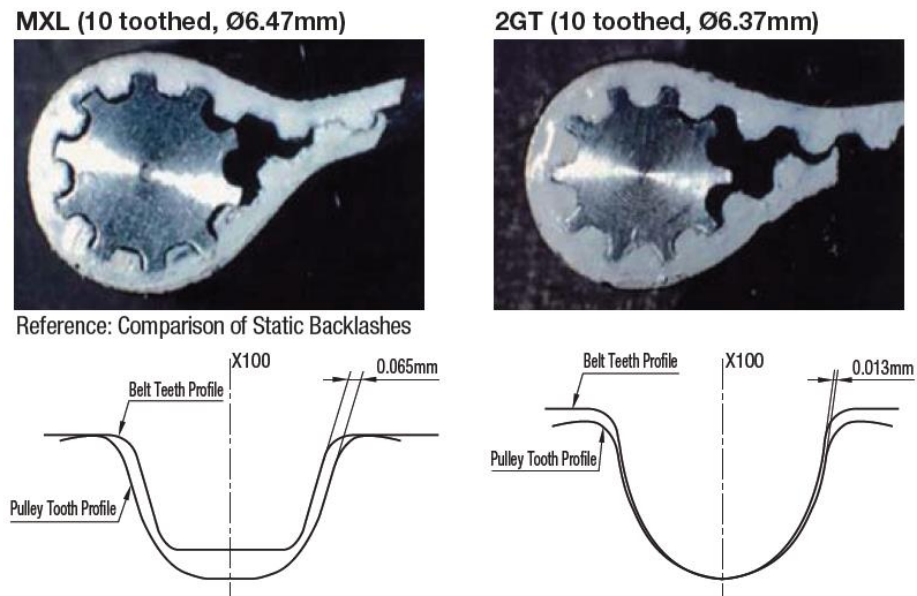
Figure 3-8 Static backlash between MXL belt and pulley (left); Static backlash between GT2 belt and pulley (right) [73]
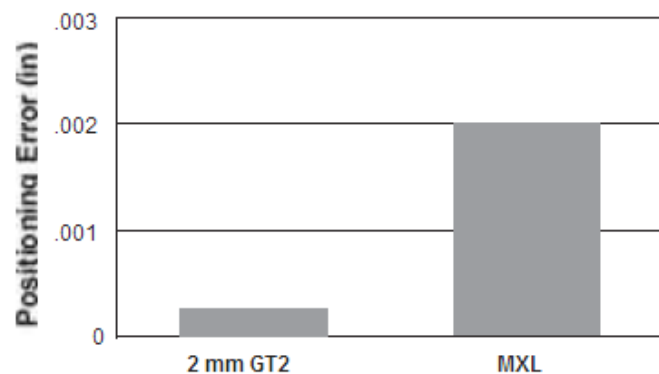
Figure 3-9 Positional error with 2 *mm* GT2 belt (left) and MXL belt (right) in motion transfer application [74].

Taking into consideration all the above mentioned findings, the selected type of belts and pulleys are GT2 with 2 *mm* pitch.

3.8.1. Belt tensioning and belt sizing

Figure 3-4 and Section 3.4 depict the spatial arrangement of pulleys and belts. The tensioning of the first and second levels (yellow and pink belts) is realized by horizontal displacement of the holders of the driving gears as illustrated on the figure below (see

black lines with red arrows). On the other hand, the tensioning of the third level belt (white belt) is a bit more complex and it is NOT contained in the Figure 3-10, but is illustrated on Figure 3-11.
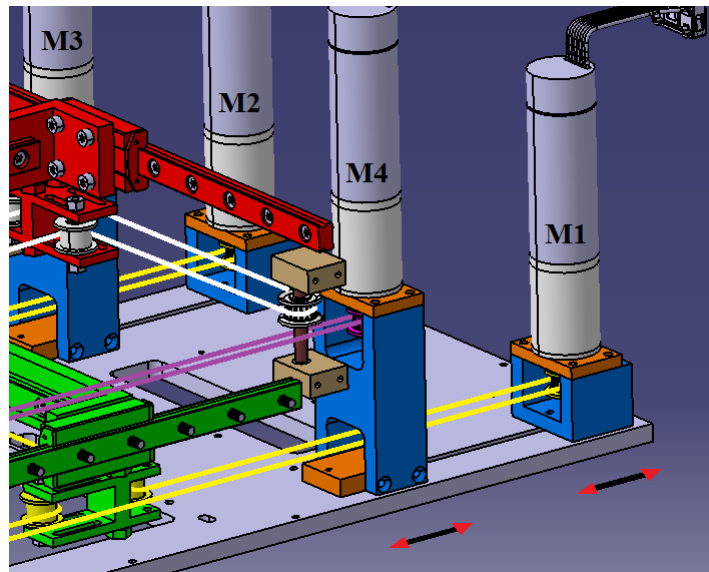
Figure 3-10 Belt tensioning of the first and second belt levels

The *belt tensioner* consists of two idle pulley arrays; the first one contains three idle pulleys that are integrated into non-moving frame, and the second pulley array contains two toothed idle pulleys that are integrated into moving frame. The hollow thread in the moving frame enables a M4 screw to fit inside and thus to allow displacement of the part by rotation of the screw. The tensioning is realized by displacing the moving frame (Figure 3-11 b). One incremental movement of the moving frame corresponds to four tightening incrementals on the belt. The linear displacement is eased by cylindrical rods that serve as linear guideways. The attachment of the belt tensioner within the structure of DOHMAN is discussed in Section 3.10.

a)   b)
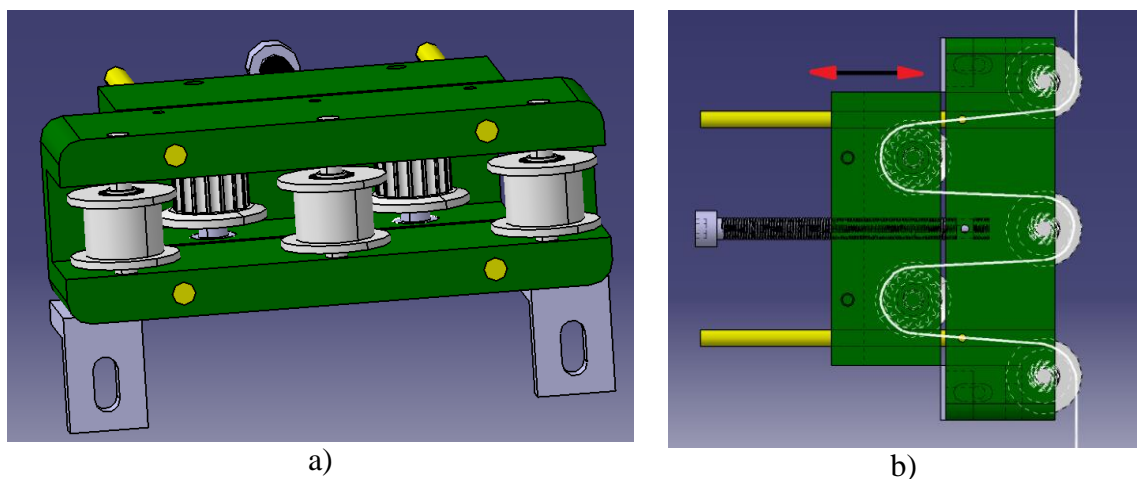
Figure 3-11 Belt tensioner sub-assembly (belt not included) (a) Shaded top view of the belt tensioner (b)

3.8.2. Belt size calculations

After a belt and pulley profile selection is done and tensioning mechanism has been designed, a belt sizing is a sequential phase needed before purchasing the complete transmission structure. At first, this phase started with calculating the overall circumference of both H-like belt structures and the middle belt structures, then the margins for the tightening are added (upper H' and middle level belts) or subtracted (lower H'), and the phase ends with finding available belt length from suppliers.

Lower H belt structure

An approximation of the overall circumference of the lower H-like belt structure can be expressed as:

$$C_{LH} = 2x_{lh1} - x_{lh5} + 4x_{lh2} + 4x_{lh3} + 2x_{lh6} + 3.5C_{sp} \\ + 2x_{lh4} + 0.5C_{bp} = 1695,2 \ [mm]; \tag{3.37}$$

where

- x_{lh1} to x_{lh7} are distances shown on Figure 3-12. Their values are listed in Appendix 6.
- $C_{sp} = 31.4 \ [mm]$ – circumference of small pulley with $d = 10 \ [mm]$.
- $C_{bp} = 78.5 \ [mm]$ – circumference of big pulley with $D = 25 \ [mm]$.
- C_{LH} – Overall circumference of the lower H-like belt structure.

The maximum size of x_{lh7} is 43 *mm*, hence the minimum value of the overall circumference C_{lH}' is:

$$C_{LH}' = C_{LH} - 4x_{lh7} = 1523,2 \ [mm]. \tag{3.38}$$

Considering the equations above, the selected belt length should be between 1523 and 1695 *mm*. Available belt lengths from suppliers are 1524 *mm* and 1558 *mm*.
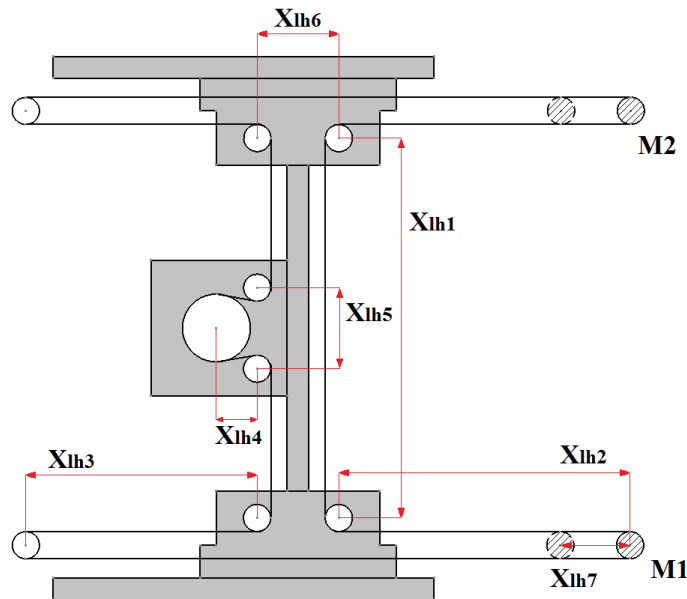
Figure 3-12 Distances in lower H-like belt structure measured from the DOHMAN's CAD product

Upper H belt structure

In a similar fashion, an approximation of the overall circumference of the upper H-like belt structure can be expressed as:

$$C_{UH} = 2x_{uh1} - x_{uh5} + 4x_{uh2} + 4x_{uh3} + 2x_{uh6} + 3.5C_{sp}$$
$$+ 2x_{uh4} + 0.5C_{bp} + (2C_{sp} + 4x_{uh7}) - x_{uh8}, \tag{3.39}$$

where

- x_{uh1} to x_{uh6} are distances shown on Figure 3-13, and their values are given in Appendix 6.
- Illustration of x_{uh7} and x_{uh8} distances as well as their values can be also found in Appendix 6.
- C_{UH} – Overall circumference of the upper H-like belt structure.
- The addition $(2C_{sp} + 4x_{uh7})$ refers to the belt length within the belt tensioner.

Thus:

$$C_{UH} = 1182 \, [mm]. \tag{3.40}$$

The maximum tensioning margin within the belt tensioner is 20 *mm* (maximum displacement of the moving part), hence the maximum value of the overall circumference C_{UH}' is:

$$C_{UH}' = C_{UH} + 4 * 20 = 1262 \, [mm]. \tag{3.41}$$

Considering the equations above, the selected belt length should be between 1182 and 1262 *mm*. Such available lengths are 1228 *mm* and 1256 *mm*.
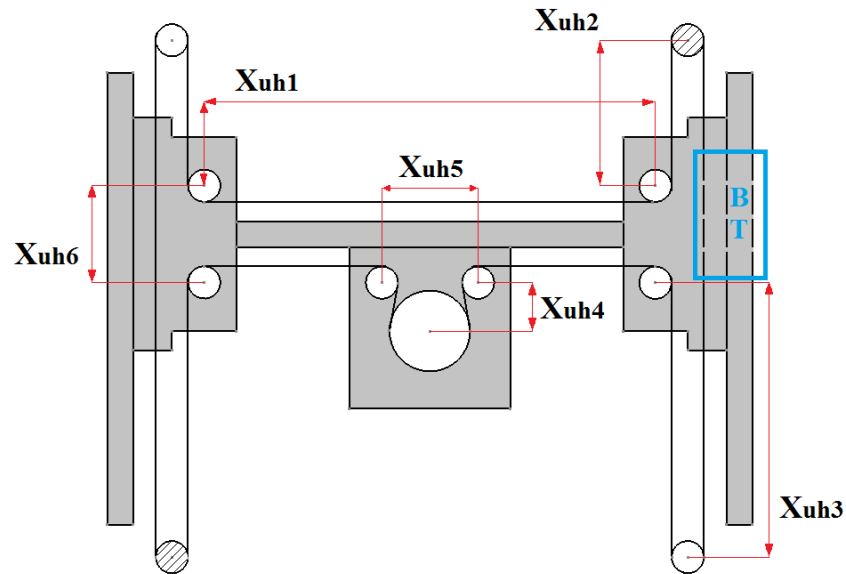
Figure 3-13 Distances in upper H-like belt structure measured from the DOHMAN's CAD product. BT denotes belt tensioner.

Middle level belts

The middle level belts are independent from each other. The belt size for the long middle belt can be dimensioned as:

$$C_{ML1} = 2x_{m1} + C_{sp} = 545.4 \ [mm]; \tag{3.42}$$

$$C_{ML1}{}' = C_{ML1} + 2x_{mar} = 575.4 \ [mm]; \tag{3.43}$$

where

- $x_{m1} = 257 \ mm$ is the distance between the axis of the driving pulley to the axis of the driven pulley as illustrated on Figure 3-14 a),
- C_{ML1} - Circumference of the first middle belt, Figure 3-14 a),
- $x_{mar} = 15 \ mm$ – The estimated distance for moving the holder of the driving gear in order to tighten the belt, and
- $C_{ML1}{}'$ - Circumference with added margins i.e. maximum belt lengths.

In a similar fashion, the second (short) middle belt can be dimensioned as:

$$C_{ML2} = 2x_{m2} + C_{sp} = 85.4 \ [mm]; \tag{3.44}$$

$$C_{ML2}{}' = C_{ML2} + 2x_{mar} = 115.4 \ [mm]; \tag{3.45}$$

where

- $x_{m2} = 27 \ mm$ is the distances between the axis of the driving pulley to the axis of the driven pulley, shown on Figure 3-14 b),
- C_{ML2} - Circumference of the second middle belt, Figure 3-14 b), and
- $C_{ML2}{}'$ - Circumference with added margins i.e. maximum belt length.

a)   b)
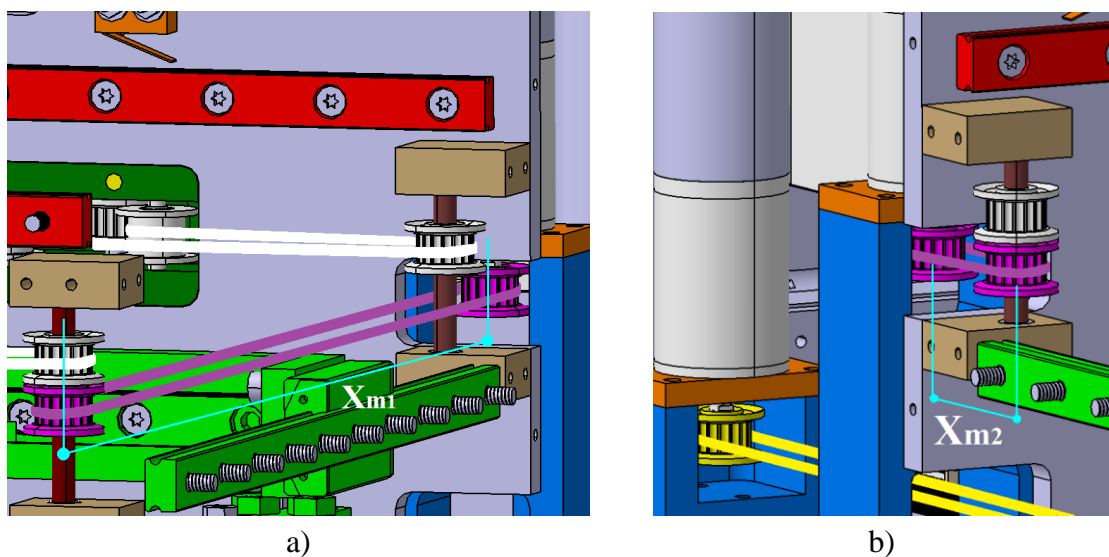
Figure 3-14 Middle level belts; long middle belt (a) and short middle belt (b)

Suitable and off-the-shelf available belt length for the first middle level belt is 558 *mm*, and for the second 100 *mm*.

The belt elongations or belt stretch occurs when the belt becomes tensioned. Since the belt elongation is very small for the fiberglass reinforced belts (as the selected ones), the elongation factor was not considered during the dimensioning of the belts. For instance the belt elongation for the longest belt (1524 *mm* in length) according to [75] is as follows:

$$Belt\ Elongation = \frac{Belt\ Length * F_u}{Tensile\ Modulus} = 0.61\ [mm];\qquad(3.46)$$

where the tensile load F_u is

$$F_u = m_{TL} * a_y + m_{TL} * g * \mu = 32\ [N];\qquad(3.47)$$

and $Tensile\ Modulus = 79200\ [N]$ as parameter for all chosen belts [75].

3.9. Sensors and limit switches for safety and homing

The safety maintenance and homing strategy in DOHMAN can be realized by the limit switches and/or index pulses of the linear encoders. There are six limit switches in total. Figure 3-15 illustrates two limit switches along each of the *X* and *Y* axis that are used to indicate the end of the displacement. X-pos and X-neg are limit switches for limiting movement along *X*, and Y-pos and Y-neg are limit switches for limiting movement along *Y*. These limit switches are triggered by the linear sliders. One homing approach is to use one of the two limit switches along each axis.
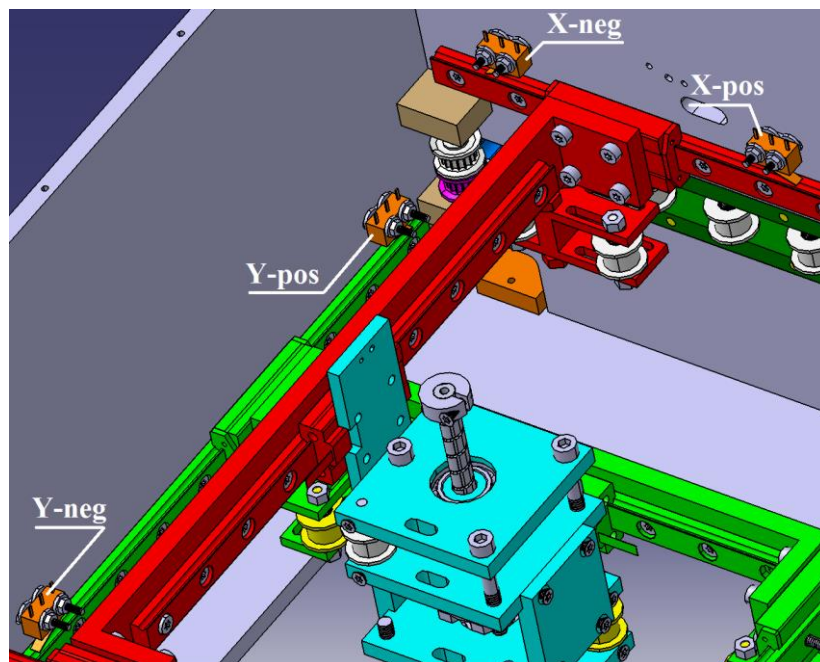
Figure 3-15 Homing of *X* and *Y* axes (belts not illustrated)

Another approach of homing *X* and *Y* axes is by using the index signals from the linear encoders from each axis. Therefore it can be inferred that there are several homing strategies for the first two axes.

For homing *Z* axis and *W* angle, one very innovative approach has been designed. Figure 3-16 shows the lower part of the BSS sub-assembly. The most important components in this context are the optical fork sensors (1) and (2); and the 270° arc profile (3). The homing strategy for *Z* axis and *W* angle is explained below:

1. Move the lead screw up until optical switch (1) **or** (2) turns ON.
2. Z+ incremental movement enough to actuates the limit switch(es)
3. Rotate the lead screw in CW direction until the optical switch (1) encounters rising edge i.e. alters from OFF to ON.
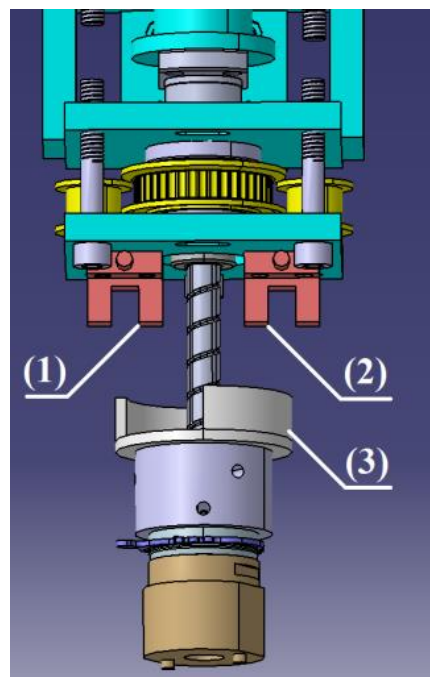
Figure 3-16 Homing of *Z* and *W*

Please note that the above algorithm can be modified and thus new homing strategies for *Z* and *W* can be obtained. The advantages of the innovative layout are: efficient use of space for mounting sensors, avoiding huge loss in the overall *Z*-axis movement, and no cabling issues (cables do not extract/retract or stretch while performing displacements along *Z* and *W*). The implemented homing algorithm is explained in greater detail in Section 4.2.

The selection of both types of switches, the basic and the optical fork switch, was done by analyzing the available switches from all available electronics suppliers in Finland, i.e. Etra [76], Farnell [77] and Omron [78]. The basic switch [79] was chosen from Omron because of the smallest dimensions. The optical fork switch [80] was also chosen from Omron because this was the only supplier that offered this kind of switch with appropriate mounting capabilities and signal conditioning on board.

3.10.　　DOHMAN's CAD model at a glance

This section finalizes the elaboration of the DOHMAN design by brief illustration of DOHMAN's CAD model. Therefore, a self-explanatory CAD of the robot is illustrated on Figure 3-17. As already explained in Section 3.4, the structures (1), (2) and (3), i.e. the upper and lower *H'*-gantry mechanisms and the BSS sub-assembly respectively, form the core mechanical construction of DOHMAN. Idle GT2 pulleys are attached to custom designed axes that reside on different kind of axis couplings (white ellipses on the figure). The axis couplings are tightened to the enclosing plates of the module, please see Appendix 7 for greater explanation of the DOHMAN's enclosing.
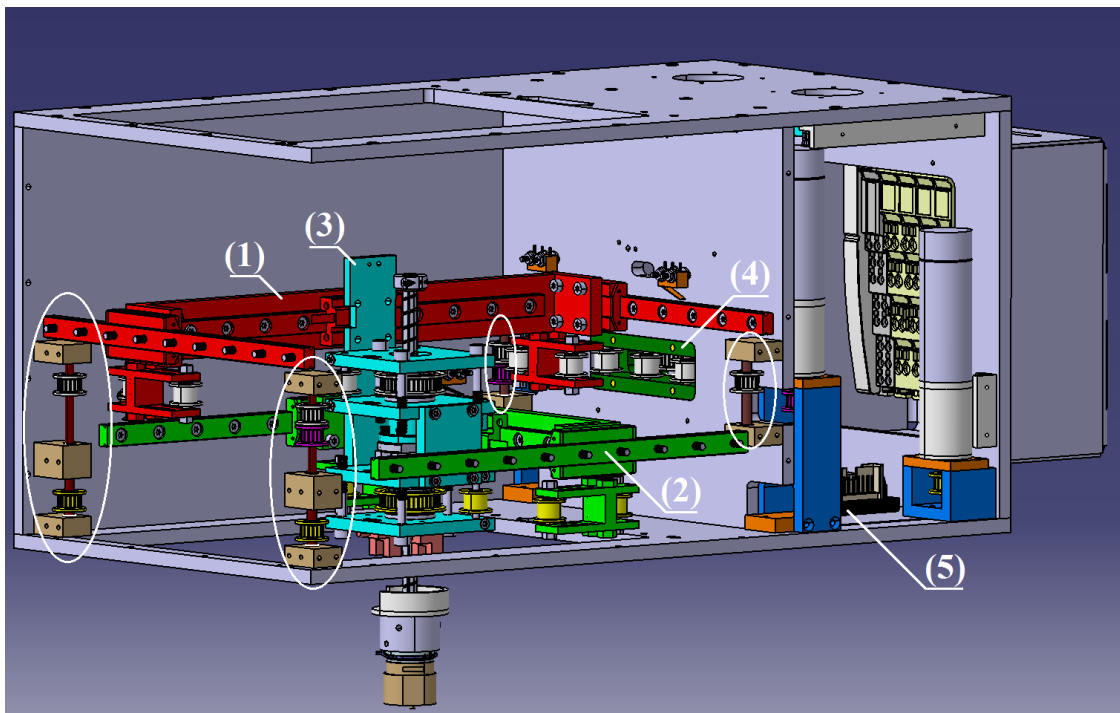
Figure 3-17 CAD of DOHMAN module (hidden visibility of belts and some enclosing plates)

Please note that the middle axis coupler (the two bigger ellipses) enables independent rotation of the both axes attached to it, thus axes are decoupled.

The belt tensioner mechanism (4) is attached to the middle PM plate together with X-pos/neg limit switches, colored in orange. Two motor amplifiers (5) are positioned on the bottom plate, and the other remaining two are attached on the back of the middle plate (please see Figure 8-6). The amplifiers together with the motors are located behind the middle PM plate or into the so called (distributed) actuation part of DOHMAN.

4. CONTROL AND VISION

This chapter depicts the control and vision aspects in the developed microfactory cell. At first Section 4.1 explains the control architecture of the overall cell. Next, the motion control design of DOHMAN is elaborated in Section 4.2 and Section 4.3 depicts the control and software implementations. To continue, dimensioning of the machine vision setup is examined in Section 4.4, and the chapter ends with CAD illustration of the spatial integration of the control and vision parts, Section 4.5.

4.1. Control architecture

Figure 4-1 illustrates the overall control hardware architecture of the microfactory cell. The base module has one output device (LED stripes) that is connected to its IO module. The DOHMAN has six limit switches as digital inputs connected to its IO modules which in addition reserve one digital slot for the object sensor. The object sensor is the sensor that should detect weather the gripper has gripped the object or not. The selection of the sensor and its attachment are not part of this thesis. Two linear encoders as three channel digital pulse inputs are connected to the DOHMAN IOs as well, and two fan blowers are connected directly to the power supply line, thus no IO slots are dedicated for them. Two output slots are being reserved for the vacuum valves. The process module also contains four motors with four drivers which are connected to the main controller through a CANopen interface.
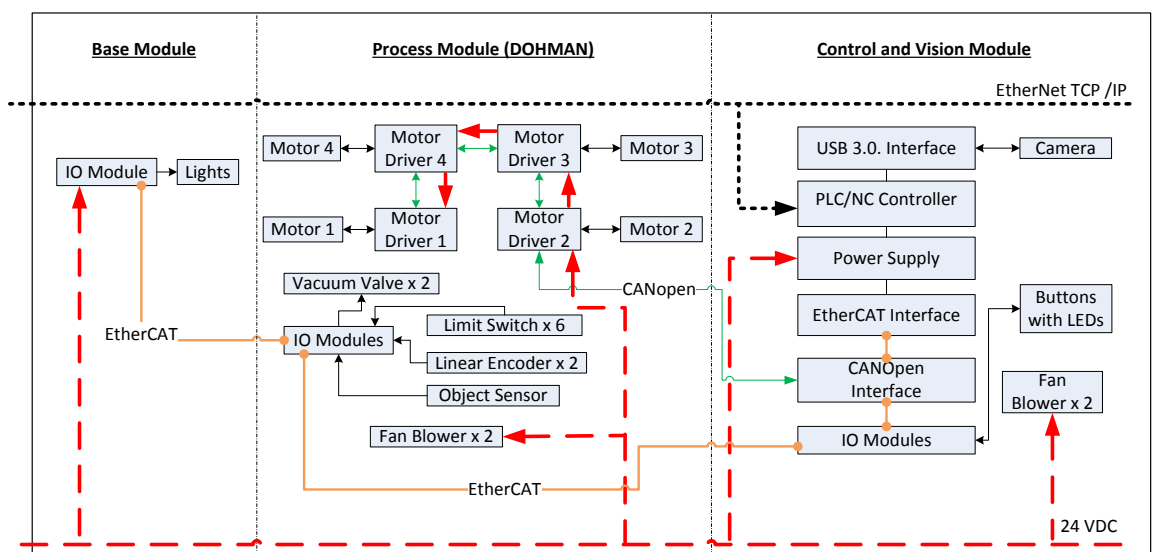
Figure 4-1 Microfactory cell control hardware architecture

The PLC/NC is a master control unit that gathers the data from all input devices (limit switches, linear encoders, camera) and according to a certain logic outputs control decisions that are delivered to the output devices (motors, LEDs, vacuum valves) in the base and process modules through the communication interfaces. Therefore, it is evident that the control is arranged in master/slave configuration by utilizing tree topology.

4.2. Motion control design

Figure 4-2 illustrates a typical motion control design in controlling positioning tables, CNC mills and/or other conventional mechatronic positioning systems with Cartesian layout in which each axis is driven by one single motor. At first, the user sets the desired path and speed of the TCP in the base coordinate system. The input instructions are given for example in G-code, i.e. DIN 66025, and send to the G-code interpreter. The G-code interpreter computes the position, velocity and acceleration profiles of each axis and sends them to numerical controller (NC). Based on the received data, the NC outputs the velocity control commands to the driver/amplifier that drives the motor. Position encoder (motor encoder or linear encoder or other displacement measuring device) is used to measure the actual position of the axis displacement and provide feedback information to the driver and the NC. This motion control design works in closed loop control cycle. It performs fast closed-loop control with simultaneous position, velocity, and trajectory maintenance on each axis. The control loop handles closing the position/velocity loop based on feedback, and it defines the response and stability of the system.
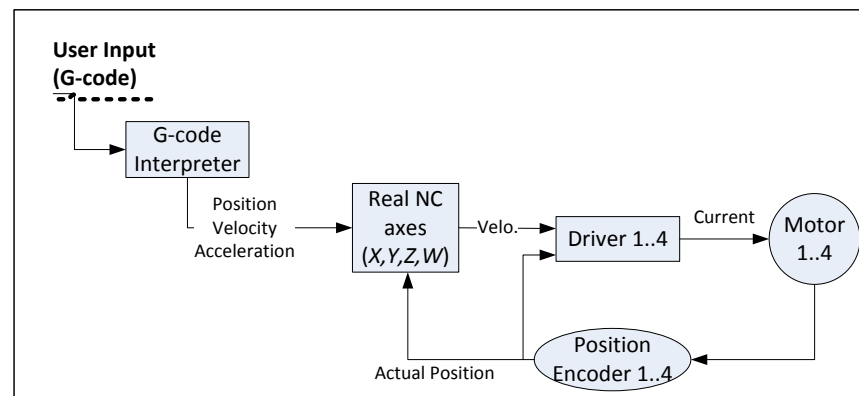
Figure 4-2 Block diagram of typical motion control design of four DOF positioning device

Unlike in the typical Cartesian positioning systems, the motion control in DOHMAN is designed in different way, illustrated on Figure 4-3. The idea behind this design is to compute kinematic transformations before sending control commands to the motors and before receiving feedback data from their encoders. The reason why the kinematic transformations are integrated into this motion control scheme is because for driving each axis two motors (for Z) and all four motors (for X, Y and W) need to be working. The NC virtual axis through the self-implemented kinematic transformations (coded in the PLC) generates the interpolating paths and sends them to the NC real axis, which on

the other hand, outputs the velocity and current control commands to the driver. In a similar fashion, the feedback link of the actual position goes to the real axis NC and through the forward kinematic transformation to the virtual NC axis.
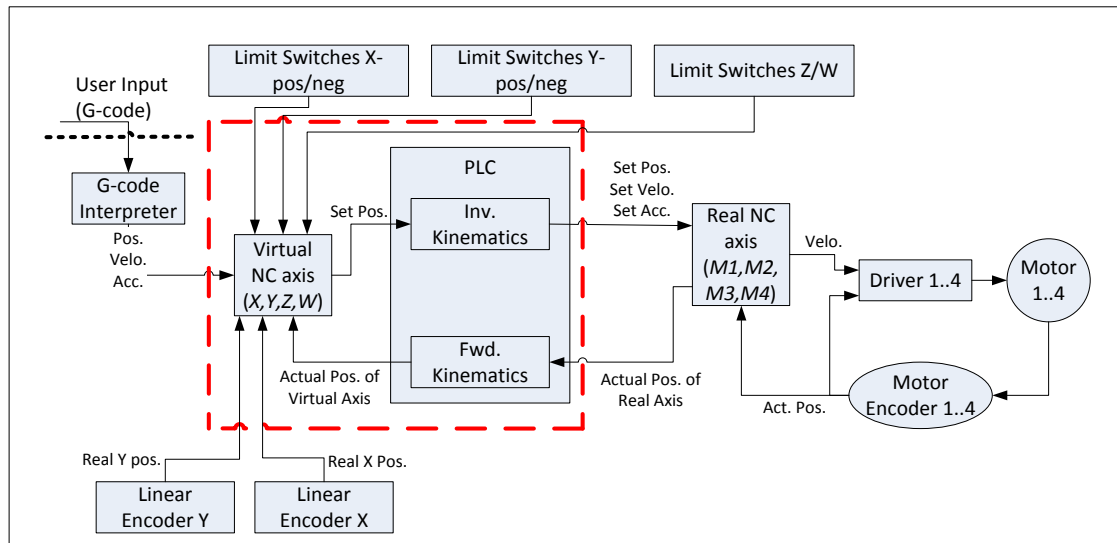
Figure 4-3 Motion control design in DOHMAN

This motion control design features multiple feedback devices because of the complexity in its mechanical structure. This means that beside the motor encoders a linear encoders along *X* and *Y* axes are used as well. This is done to ensure that the motors along with the mechanical system perform the movements in the way they should. Although feedback devices offer position feedback, sometimes special feedback information, such as vibration sensor, needs to be sent back to the controller. However, such sensor is not used in this control design.

Last but not least, the designed motion control system is capable of performing safety maintenance, fault detection and initializing sequence (homing). The safety maintenance and the fault detection refer to stopping the motor(s) when limit switches are encountered or safe emergency stop button is pushed or the drives fail from unknown reasons. Homing, in addition, is an initializing sequence that brings each axis to its initial (zero) position.

Homing

There are two different position reference systems, depending on which position referencing system is used. An *absolute reference system* yields an absolute position (once the machine is turned on) that is unique over the whole travel path. Reference system as such is calibrated once and set via a persistently stored position offset. On the other hand, *relative reference systems* provide an ambiguous position value after machine is turned on that must be calibrated through homing. According to [81] homing represents an axis initialization run that determines the correct actual position of the axis by means of a reference signal. Reference signal comes from a limit switch which is triggered at known and unambiguous position along the travel path. Image A on Figure 4-4 shows a

schematic diagram of a homing procedure with individual velocity profile phases, and images B and C show the position and velocity profiles during homing.
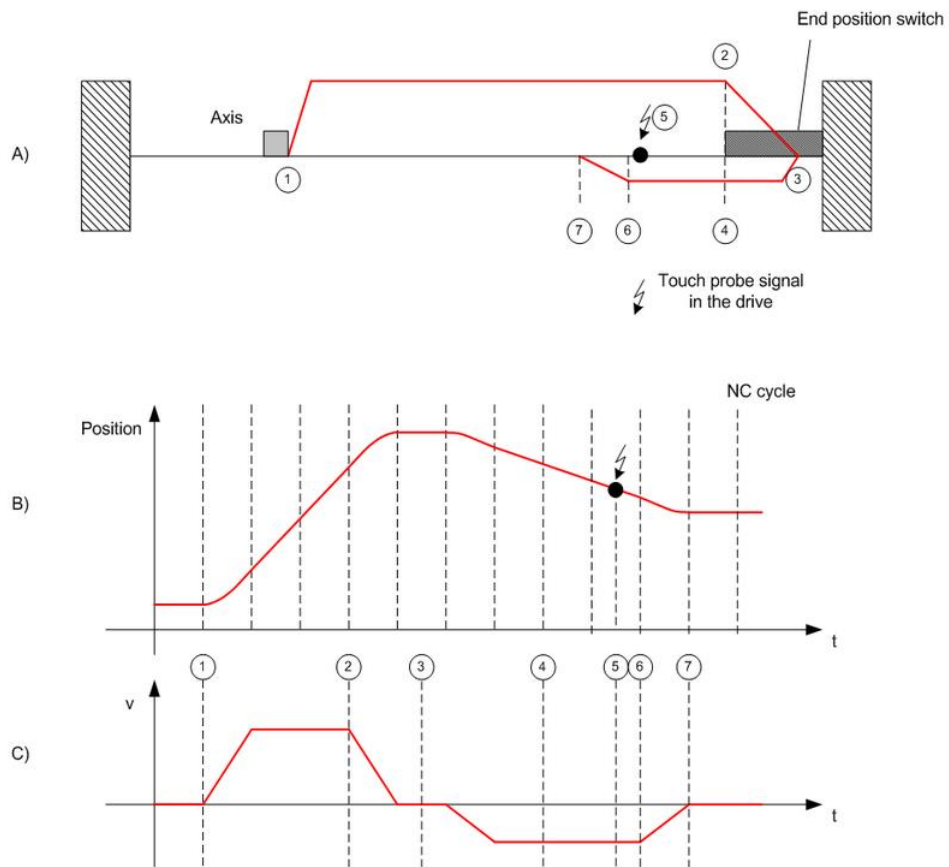
Figure 4-4 Schematic diagram of a homing procedure with individual velocity profiles (A); position profiles (B); and overall velocity profile (C). [81]

1. Axis is in a random position (1) when the machine is switched ON.
2. Homing is initiated, i.e. the axis moves towards the end position switch.
3. When the end position switch is detected, the axis stops and reverses.
4. The axis travels away from the end position switch and detects the falling edge of the reference signal.
5. Depending on the reference mode setting, the axis continues and searches for a sync pulse or another distinctive event. This step may be omitted where appropriate.
6. The occasion is detected and the specified reference position is set.
7. The axis stops at a certain distance from the reference position, which was set shortly beforehand with maximum precision.

The homing strategy in DOHMAN can be arranged in the relative measurement system manner in several ways by combining the index signals from the linear encoders together with the limit switches along the *X* and *Y* axes. Although there were several possibilities, it was decided to use the positive limit switches alone because of their correct positioning at the end of each axis. Therefore, the implemented homing strategy has the following procedure:

1. Homing *Z*:
   - o Drive *Z*+ until optical switch (1) **or** (2) is triggered.
2. Incremental Z+ movement enough for triggering optical switch(es) ON; This way, we are sure that sensors will definitely act while homing *W*.
3. Homing *W*:
   - o Rotate the lead screw in CW direction until the optical switch (1) encounters falling edge i.e. alters from ON to OFF.
4. Homing *Y*:
   - o Drive *Y*+ until limit switch Y-pos turns OFF.
5. Homing *X*:
   - o Drive *X*+ until limit switch X-pos turns OFF.

The advantages of this homing strategy layout especially for *Z* and *W* axes is the efficient use of space for mounting the optical fork sensors, avoiding huge loss in the overall Z-axis movement, and no cabling issues (cables do not extract/retract or stretch while performing displacements along *Z* and *W*) in the moving structure.

4.3. Control hardware and software implementation

4.3.1. Control hardware implementation

The control implementation in all the modules of the cell is realized with industrial off-the-shelf controller and IO modules. Although this kind of control implementation is not the most appropriate for micro-production systems due to the large size of the industrial controllers, it is very convenient because of the standardized software, modular input/output (IO) devices and verified robust hardware components. The control implementation as such allowed the focus of the development time to be dedicated to the mechanical construction and implementation rather than to design the control electronics.

IO dimensioning of the complete cell was done prior to the control selection and its listing can be found in Appendix 8. The selected master controller is Beckhoff embedded PC, series CX2030 [82] which comes with two Ethernet and four USB 2.0 connections on board, Figure 4-5. The Ethernet communication is used for setting the controller configuration through a PC and also having the possibility to establish a remote HMI, a USB 2.0 port can be used for communication with the camera. In fact, the selected camera features USB 3.0 (Chapter 4.4). Therefore CX2500-0070 [83] module with four USB 3.0 slots was added in order to take a full advantage of the USB 3.0 interface. The CX2500-0070 module was added to the left-hand side of the controller and the communication between the controller and the module was realized via PCI Express. Similarly, the communication between the controller and the modules added to the right-hand side of the controller is done through EtherCAT. The CANopen communication is enabled by EL6751 [84] fieldbus master and it is utilized for motion control of the motors through the motor drivers. EL1819 [85] digital input module is used for receiving the Boolean data from the five buttons and EL2828 [86] digital output module

is used for controlling the LEDs in the buttons. The power supply to the controller and the modular IOs is provided through CX2100-0004 [87]. At the right-hand side end of the array, an IO module EK1110 [88] was placed in order to enable EtherCAT communication.
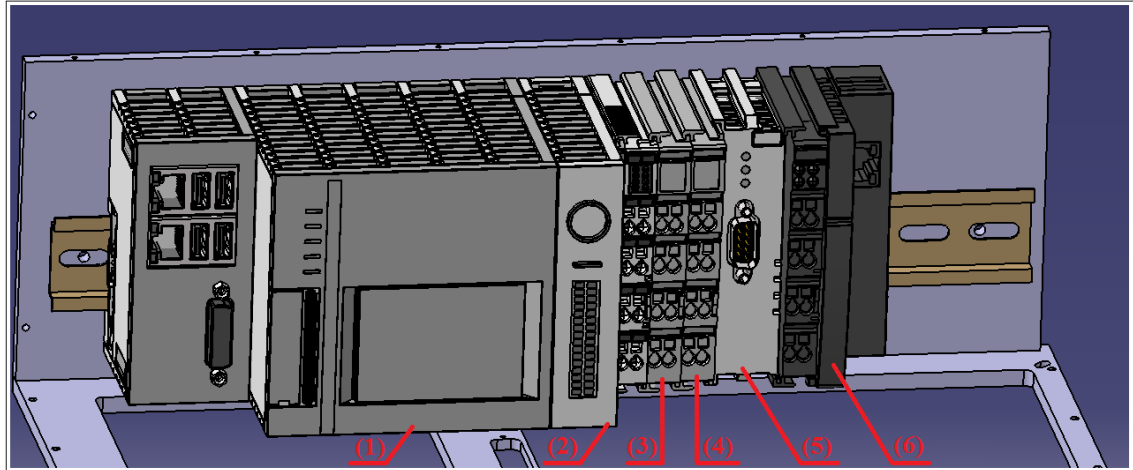
Figure 4-5 CAD illustration of the control hardware; USB 3.0 module not included; Beckhoff CX2030 (1), Beckhoff CX2100 (2), Beckhoff EL 1819 (3), Beckhoff EL2828 (4), Beckhoff EL6751 (5), Beckhoff EK1110 (6).

Additionally, this IO module terminates the array, meaning that prevents any damages caused by accidental shortcut for the internal bus system circuitry. All these control components are attached to a DIN rail and mounted on the right plate of the control and vision module (Section 4.5). The control component arrangement as such encompasses the control sub-module.

The selected distributed IOs in the process module are enlisted below. Each numbered item corresponds with its CAD element on Figure 4-6.
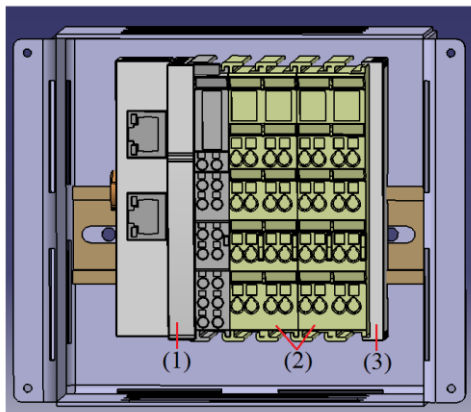
Figure 4-6 CAD of the IO modules located in process module

1. Beckhoff EK1818 [89]. This module contains 8 digital inputs 24V DC, four digital outputs 24V DC, 0.5A, and E-bus power supply with maximum current of 1 A. The six limit switches and the object sensor are connected to this module.

2. Beckhoff EL5101 [90]. This module represents incremental encoder interface with 16 bit differential input, and it serves for acquiring three channels of data from the each linear encoder.

3. Beckhoff EL 9011 [91] is terminal end cap that serves for right-hand end enclosing of the control assembly. This enclosure is needed to prevent the cell from shortcut circuits.

The selection of the EL 5101 required little dimensioning beforehand, meaning that it was needed to check whether this module was able to acquire the whole data from the linear encoder. The maximum frequency from the encoder F_{sensor_max} that is delivered to the IO modules can be calculated as:

$$F_{sensor\_max} = 4 * 1.2 * \frac{V_{X\,max}}{i_{le}} \cong 1 [MHz] , \qquad (4.1)$$

where

- $V_{X\,max} = V_{Y\,max} = 210 \; mm/s$ – Maximum linear velocity along *X* and *Y* axes,
- $i_{le} = 1 [\mu m]$ – Measuring resolution of linear encoder along *X/Y* axis,
- The coefficient 1.2 is referring to 20% safety margin, and
- 4 – Multiplication factor denoting 2 channels (A and B), 2 edges per channel.

According to [90], the limit frequency of the EL5101 module is four million increments per second, i.e. $F_{IO} = 4 \, [MHz]$, which is by far larger than F_{sensor_max}, or empirically expressed as:

$$F_{IO\_min} \ll F_{IO}. \qquad (4.2)$$

Thus it can be inferred that the full data acquisition from the encoders is expected to be realized without any doubts for losing pulses.

The base module control unit consists of EtherCAT coupler EK1100 [92] and EL 2004 [93], a four slot output module. The former one is used for EtherCAT communication with the control sub-module and the later one for control of the LED illumination straps (Section 4.4) in the base module itself. An end-cap EL9011 is also positioned at the end of the control unit array, Figure 4-7.
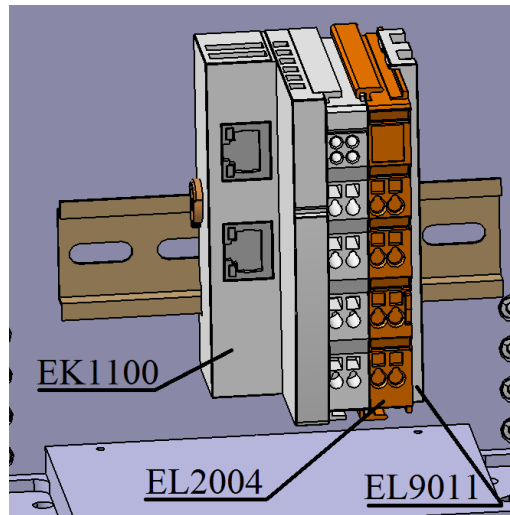
Figure 4-7 CAD of the IO modules in the base module.

4.3.2. Control software implementation

At first, the motor amplifiers were configured with EPOS Studio, which is drive axis configuration SW from supplier Maxon. The PID loop for current and velocity control of the motors was configured automatically by the software, thus the proportional, integral and derivative coefficients were automatically set and then stored into the drives and a configuration document. After configuring the motor drivers, an Ethernet com-

munication between a PC and the main controller was established and the configuration data of the motor was loaded in the controller through the TwinCAT software platform. This PC-based software platform together with the selected PLC/NC control hardware offers the possibility to perform numerical control of the axes of the robot.

TwinCAT combines software NC and software PLC and it enables a PC to process the operating programs at the same time. The communication between the two packages is a pure software to software channel with minimum delay times. [94]

4.4. Machine vision realization

Machine vision is de facto standard for part localization and part's features identification in desktop size manipulators. For the purpose of implementing vision system, a camera with appropriate optics should be selected. The selection procedure used during the development of this vision sub-module was arranged in the following way:

1. Introduce communication protocol as selection criterion that will constrain and ease the camera selection process.
2. Select at least three types of cameras.
3. Define the field-of-view (FOV).
4. Calculate lens focal length for each camera.
5. Select the camera and the optics based on price as prime decision factor and overall dimensional size as second decision factor.

In step 1, USB 3.0 was selected as desired communication interface. USB 3.0 enables fast communication up to 350 *MB/s* and also provides realization of both the communication and the power supply inside one single cable, which eases the cabling within the control and vision module (next section). Another reason for choosing the USB 3.0 communication interface is supported by the fact that Microfactory RG wants to experiment and verify the speed and reliability of it in the applications demanding higher image resolution and/or higher frame rates, in which DOHMAN might find potential usage. After closely examining the few well-known camera producers the final list with available options looks as follows (step 2):

2.1 Ximea MQ013CG-E2, datasheet available at: [95]
2.2 IDS UI-3240CP-M-GL, datasheet available at: [96]
2.3 Point Grey Flea3 FL3-U3-13Y3M-C, datasheet available at: [97]
2.4 Edmund Optics CMOS Machine Vision EO-1312M, datasheet available at: [98]
2.5 Basler Ace acA1300-30um, datasheet available at: [99]

The desired FOV (step 3) should have height (H_{FOV}) of approximately 50 *mm* and its width (W_{FOV}) depends on the aspect ratio of the camera detector; usually such sensor ratios are 5/4 or 4/3, based from the above list with camera options. Hence:

$$W_{FOV} = \frac{5}{4} * H_{FOV} = 62.5 \, mm \ or \ W_{FOV} = \frac{4}{3} * H_{FOV} = 67.08 \, mm. \qquad (4.3)$$

Once the desired FOV is defined, the focal length (f) of the optical lenses should be calculated (step 4). Such calculation can be obtained from the ratio given below.

$$\frac{f}{h_{sen}} = \frac{d_0}{H_{FOV}} \; , \tag{4.4}$$

where

- f – Focal length of the optical lenses,
- $d_0 = 265 \; mm$ – Distance from the FOV to the lenses, and
- h_{sen} – Height of camera detector.

The ratio dependency is illustrated on the Figure 4-8.
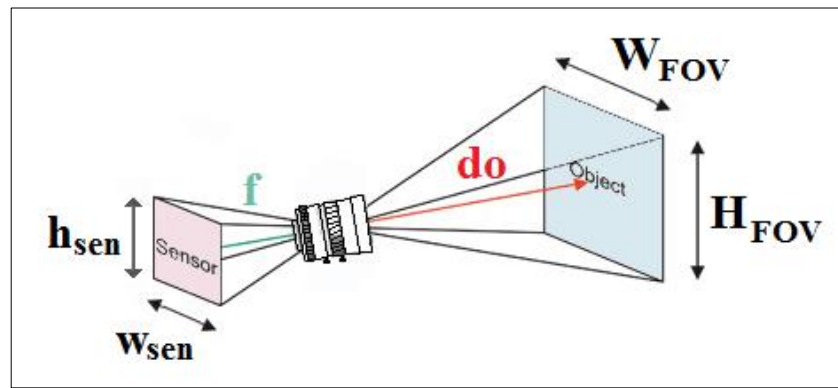
**Figure 4-8 Rough illustration of FOV and focal length (remodeled from:
http://www.parameter.fi/selectors/lens.aspx)**

Thus we obtain:

$$f = \frac{d_0}{H_{FOV}} \; h_{sen} \tag{4.5}$$

Since h_{sen} is a parameter that depends on the camera type, it is expected that the focal length will vary. The lenses that are planned to be implemented are lenses with fixed focal length. In fact, it is very seldom that calculated focal length is same as the available focal lengths given from the producers of the optical lenses. Therefore it is usual practice to choose a focal length that is closer to the calculated one. Table 8-4 in the Appendix 9 contains all the calculations for the focal lengths for each type of camera.

Continuing with step 5 requires calculating the price of each combination of camera and optics, and choosing the cheapest one. However this step is not necessary because the camera Ximea MQ013CG-E2 is by far the cheapest camera compared to the other cameras, hence it remains just to be combined with proper optical lenses. In addition to the low-cost price, Ximea cameras feature interfaces with software automation platforms such as LabVIEW and MATLAB, which enables easier integration from control point of view.

The lenses with 25 *mm* and 35 *mm* focal length provide ~72 x 58 mm^2 and ~51 x 41 mm^2 FOVs. Lenses with 25 *mm* focal length were selected because they take less spatial volume, usually have lower cost and the fact that such lenses (Spacecom JHF 25MK) are already available in the TUT Department of Mechanical Engineering and Industrial Systems facilities. A FOV closed to the desired one, i.e. 62.5 x 50 mm^2, can be achieved by lowering the camera. The possibility for realization such displacement is illustrated on Figure 4-9. Lenses (2) are attached to the camera (1) by the standard C-mount interface. The camera is rigidly attached to the moving support (3) which can move in vertical *Z* direction. When the desired position is achieved the support (3) is fixed to the support (4) by aid of M3 screws and nuts. The smallest and the largest FOVs that can be achieved by setting the camera to its end positions along the support (3) are ~68 mm x 54 *mm* (for $d_0 = 249\ mm$) and ~76 mm x 61 *mm* (for $d_0 = 281\ mm$), respectively.
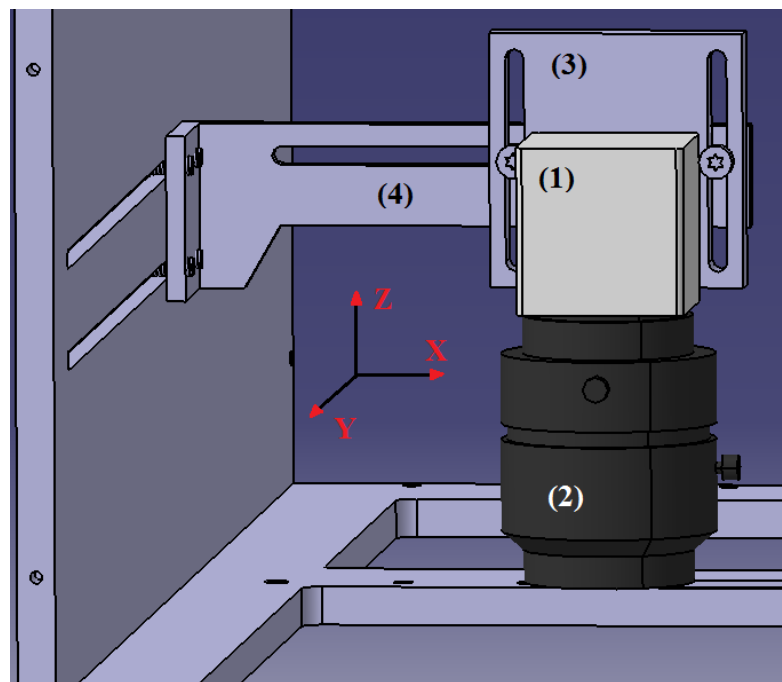
Figure 4-9 CAD illustration of the camera and optics adjustment

In addition to the vertical adjustment, the camera and lenses can be adjusted in the other two remaining directions. By sliding the support (4) along the open holes on the left plate, the camera can be positioned in *Y* direction, and by sliding the support (3) along the long hole of the support (4) it can be positioned in *X* direction within the workspace of the robot.

Illumination

The illumination is very critical aspect in machine vision systems and thus a more detailed examination of this issue is highly suggested. Usually, a good understanding of illumination types and techniques, geometry, filtering, and color are required in order to design a consistent, robust and efficient lighting. [100]

Several concerns such as *broad applicability*, *position* and *efficiency* are introduced in order to constrain the lighting selection. The broad applicability refers to more general

and uniform illumination of the workspace, thus extending the possibility to use the same lights in several applications. The position of the lights refers to the location where the lights are placed. Theoretically, they can be positioned in all of the three modules. However, the lights positioning is practically limited in the process module and control and vision module since the movements of the DOHMAN will seriously disturb the illuminated scene. In addition, the space issue and reduced moving flexibility of all vision components are other aspects that bound lights installation in these modules. Therefore the possibility of installing the lights in the base module should be examined. The efficiency refers to provision of sufficient illumination at low power consumption.

Having all the above in mind, several illumination types such as LED, halogen and florescent lights arranged differently were examined. The reference [101] suggests twelve basic geometry arrangements that lead to selection of the final illumination layout. Directional front illumination was selected as the best suiting lighting technique in which two LED stripes are attached to the top plate of the base module, see Figure 4-10. The LED stripes [102] are connected to the control unit of the base module through the 15 pin db connector (visible on Figure 4-10 a). One control output (0.5A) is dedicated for switching the both stripes (current consumption of one stripe is 0.12A) that are arranged in parallel circuit, and if necessary two additional stripes can be added to the same output. Thus one control output is able to control four LED stripes in parallel circuit. The parallel arrangement of the stripes is needed because of the system modularity, meaning that LED stripes can be easily added or removed.
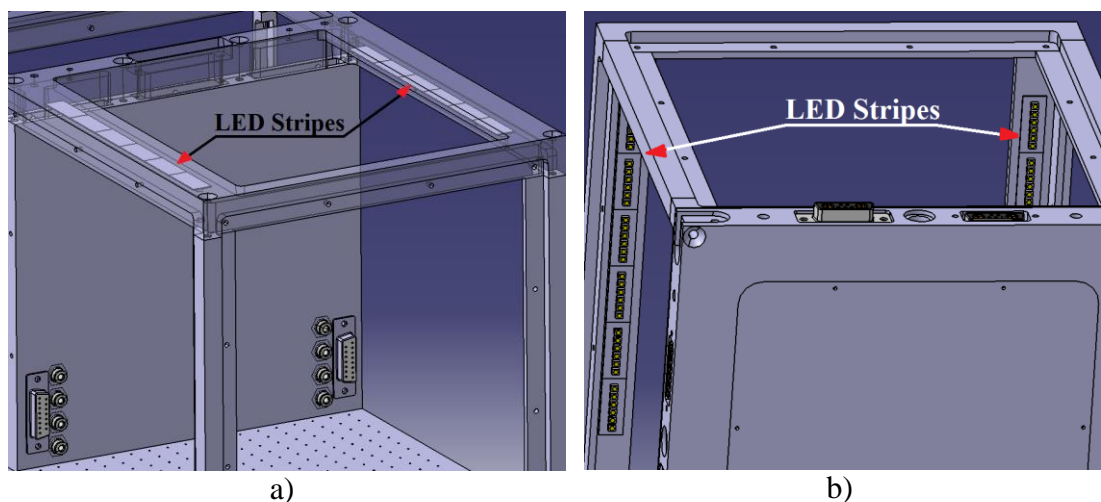
Figure 4-10 CAD illustration of LED stripes positioning into the base module. Transparent view of the top plate (a); view from the bottom of the base module (b)

Although the illustrated illumination approach satisfies the constraining concerns, it should be noted that for more specific applications (e.g. those for which only backlight is possibile) other kind of lights can be added and connected to the control unit of the base module.

4.5. Control and vision module

The control and vision components are integrated into one module called **control and vision module (CVM)** which is designed to be attached on top of the process module. The figure below shows the CAD illustration of the CVM. The control stack is attached to DIN rail and mounted onto the right CVM plate of the module (red shape). Heat reduction is done by two fan blowers (1) attached to the back plate of the module. User interaction with the control sub-module is realized through lighting push buttons (2).

The integration of the machine vision design that consists of Ximea 1.2 MP color camera, Spacecom JHF25MK optical lenses together with the camera mount supports into the CVM module is highlighted by the yellow shape.
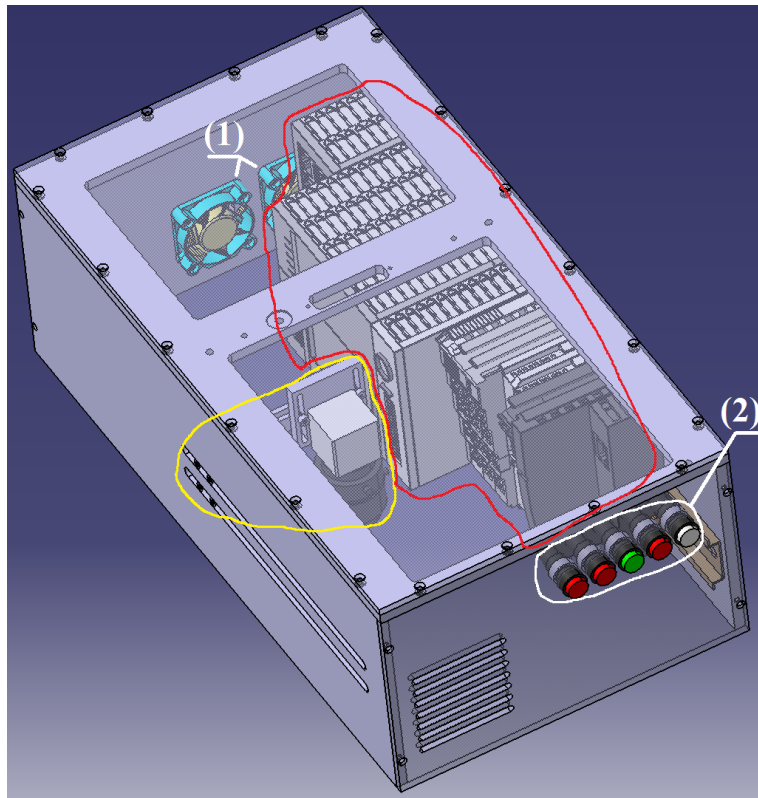
Figure 4-11 CAD illustration of the control and vision module (CVM)

5. PHYSICAL IMPLEMENTATION

Figure 5-1 illustrates the prototyped modules and their integration into a single complete and functional unit, i.e. TUT μF cell. The CAD design of the cell was previously illustrated and explained in Chapter 3.1. Images of each module along with more information about their interfacing are provided in Appendix 10 and 11 respectively. Appendix 12, in addition, provides the enumeration and color coding of wire connections.

Figure 5-1 Physical prototype of the TUT μF cell consisting from base module, process module (DOHMAN) and control and vision module

The aim of this chapter is to show the physical building of the DOHMAN, and control and vision module, the manufacturing of the composing parts (5.1), the encountered problems and solutions (5.2) and the experimental validation (5.3).

5.1. Manufacturing

As it can be seen from Appendices 1 and 2, the parts in both modules were manufactured from aluminum, steel, plastics (3D printing), sheet metal and Plexiglas.

5.1.1. Manufacturing of metal parts

Parts such as enclosing plates, couplings, BSS plates, bushing, motor holders, and π-like profiles were manufactured by aluminum and their manufacturing was outsourced to a subcontracting company. Almost all of these parts underwent an anodization surface treatment. The anodization was done for improving the strength of the parts as well as for protection from scratches. The anodized coating, on the other hand, influences the threads and cause hardship during screw insertions. Many parts required thread re-tapping.

Few parts such as axes and idle pulleys were manufactured from steel. The steel axes were machined by lathe, and the silver hardened dowel pins were grinded in order to decrease their diameters. The idle pulleys were manufactured from two lathe machined stainless steel parts and they were later fused by laser welding.

5.1.2. Manufacturing of sheet metal parts

Some custom designed washings and enclosing of the DOHMAN control unit were manufactured from sheet metal. A laser-cutting machine with Lasag KLS 246 ND:YAG [103] laser was used for manufacturing these parts. The machining was done by laser cutting with nitrogen gas and laser cutting alone. The former technique featured manufacturing of smoother edges.

5.1.3. Manufacturing of Plexiglas parts

The only Plexiglas parts are the enclosing plates that can provide transparency for visual purposes. These parts were manufactured on CO_2 laser-cutting machine.

5.1.4. Additive Manufacturing (3D printing) of parts

Figure 5-2 shows some of 3D printed parts that are installed in DOHMAN robot.
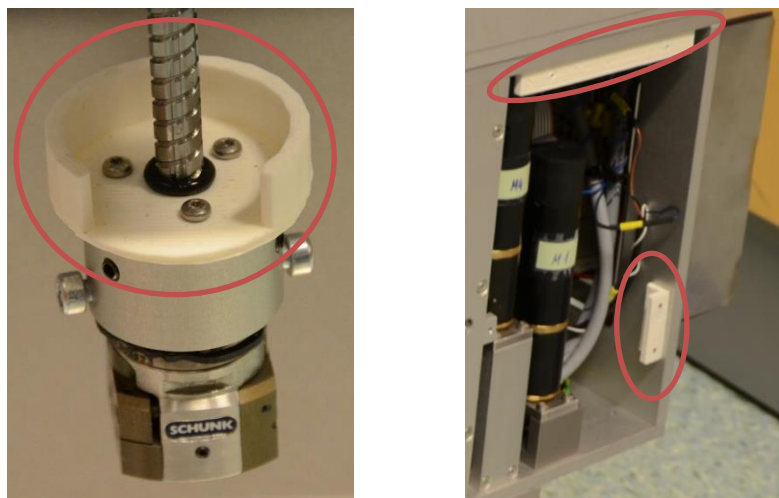
Figure 5-2 3D printed parts in DOHMAN

The image on the left illustrates the curved part for *Z&W* homing, and the image on the right the L-like profiles used for mounting the Plexiglas' plates. All of the 3D printed parts do not undertake any loading and that is the main reason why they were manufactured in this way. For 3D printing on these parts an Ultimaker 3D printer was utilized.

5.2. Encountered problems and their solutions

During the whole integration phase of DOHMAN and CV module many problems were encountered. Their explanation and solving approach is described in this section.

5.2.1. Problems with suppliers

The first problem that was encountered with the suppliers was while ordering the BSS mechanism. In fact, there are two companies in the world, i.e. THK and KSS, both from Japan, which could manufacture the component in small dimensions as they could fit within the microfactory concept. The second company was able to provide the BSS mechanism with smallest dimensions and thus their product was selected as best offer. Despite the long delivery time of 18 weeks, other drawbacks during the whole purchase were the infrequent e-mails and insufficient information in them. Additional drawback was the company's dysfunctional supply chain in Europe (European's representative did not communicate with us) so they needed to found another partner in order to reorganize their European supplies. Overall, the whole procedure of ordering the component until its arrival lasted slightly longer than 6 months.

Second similar problem was due to ordering of the GT2 belts from the company "B&B manufacturing" from United States. The initial delivery time was 6 weeks at the time during the belts were ordered. After few weeks I was informed that few belts were out of stock and additional 6 weeks are needed, to which I agreed. Before the actual dispatching, an additional delay was caused because billing system of the company does not memorize the orders older than one month. Overall, the time from the day of order until the day of receiving the belts approximately took 4 months. However, after the arrival of the belts, it was realized that two belt sizes were miscalculated and new order was placed to a Japanese company that has well established companies in Europe so the delivery time was shorter than two weeks.

Luckily the mentioned supply issues occurred in parallel; however they created unpleasant experience.

5.2.2. Assembly and integrations issues

Breaking tapping tools into the plates

While assembling the BSS mechanism to its parts, one M 2.5 tapping tool broke into one hole of the supporting plates. Same situation occurred while tapping a M2 hole in the left CVM plate. The breakage occurred as a result of the anodized surfaces in the holes of the aluminum plates. That was noticed while tapping other anodized holes. The

left over from the tapping tool was not able to be taken out and it was left inside, however the tightening remained unspoiled because of having four tightening holes in both situations.

Locking liquid into the gearhead

Figure 5-3 shows how each driving pulley is attached to the driving gear (encoder + motor + gearbox). The pulley is drilled and tapped with M2 thread and set screws are used for fixing it to the output shaft of the driving gear. However, during driving of the motors this connection was loosen and such behavior was noticed at one of the driving gear assembly. Therefore it was decided to reinforce the linking with Loctite 290 [104] locking liquid at each driving gear assembly. This adhesive liquid has very low viscosity and capillary action. It fills the small gaps between the mating surfaces and because of its time-dependent decrease in viscosity it solidifies.
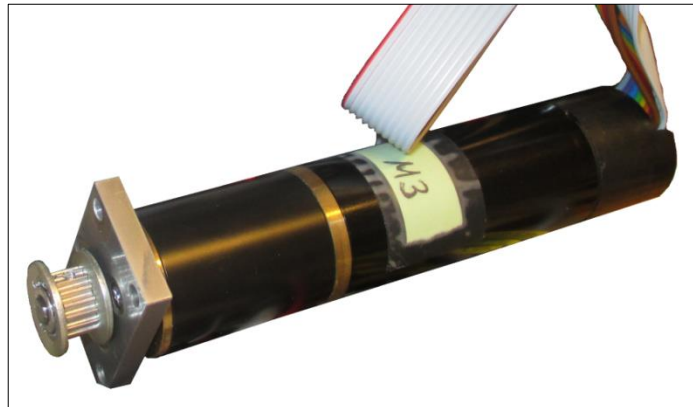
Figure 5-3 Pulley attachment to driving gear assembly

During such locking reinforcement at one of the driving gears, certain amount of the locking liquid entered into the bearings of the gearhead and completely jammed the driving gear assembly. This issue was solved by driving the motor over a long time (two times for 20 minutes) so that the increased friction burned the locking liquid.

Wrong selection of amplifiers for the motors

Although four 100W motors were selected, the motor drivers were able to amplify the motor power until 50W. However, the selected driving gears featured torque for about 40% greater than the calculated one, equation (3.30). Therefore, it is evident that the desired acceleration and payload are still achievable but under slightly lower safety factor.

FPCB-to-cable interface unit design and implementation

The encoder output of the miniscales is a flexible printed circuit board (FPCB) illustrated on Figure 5-4.
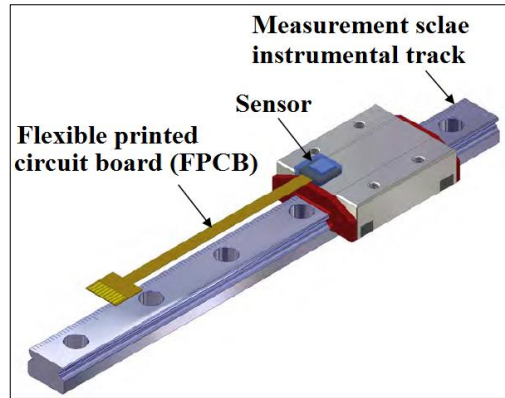
Figure 5-4 Miniscale illustration (Remodeled from [105])

In fact the FPCB is meant for static connection and it should not be exposed to any movement. Therefore an interface unit that will allow cable movement was supposed to be designed and installed. Such FPCB-to-cable interface units were custom developed for each miniscale and installed accordingly onto the BSS sub-assembly (Figure 5-5).
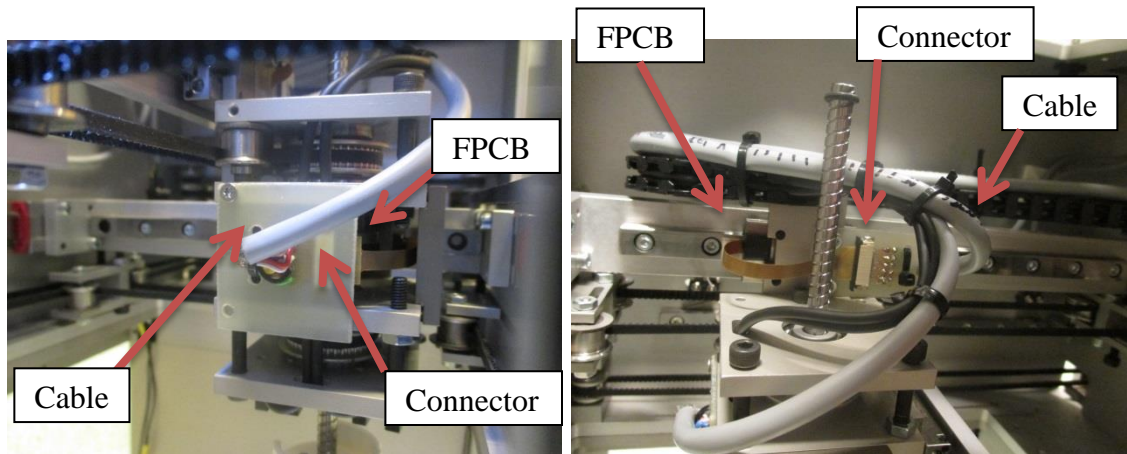
Figure 5-5 FPCB-2-cable interface units at the lower H (left); and upper H (right)

Changes within the belt tensioner mechanism

Figure 5-6 illustrates the implementation of the belt tensioner. Unlike on Figure 3-11, the belt arrangment was arranged in trapez-like structure. Therefore the middle pulley
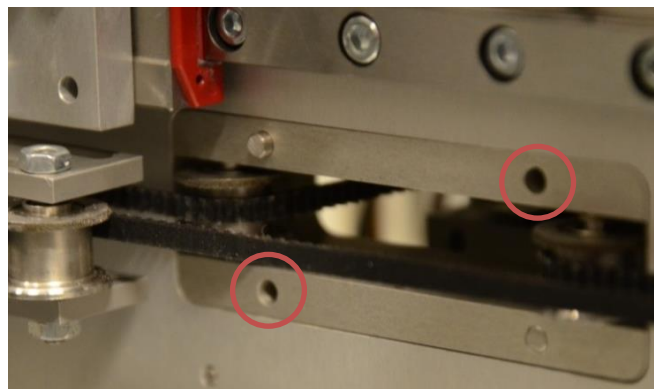
Figure 5-6 Changes caused by the implementation of the belt tensioner.

was not installed. Additional change in the belt tensioner was the avoidance of using all four guides, so two were dismissed (red circles) due to the high friciton and hardship in the movement while tensioning the belt.

The left side image on the Figure 5-7 illustrates the cabling in the actuation and control part of DOHMAN. In order to prevent any cables and/or wires to interfere with the belt within the belt tensioner mechanism, a cover was 3D printed (white part) and attached accordingly as shown on the image on the right.
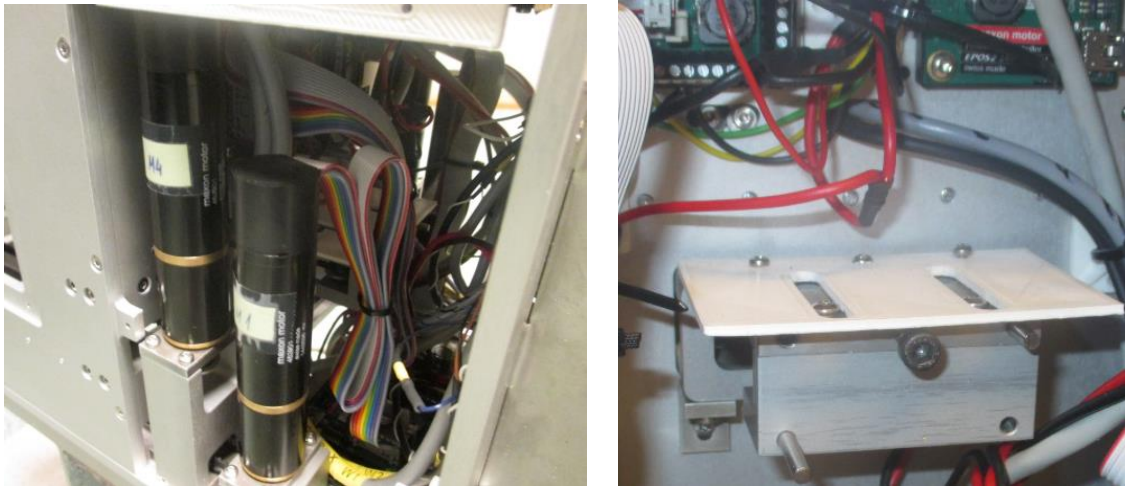
Figure 5-7 Cabling in the actuation and control part within DOHAM (left); 3D printed cover for preventing cables and wires to interfere with the belt within the belt tensioner mechanism (right).

Incorrect holes positioning of the top and bottom plate of the control and vision module

During one iterative redesign of the side plates of the control and vision module, the alignment of the holes of these plates with the holes of the top and bottom plate was not updated. This problem is illustrated with red rectangular marking on Figure 5-8, and it is solved by drilling new holes onto the side CVM plates.
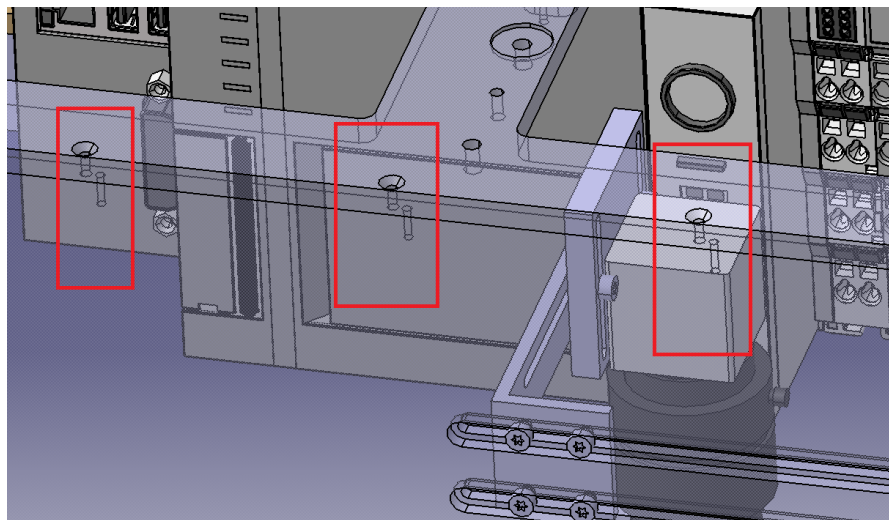
Figure 5-8 Holes misalignment between left CVM plate and top CVM plate. Transparent view of the plates for illustration purposes.

Remanufacturing of middle PM plate and top PM plate

Figure 5-9 (left) shows the CAD model of the middle PM plate in a form in which it was initially manufactured by the manufacturing subcontractor. However, during the installation of the cables it was noticed that the openings on the top should be deeper along with a need of making new opening in the center. The remanufacturing of the middle plate was realized by manual milling and thus the center opening (yellow rectangle) was formed as well as widening of the existing ones (red ellipses). The CAD model of the remanufactured middle PM plate is given on the Figure 5-9 (right).
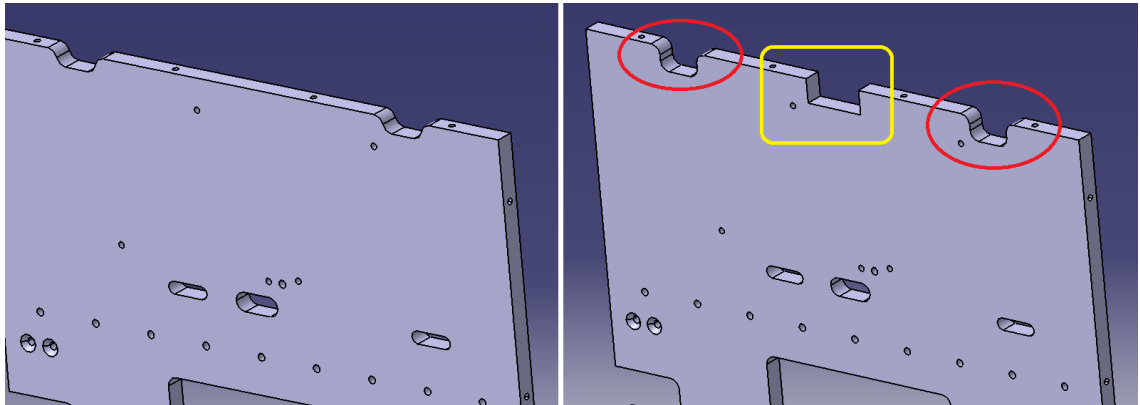
Figure 5-9 Remanufacturing of the middle plate for making new opening and widening of the existing ones

Other issue was making opening on the top PM plate for the fan blowers. This was solved also by manual re-milling of the plate.

Wrong positioning of Y–neg limit switches

Figure 5-10 show incorrect positioning of the Y–neg limit switch. This design drawback causes the BSS sub-assembly to collide with the central pulley holders (yellow circle) before the slider reaches the switch (blue ellipse). However the collision prevention is done by assigning software limits in the control program.
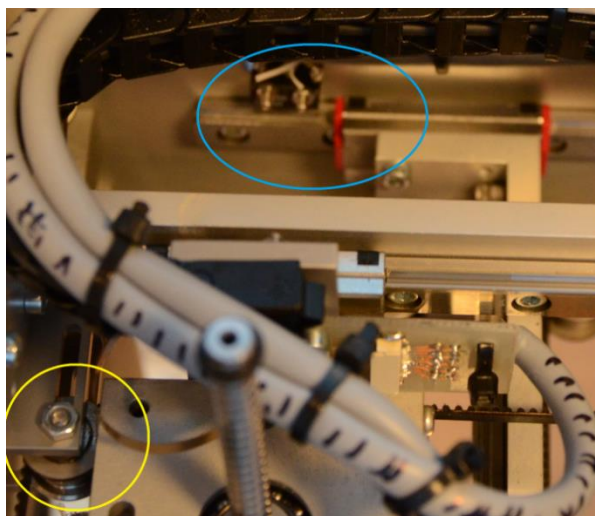
Figure 5-10 Incorrect positioning of Y-neg limit switches

5.2.3. Unbalanced displacements

Unbalanced rotation refers to uneven distribution of mass around an axis. One encountered problem as such was encountered in the screw nut. The unbalancing phenomenon was noticed due to tightening the M4 screws that are linking the two horizontal plates (a1 and a2 on Figure 5-11).

Eliminating or significantly reducing the unbalance (leaving very small presence of unbalanced rotation), was achieved by placing M4 nuts prior to the threaded holes on the second plate (red circles). The nuts helped in parallel alignment of the plates a1 and a2. However, additional screw insertions into these plates was corrupting the balanced rotation of the screw nut, thus only few screws were completely tightened.
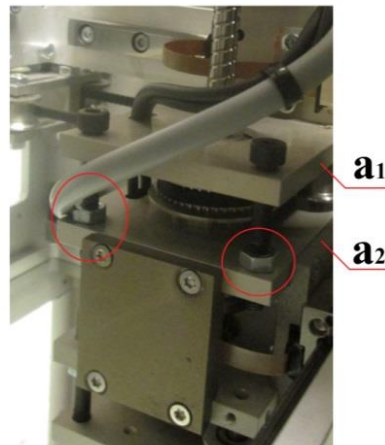
Figure 5-11 Implemented BSS

Another encountered issue was the inconsistent linear displacement (jamming and or jerking) of the bridges of the *H*-structures when were driven by constant force. There were paths along which the bridge could slide normally, but also paths where it was jamming. This issue was solved by tightening only the end screws (red circles on Figure 5-12) of the linear guideway rails and slightly untightening the rest of them (white circles). This is usual practice in machines with linear displacements. Some engineers prefer to put fillings such as ultrathin plates, between the rails and enclosing walls and then tight the loosen screws. However, it was not necessary in this case.
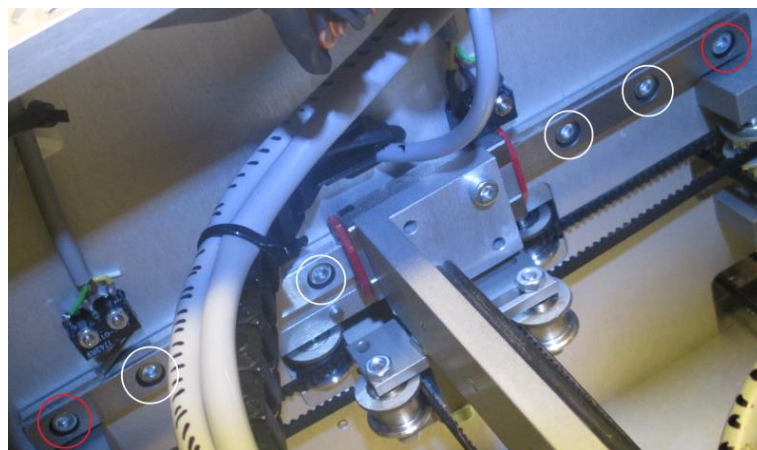
Figure 5-12 Tightening of guideways

5.3. Experimental Validation

After the implementation of DOHMAN, its kinematic model along with the controls needed to be tested and validated. At first, several different kinematic models with diverse assumptions of the mechanical system were derived and their validation onto the real model was inevitable step towards obtaining a final and correct kinematic transformation.

By manual movement of the belts (simulating motor rotation) as well as hand movement of the TCP in all of the four DOFs, the initial kinematic validation was performed, and thus one single kinematic model was obtained. This heuristically validated kinematic model as such was integrated into an existing TwinCAT PLC based control script in order to verify its correctness. The PLC control script was previously developed for control purposes of the *H*-SCARA manipulator (mentioned in Section 2.2) and changes were made in order to adopt for manipulating the DOHMAN robot.

By individual displacement of each axis through the HMI interface within the TwinCAT platform, the initial automatic driving was performed and thus the final kinematic transformation was verified as correct. After confirmation of the kinematic model, the experimental validation procedure continued with setting the homing procedure and failure recovery after facing the boundary conditions (limit switches and software limits).

DOHMAN was shown in front of the fellow students enrolled at the Machine Automation Master of Science program at TUT. The show-case was consisting of individual displacement along each axis, linear interpolation in XY plane and emulation of assembly operation. The robot in this show case was operated in low speeds, thus the dynamic errors such as vibration and drag were not visible. The G-code used for the show case is given in Appendix 13.

6. RESULTS, DISCUSSION AND CONCLUSIONS

6.1. Results

Designing, modeling and implementing the desired double *H'*-gantry manipulator into the framework of the TUT microfactory concept is successfully achieved and thus elaborated in this thesis. The resulting robot structure features theoretical maximum linear velocities ~210 *mm/s* along *X* and *Y* and ~100 *mm/s* along *Z* and ~17 s^{-1} around *W*. The maximum accelerations are ~20 *mm/s^2* for all Cartesian axes and ~570 *rev/s^2* for *W*. This robot operates in a cube-like workspace with theoretically defined dimensions of ~40 x 115 x 50 *mm^3* and its size is 200 x 450 x 270 *mm^3*. The resolution along *X* and *Y* axes is 3.1 *μm*, along *Z* axis is 4.6 *μm*, and 0.3^o for the *W* axis. The payload of the robot is 0.15 kg.

DOHMAN advantages are the distributed actuation, homogeneous workspace and innovative homing strategy for the *Z* and *W* axes. The distributed actuation enables reduced masses in the moving mechanical structure as well as reduced cabling within overall mechanical system. The consistency in the workspace enables easier control of the, as a direct consequence from lack of regions to avoid while moving the TCP. The innovative *Z* and *W* homing enable efficient use of space for mounting sensors, avoiding huge loss in the overall *Z*-axis movement, and no cabling issues. On the other hand, the robot is characterized with complex geometry seen through the counterintuitive kinematic model. The presence of the BSS mechanism and the linear guideways make this robot not to be utilized in cleanrooms because of the lubricated surfaces. The cleanroom compatibility is also impeded by the belts which accumulate dirt and dust.

6.2. Discussion

Featuring four DOF, DOHMAN and the *H*-SCARA manipulator are the most dexterous robots implemented in TUT microfactory concept. DOHMAN features higher accelerations, payload and plug and play configuration compared to its counterpart. However, the *H*-SCARA has much greater workspace rather than DOHMAN, and it is able to go in the neighboring attached modules in side-wise direction. In addition, the *H*-SCARA is three times faster along *X* and *Y* axes and two times along *Z* axis.

In comparison to the other *H*-gantry robot already implemented in TUT microfactory, i.e. the Cartesian *H*-gantry robot, DOHMAN features higher accelerations, payload

and dexterity. On the other hand, the Cartesian *H*-gantry is characterized with greater velocities and resolution along all three *X*, *Y* and *Z* axes, as well as greater workspace.

Different kind of approaches would have been taken if the design and implementation procedure could start all over again. Therefore if one will give an attempt to reproduce this work or build something on top of this, several recommendations should be considered.

At first, 10 to 20 *mm* longer lead screw could be a better choice because the overall workspace can be significantly increased. Second, more compact design of the BSS subassembly should be made because the current design is prone to vibrations; lacks rigidity and tightening of screws into the plates affect the balance of the screw nut. Third, it should be considered that laser welding of washers to the pulleys leaves some slag at the bottom of the teeth, thus gluing should be favored over the laser welding as fusing method. To continue, off-the-shelf components should be purchased only from European suppliers in order to reduce the overall project duration. Moreover, motor amplifiers with operating range from 5 to 10 Amperes should be selected. Last but not least, designing and implementing more dexterous robot that will feature 5 or 6 DOF will be much greater challenge to accomplish.

6.3. Future work

The future work in advancing DOHMAN can be categorized in three aspects, i.e. integration, modeling and control. From the aspect of integration the following things are suggested:

- measuring of the real performance of the robot and then compare with the theoretically defined one in Section 0,
- selection, mounting design and implementation of an object sensor,
- repositioning of the dysfunctional limit switches,
- pneumatic supply to the BSS mechanism and design of gripping fingers,
- making new openings on the left PM plate for easing the maintenance and increasing the visibility, and
- design and implementation of position feedback of *Z* and *W* axes.

From the modeling point of view, one can advance the robot by making dynamic modeling of each *H'*-gantry at first, then dynamic modeling of the BSS mechanism and at the end overall modeling of the robot. There is potential to use the dynamic model for controlling purposes. Speaking in terms of control, one can also try to develop and implement dedicated electronics and thus significantly reduce the footprint of the control and vision module or do reintegration of the modules.

6.4. Conclusions

The goal of this Master of Science thesis was to design, model and implement double *H'*-gantry manipulator that fits into the TUT microfactory concept, and thus is successfully accomplished. The resulting physical prototype shown throughout the figures in this document is property of Microfactory RG and is a tangible proof of the done work. In fact, the developed prototype is a result of the many iterative computer-aided-design cycles. Additional module for control and vision purposes of the robot was also designed and implemented. For building the robot prototype and its supporting module, a selection of proper off-the-shelf components along with custom designed parts and assemblies were done as well. The design decisions and the implementation phase are being elaborated in the previous chapters and in the appendix of this document. During the design phase a new innovative homing strategy for linear *Z* and angular *W* axes was suggested and later implemented. Efficient use of space for mounting sensors, avoiding huge loss in the overall *Z*-axis movement, and no cabling issues are results from the innovative *Z* and *W* homing. The robot modeling was tested and verified on the prototype itself. Additionally, a show-case was designed and implemented for external validation and demonstration purposes. The show-case was consisting of individual displacement along each axis, linear interpolation in XY plane and emulation of assembly operation.

DOHMAN features four DOF and its theoretical maximum linear velocities are ~210 *mm/s* along *X* and *Y*, ~100 *mm/s* along *Z* and ~17 s^{-1} along *W*. The robot has a foot print of 200 x 300 x 270 mm^3 and homogeneous workspace of ~40 x 115 x 50 mm^3. The maximum accelerations are ~20 mm/s^2 for all Cartesian axes and ~570 rev/s^2 for *W*. The resolution along the first two axes is 3.1 *μm*, along the third axis is 4.6 *μm*, and 0.3^{o} for the remaining forth axis. This robot features payload of 0.15 kg.

Concrete application of the robot is not defined yet although is out of scope of this thesis. However it can be used for pick and place operations of small part such as medical implants, pipettes, small mechanical components in assembling watches, and etc.

7. REFERENCES

[1] Ehmann, K. F., DeVor, R. E., & Shiv, K. G. (2002). . "Micro/meso-scale mechanical manufacturing-opportunities and challenges. *Proc JSME/ASME Int Conf Mater Process. Vol. 1*, 6-13.

[2] Tuokko, R., Heikkilä, R., Järvenpää, E., Nurmi, A., Prusi, T., Siltala, N., et al. (2012). *Micro and Desktop Factory Roadmap.* Tampere: Tampere University of Technology.

[3] Okazaki, Y., Mishima, N., & Ashida, K. (2004). Microfactory—Concept, History, and Developments. *Journal of Manufacturing Science and Engineering*, 837-844.

[4] Tanaka, M. (2001). *Development of desktop machining microfactory.* Riken Review 34.

[5] Honegger, A. E., Langstaff, G. Q., Phillip, A. G., & Vanravenswaay, T. D. (2006). Development of an automated microfactory: part 1– Microfactory architecture and sub-systems development. *Transactions of NAMRI/SME*, 333-340.

[6] Honegger, A. E., Langstaf, G. Q., Phillip, A. G., Vanravenswaay, T. D., & Kapoor, S. G. (2006). Development of an automated microfactory: part 2– Experimentation and Analysis. *Transactions of NAMRI/SME*, 341-349.

[7] Park, J. K., Lee, N. K., Lee, D. W., & Song, J. Y. (2007). Development of Microfactory Systems for the Next Generation-3rd Year Report. . *3th International Workshop on Microfactory Technology*, (pp. 5-12).

[8] Gaugel, T., & Dobler, H. (2001). Advanced modular micro-production system (AMMS). (pp. 278-285). Newton, USA: Proc. SPIE 4568, Microrobotics and Microassembly III.

[9] Verettas, I., Codourey, A., & Clavel, R. (2005). Pocket Factory: Concept of Miniaturized Modular Cleanrooms. *1st Topical Meeting of Desktop MEMS and Nanofactories (TMMF2005).* Tsukuba, Japan.

[10] Ashida, K., Nakano, S., Park, J., & Akedo, J. (2010). On-Demand MEMS Device Production System by Module-Based Microfactory. *International Journal of Automation Technology 4, no. 2*, 110-116.

[11] Kobel, P., & Clavel, R. (2010). "Circular concept of a miniaturized assembly line with an integrated clean room. *7th International Workshop of Micro-factories*, (pp. 25-29). Daejeon, Korea.

[12] Heikkilä, R., Huttunen, A., Vuola, A., & Tuokko, R. (2008). A Microfactory Concept for Laser-Assisted Manufacturing of Personalized Implants. *International Workshop on Microfactories IWMF*, (pp. 77-80). Evanstonm Illinois.

[13] Ehmann, K. F., Bourell, D., Culpepper, M., Hodgson, T. J., Kurfess, T. R., Madou, M., et al. (2005). *International assessment of research and development in micromanufacturing.* World Technology Evaluation Center (WTEC), Inc. Baltimore MD.

[14] Medical Murray. (n.d.). *Nanomolding*. Retrieved 08 21, 2013, from Medical Murray Development and Manufacturing: http://www.medicalmurray.com/Development/Nanomolding.aspx

[15] Järvenpää, E., Heikkilä, R., & Tuokko, R. (2010). Microfactory concept for highly flexible volume assembly of watch mechanisms. *Workshop on Microfactories*, (p. 6). Daejeon, Korea.

[16] JOT Automation. (n.d.). *JOT IDeA.* Retrieved 08 22, 2013, from Micro Assembly: http://www.jotautomation.com/media/datasheets/j505-74_datasheet_2_0_6_print.pdf

[17] Heikkilä, R., Järvenpää, E., & Tuokko, R. (2010). Avances in the TUT Microfactory Concept Development. *International Journal of Automation Technology*, Vol4, No.2, pp118-126.

[18] Zhenishbek, Z., Golubovic, E., & Sabanovic, A. (2013). Galvanometric optical laser beam steering system for microfactory application. *Industrial Electronics Society, IECON 2013-39th Annual Conference of the IEEE* (pp. 4138-4143). Vienna: IEEE.

[19] Nurmi, A. T. (2012). *Business models and applications for micro and desktop production systems.* Tampere, Finland: Master of Science thesis at Tampere University of Technology, (page 86-th).

[20] Cenev, Z., Prusi, T., & Tuokko, R. (2014). Image stitching based measurement of medical screws. *International Precision Assembley Seminar* (p. 10). Chamonix, France: Springer.

[21] Biohit. (n.d.). *Biohit Roboline.* Retrieved 08 22, 2013, from Liquid Handeling: http://www.biohit.com/resource/files/media/brochures/liquid-handling/all/roboline-brochure-490100en-screen.pdf

[22] Dynex Technologies. (n.d.). *Our Products*. Retrieved 08 22, 2013, from Dynex Technologies: http://www.dynextechnologies.com/index.php

[23] RepRap. (n.d.). *RepRap*. Retrieved 08 22, 2013, from RepRap.org: http://reprap.org/wiki/Main_Page

[24] Fab@Home. (n.d.). *Main Page*. Retrieved 08 22, 2013, from fabathome.org: http://www.fabathome.org/wiki/index.php?title=Main_Page

[25] MakerBot. (n.d.). *Makrebot Store*. Retrieved 08 22, 2013, from Makrebot Replicator 2: http://store.makerbot.com/

[26] Formlabs. (n.d.). Retrieved 08 2013, from Formlabs - High Resolution Desktop 3D Printer: http://formlabs.com/

[27] Xie, N., Onal, C., Regnier, S., & Sitti, M. (2012). *Atomic Force Microscopy Based Nanorobotics.* Heidelberg: Springer. (page 7-th).

[28] Murthy, R., Stephanou, H. E., & Popa, D. O. (April 2013). AFAM: An Articulated Four Axes Microrobot for Nanoscale Applications. *IEEE Transactions on Automation Science and Engineering*, 276-284.

[29] Král, M., & Clavel, R. (2011). Pollution monitoring sensor for a Micro-Factory. *IEEE International Symposium on Assembly and Manufacturing (ISAM)* (pp. 1-4). Tampere: IEEE.

[30] Kobel, P., & Clavel, R. (2011). Miniaturization Challenges and Their Impact on the Micro-factory Concept and Manipulators. *Journal of the Japan Society for Precision Engineering*, 263-268.

[31] Hofmann, A., Hummel, B., & Bär, M. (2011). microFLEX - A New Concept to Address the Needs for Adaptable Meso and Micro Assembly Lines. *IEEE International Symposium on Assembly and Manufacturing (ISAM)* (pp. 1-5). Tampere: IEEE.

[32] Hofmann, A., Bretthauer, G., Siltala, N., & Tuokko, R. (2011). Evolvable Micro Production Systems: Specific Needs and Differences to Macro. *IEEE International Symposium on Assembly and Manufacturing (ISAM)* (p. 6). Tampere: IEEE.

[33] Giovanni, L., Borboni, A., Gabrielli, A., Fassi, I., Ruggeri, S., Fontana, G., et al. (2013). Design of a miniaturized work-cell for micro-manipulation. *21 Congresso AA. NAZ. Meccanica Teorica ed Applicata*, (p. 10). Tornio.

[34] Fontana, G., Ruggeri, S., Fassi, I., & Legnani, G. (2014). A mini work-cell for handling and assembling microcomponents. *Assembly Automation 34 (1)*, 27-33.

[35] Burisch, A., Wrege, J., Raatz, A., Hesselbach, J., & Degen, R. (2007). PARVUS–miniaturised robot for improved flexibility in micro production. *Assembly Automation 27.1* , 65-73.

[36] Burisch, A., Raatz, A., & Hesselbach, J. (2010). Challenges of precision assembly with a miniaturized robot. *Precision Assembly Technologies and Systems (IPAS)* (pp. 227-234). Springer Berlin Heidelberg.

[37] Mistubishi Electric. (n.d.). *Mistubishi Electric Melfa RP series robots*. Retrieved 08 16, 2013, from MELFA Roboter – RP-Serie: http://www.mitsubishi-automation.de/products/robots_RP.html

[38] THK. (n.d.). *Presision Ball Screw/Spline.* Retrieved 08 22, 2013, from Product Catalog: https://tech.thk.com/upload/catalog_claim/pdf/327E_BNS_NS.pdf

[39] Perroud, S., Codourey, A., & Mussa, Y. (2006). PocketDelta: a Miniature Robot for Micro-assembly. *5th International Workshop on Microfactories*, (pp. 193-200). Besancon, France.

[40] *Asyril*. (n.d.). Retrieved 08 16, 2013, from Asyril: http://www.asyril.ch/en/products/delta-robots.html

[41] Fanuc Robotics UK. (n.d.). *Industrial Robots*. Retrieved 08 16, 2013, from M-1 Series: http://www.fanucrobotics.co.uk/en/Products/A_Industrial-Robots/M-1iA

[42] Sysmelec Robot and Automation. (n.d.). *Equipment Machines*. Retrieved 08 16, 2013, from High precision robots: http://www.sysmelec.ch/page.asp?id=131&parentid=129

[43] Klocke Nanotechnik. (n.d.). *XYZ manipulator*. Retrieved 08 16, 2013, from Orthogonal Movement With High Resolution: http://www.nanomotor.de/n_xyz_manipulator.htm

[44] KEC. (n.d.). *RakuRobo*. Retrieved 06 2013, from rakurobo: http://www.rakurobo.jp/RB23_catalog.pdf

[45] Heikkilä, R. (2011). *AC-Desk TUT research plan.* Tampere: TUT

[46] Zoltán, F. (2010). "Mathematical Modelling of 4 DOF Gantry Type Parallel Manipulator". Munich: Robotics (ISR), 41st International Symposium on and 6th German Conference on Robotics (ROBOTIK) (pp1-6). VDE.

[47] Dassault Systèmes. (2002). *3D CAD design software CATIA*. Retrieved 12 2013, from http://www.3ds.com/products-services/catia/

[48] MathWorks. (1994). *MATLAB - The Lenguage of Technical Computing*. Retrieved 12 2013, from http://www.mathworks.com/products/matlab/index.html?s_tid=gn_loc_drop

[49] Beckhoff Automation GmbH. (n.d.). *TwinCAT - PLC and Motion Control on the PC*. Retrieved 12 2013, from http://www.beckhoff.com/english.asp?twincat/default.htm

[50] National Instruments. (n.d.). *LabVIEW System Design Software*. Retrieved 12 2103, from NI LabVIEW - Improving the Productivity of Engineers and Scientists: http://sine.ni.com/np/app/main/p/docid/nav-104/lang/fi/

[51] Heikkilä, R., Karjalainen, I., Uusitalo, J., Vuola, A., & Reijo, T. (2007). The concept and first application for the TUT Microfactory. *International Workshop on Microfactory Technology*, (pp. 57-61). Jeju-do, Korea

[52] Vuola, A., Heikkilä, R., Prusi, T., Remes, M., Rokka, P., Siltala, N., et al. (2010). Miniaturization of flexible screwing cell. *Precision Assembly Technologies and Systems* (pp. 309-316). Springer.

[53] Siltala, N., Vuola, A., Heikkila, R., & Tuokko, R. (2010). A H-Scara Mini Robot - a Dual Parallel Kinematics Mini Manipulator. *41st International Symposium on Robotics (ISR) and 6th German Conference and on Robotics (ROBOTIK)*, (pp. 1-7). Berlin.

[54] Prusi, T., Vuola, A., Siltala, N., Heikkilä, R., & Tuokko, R. (2010). "Robots for micro and desktop factories: examples and experiences. *Robotics (ISR), 2010 41st International Symposium on and 2010 6th German Conference on Robotics (ROBOTIK)* (pp. 1-7). Berlin: VDE.

[55] Siltala, N., Vuola, A., Prusi, T., Heikkilä, R., & Tuokko, R. (2012). Comparison of Five Low Cost Manipulators for Microfactories. *International Workshop on Microfactories*, (p. 8). Tampere, Finland.

[56] Multimechatronics. (n.d.). *H-bot Slides.* Retrieved 2013, from Multidisciplinary Mechatronic Innovations: http://multimechatronics.com/images/uploads/courses/h_Bot/H-Bot%20Web%20Site%20Slides%205-11-2011.pdf

[57] Weikert, S., Ratnaweera, R., Zirn, O., & Wegener, K. (2011). *Modeling and Measurment of H-bot kinematic systems.* Zurich: ETH Institute for Machine Tools and Manufacturing.

[58] Sollmann, K., Jouaneh, M. K., & Lavender, D. (April 2010). Dynamic Modeling of a Two-Axis, Parallel, H-Frame-Type XY Positioning System. *IEEE/ASME Transaction on Mechatronics*, Vol.15.

[59] THK CO., LTD. (n.d.). Retrieved 06 2013, from THK Global: http://www.thk.com/?q=eng/node/202

[60] KSS Co., Ltd. (n.d.). Retrieved 06 2013, from KSS Japan | Ball Screw & Actuators: http://www.kssballscrew.com/

[61] Donelan, P. (2007). Singularities of Robot Manipulators. *Singularity Theory*, 189-217.

[62] THK. (n.d.). *Ball Screw- General catalog. Page A-757*. Retrieved 20 22, 2013, from THK CO LTD Web Site: http://www.thk.com/sites/default/files/documents/uk_pdf/product/general/a/ee_A15.pdf

[63] Festo. (n.d.). *Motor Sizing and Selection from First Principles - Torque Calculation*. Retrieved 10 22, 2013, from Festo Support Forum: http://www.festo.com/net/SupportForum/yaf_postst65_Motor-Sizing-and-Selection-from-First-Principles---Torque-Calculation.aspx

[64] Leadshine Technology Co. Ltd. (n.d.). *"Motor Torque Calculation" page 2.* Retrieved 07 08, 2013, from http://www.leadshine.com/Pdf/Calculation.pdf

[65] Engineering Toolbox. (n.d.). *Friction and Coefficients of Friction*. Retrieved 10 23, 2013, from engineeringtoolbox: http://www.engineeringtoolbox.com/friction-coefficients-d_778.html

[66] B&B Manufacturing. (n.d.). *Product details for 1524-2P-03* . Retrieved 07 2013, from http://www.bbman.com/catalog/product/1524-2P-03

[67] Maxon Motor AG. (2012, 05). *"EC 22 Ø22 mm, brushless motor, 100 Watt".* Retrieved 07 08, 2013, from http://www.maxonmotor.com/medias/sys_master/8807042121758/13_175_EN.pdf

[68] Maxon Motor AG. (2013, 06). *Planetary Gearhead GP 22C.* Retrieved 10 23, 2013, from

http://www.maxonmotor.com/medias/sys_master/8807050706974/13_251-252_EN.pdf

[69] Maxon Motor AG. (n.d.). *DC motors and drive systems*. Retrieved 12 2013, from http://www.maxonmotor.com/maxon/view/content/index

[70] Faulhaber. (n.d.). *Miniature Drive Systems*. Retrieved 2013, from http://www.faulhaber.com/n613857/n.html

[71] Maxon Motor AG. (n.d.). *EPOS2 Positioning Control Units.* Retrieved 06 2013, from http://www.maxonmotor.com/medias/sys_master/8807077478430/13_328-329-330_EN.pdf

[72] Stock Drive Products / Sterling Instrument. (n.d.). *Drive your System with Timing Belts.* Retrieved 10 17, 2013, from sdp-si: http://www.sdp-si.com/product-announcements/Timing%20Belts%20White%20Paper.pdf

[73] MISUMI. (n.d.). *Catalog.* Retrieved 10 17, 2013, from MISUMI Corporation: http://us.misumi-ec.com/pdf/fa/PDFViewer.html?catalog=metric2010&page=1096

[74] Stock Drive Products / Sterling Instrument. (n.d.). *Positioning Accuracy.* Retrieved 10 17, 2013, from sdp-si.com: http://www.sdp-si.com/D265/HTML/D265T008.html

[75] B&B Manufacturing. (n.d.). *Neoprene Timing Belts.* Retrieved 12 2013, from Power Transmission Components and Sychronous Drive parts: http://files.catalogds.com/domains/bbman/trumotionsyncdata_final_3-8-07.pdf?__utma=1.1605946655.1387808477.1387808477.1387808477.1&__utmb=1.7.10.1387808477&__utmc=1&__utmx=-&__utmz=1.1387808477.1.1.utmcsr=google|utmccn=(organic)|utmcmd=organic|utmctr=(not%20provided)&__utmv=-&__utmk=22541755

[76] ETRA Oy. (n.d.). Retrieved 08 2013, from ETRA: http://www.etra.fi/

[77] Farnell. (n.d.). Retrieved 08 2013, from Finland Farnell | Electronic Components: http://fi.farnell.com/?CMP=KNC-GFI-FFI-GEN-PFB&mckv=sUMmUfx22|pcrid|24343400307|kword|farnell|match|e|plid|

[78] Omron Corporation. (n.d.). Retrieved 08 2013, from Omron Finland: http://omron.fi/fi/home

[79] Omron Corporation. (n.d.). *D2F Ultra Subminiature Basic Switch*. Retrieved 08 2013, from Omron Electronic Components: http://www.omron.com/ecb/products/sw/13/d2f.html

[80] Omron Corporation. (n.d.). *EE-SX911P-R 1M*. Retrieved 08 2013, from Omron Industrial Automation: http://www.ia.omron.com/product/item/eesx1963h/index.html

[81] Beckhoff Automation GmbH. (n.d.). *Homing*. Retrieved 12 2103, from http://infosys.beckhoff.com/english.php?content=../content/1033/ax5000_usermanual/html/ax5000_homing.htm&id=

[82] Beckhoff Automation GmbH. (2013). *CX2030.* Retrieved 10 13, 2013, from http://www.beckhoff.com/english.asp?highlights/cx2000/default.htm

[83] Beckhoff Automation GmbH. (2013). *CX2500-00xx - System modules for CX2000.* Retrieved 10 31, 2013, from http://www.beckhoff.com/english.asp?highlights/cx2000/default.htm

[84] Beckhoff Automation GmbH. (2013). *EL6751 - CANopen master/slave terminal*. Retrieved 10 31, 2013, from http://www.beckhoff.com/english.asp?ethercat/el6751.htm

[85] Beckhoff Automation GmbH. (2013). Retrieved 10 31, 2013, from EL1809, EL1819 - HD EtherCAT Terminals: http://www.beckhoff.com/english.asp?EtherCAT/el1809_el1819.htm

[86] Beckhoff Automation GmbH. (2013). *EL2828 - HD EtherCAT Terminal*. Retrieved 10 31, 2013, from http://www.beckhoff.com/english.asp?ethercat/el2828.htm

[87] Beckhoff Automation GmbH. (2013). *CX2100-0xxx - Power supply unit with E-bus/K-bus interface.* Retrieved 10 31, 2013, from http://www.beckhoff.com/english.asp?embedded_pc/cx2100_0004_cx2100_0904_cx2100_0915.htm

[88] Beckhoff Automation GmbH. (2013). *EK1110 - EtherCAT extension.* Retrieved 10 31, 2013, from http://www.beckhoff.com/ek1110/

[89] Beckhoff Automation GmbH. (2013). *EK1818 - EtherCAT Coupler with integrated digital inputs/outputs.* Retrieved 10 31, 2013, from http://www.beckhoff.com/english.asp?ethercat/ek1818.htm

[90] Beckhoff Automation GmbH. (2013). *EL5101 - Incremental encoder interface*. Retrieved 10 31, 2013, from http://www.beckhoff.com/english.asp?ethercat/el5101.htm

[91] Beckhoff Automation GmbH. (2013). *EL9011 - End cap*. Retrieved 10 31, 2013, from http://www.beckhoff.com/english.asp?ethercat/el9011.htm

[92] Beckhoff Automation GmbH. (2013). *EK1100 - EtherCAT Coupler*. Retrieved 10 31, 2013, from http://www.beckhoff.com/english.asp?ethercat/ek1100.htm

[93] Beckhoff Automation GmbH. (2013). *EL2004 - 4-channel digital output terminal*. Retrieved 10 31, 2013, from http://www.beckhoff.com/english.asp?ethercat/el2004.htm

[94] Beckhoff Automation GmbH. (n.d.). *TwinCAT - PLC and Motion Control on the PC*. Retrieved 12 2013, from http://www.beckhoff.com/english.asp?twincat/default.htm

[95] Ximea. (n.d.). *Ultra-compact USB3 Vision industrial camera*. Retrieved 10 21, 2013, from usb3 industrial cameras: http://www.ximea.com/en/products-news/usb3-industrial-camera

[96] IDS. (n.d.). *UI-3240CP*. Retrieved 10 21, 2013, from Cameras: http://en.ids-imaging.com/store/produkte/kameras/usb-3-0-kameras/ueye-cp/ui-3240cp.html

[97] Edmund Optics. (n.d.). *usb cameras*. Retrieved 10 21, 2013, from Flea3 FL3-U3-13Y3M-C 1/2" Monochrome USB 3.0 Camera:

http://www.edmundoptics.com/imaging/cameras/usb-cameras/point-grey-flea3-usb-3-0-cameras/86767

[98] Edmund Optics. (n.d.). *EO-1312M Monochrome USB 3.0 Camera*. Retrieved 10 21, 2013, from usb cameras: http://www.edmundoptics.com/imaging/cameras/usb-cameras/eo-usb-3-0-cmos-machine-vision-cameras/86754

[99] Edmund Optics. (n.d.). *Basler Ace acA1300-30um Monochrome USB 3.0 Camera*. Retrieved 10 21, 2013, from usb cameras: http://www.edmundoptics.com/imaging/cameras/usb-cameras/basler-ace-usb-3-0-cameras/88321

[100] Martin, D. (2007). *A Practical Guide to Machine Vision Lighting* . Retrieved 11 05, 2013, from Machine Vision Lightening: http://www.graftek.com/pdf/Marketing/MachineVisionLighting.pd

[101] Machine Vision Association of SME. (n.d.). *Lighting and Optics Reference Guide.* Retrieved 11 05, 2013, from MVA Lighting and Optics Poster: http://www.engatechvision.com/images/mvaposter.pdf

[102] ledxon GmbH. (2013). *Functional LED Components.* Retrieved 11 05, 2013, from Catalog: Module Performance: http://www.ledxon.de/pdf/katalog/ledxon_Hauptkatalog_Module_2012.pdf (page 38)

[103] Rofin. (2012, 08 01). *LASAG KLS 246.* Retrieved 01 2014, from Rofin - Lasers for Industry: http://www.rofin.com/fileadmin/user_upload/intern/marking/videos/data_sheet_KLS_engl.pdf

[104] Henkel Technologies. (n.d.). *Loctite 290 Technical Data Sheet.* Retrieved 12 2013, from http://www.loctite.sg/sea/content_data/93808_290EN.pdf

[105] Schneerberger. (n.d.). *Miniscale Mounting Instructions.* Retrieved 09 2013, from http://www.schneeberger.com/index.php?id=341&no_cache=1&tx_drblob_pi1%5BdownloadUid%5D=535

[106] Schneerberger. (n.d.). *MINIRAIL.* Retrieved 09 30, 2013, from Profiled miniature guideway: http://www.schneeberger.com/index.php?id=338&no_cache=1&tx_drblob_pi1[downloadUid]=71

[107] Schneerberger. (n.d.). *MINISCALE.* Retrieved 09 30, 2013, from Miniature guideway with integrated measuring system - "all in one": http://www.schneeberger.com/index.php?id=338&no_cache=1&tx_drblob_pi1[downloadUid]=75

[108] KSS. (n.d.). *Miniature Ball Screw with Ball Spline.* Retrieved 07 25, 2013, from http://www.kssballscrew.com/us/pdf/catalog/BSSP_Ditail.pdf

[109] SMB bearings. (n.d.). *Metric Thin Section Bearings*. Retrieved 06 2013, from http://www.smbbearings.com/smbnew/thin-section-metric-bearings.html

[110] SCHUNK GmbH. (n.d.). *Small multi-taskers for micro assembly*. Retrieved 05 2013, from SCHUNK GmbH & Co. KG Spann- und Greiftechnik: http://www.schunk.com/schunk/schunk_websites/news/news_detail.html?article_id =18486&country=INT&lngCode=EN&lngCode2=EN

8.   APPENDICES

This chapter provides additional materials valuable for deeper understanding of certain designs, concepts, sizing and dimensioning as well as issues concerned with the implementation of the developed microfactory modules. First two appendices contain complete bill of materials for the process and control and vision module. The third and the fourth appendix elaborate the core mechanisms in greater detail. The appendices from 5 to 9 contain information important in driving gear dimensioning, belts sizing, DOHMAN enclosing design, IO dimensioning and camera selection sheet, respectively. The tenth, eleventh and twelfth appendix refer to the implementation phase related issues and the Appendix 13 contains the G-code used in the experimental validation. Last but not least is the data CD appendix, i.e. Appendix 14, which summarizes the content of the enclosing CD that comes with this document.

APPENDIX 1: BILL OF MATERIALS OF DOHMAN MODULE

The bill of materials used for development of the DOHMAN as process module in the TUT µF cell is clustered and represented in the table below.

Table 8-1 Bill of materials for DOHMAN module

Category/Assembley/Parts	Unit Price	Quantity	Total Price €
Custom designed aluminum parts, unless otherwise noted:			
Parts for driving gear sub-assembly			
Motor holder – type low	*	2	
Motor holder – type H-like	*	2	
Bottom support for H-like motor holder	*	2	
Motor to holder interface	*	4	
Parts for belt tensioner sub-assembly			
Belt tensioner static pulley holder	*	1	
L-like belt tensioner to middle plate interface	*	2	
Belt tensioner moving part 1	*	1	
Belt tensioner moving part 2	*	1	
Machined axis rod for GT2 pulley ($\varphi = 4$ *mm*; length = 17 *mm*)	*	3	
Parts for DOHMAN (Process Module) enclosure			
Back PM plate	*	1	
Middle PM plate	*	1	
Front PM plate	*	1	
Left PM plate	*	1	
Right PM plate	*	1	
Top PM plate	*	1	
Bottom PM plate	*	1	
Parts for H-gantry structures			
Pi-like profile – short	*	1	
Pi-like profile – long	*	1	
Pulley holder for central idle pulleys	*	4	
Machined axis rod for central idle pulley ($\varphi = 3$ mm; length = 23 mm)	*	3	
Parts for BSS sub-assembly			
BSS support plate 1	*	1	
BSS support plate 2	*	1	
BSS support plate 3	*	1	
BSS support plate 4	*	1	
Interface plate: BSS to Lower H	*	1	
Interface plate: BSS to Upper H	*	1	
Interface plate: BSS SuppPlate2 to SuppPlate3	*	1	
Interface plate: BSS Lead Screw to Schunk gripping interface	*	1	

Screw Nut Bushing	*	1	
Machined axis rod for idle pulley (φ = 3 *mm*; length = 25 *mm*)	*	4	
Pulleys, axes, couplings, cable tubes, coolers			
Short machined axis rod for GT2 pulley (φ = 4 mm; length = 32 mm) material: steel	*	2	
Lower machined axis rod for GT2 pulley (φ = 4 mm; length = 21 mm) material: steel	*	4	
Upper machined axis rod for GT2 pulley (φ = 4 mm; length = 39 mm) material: steel	*	4	
Idle Pulleys – material: steel	10	10	100
Middle axes coupler	*	2	
Axis Coupler type 1	*	4	
Axis Coupler type 2	*	4	
Overall manufacturing costs for all parts marked with (*)			5000
Custom designed Plexiglas parts:			
Parts for DOHMAN (Process Module) enclosure			
Plexiglas plate 1 (~148 *mm* x 60 *mm*, thickness = 2 *mm*)		1	0
Plexiglas plate 2 (~148 *mm* x 70 *mm*, thickness = 2 *mm*)		1	0
Plexiglas plate 3 (~180 *mm* x 100 *mm*, thickness = 2 *mm*)		1	0
Plexiglas plate 4 (~170 *mm* x 104 *mm*, thickness = 2 *mm*)		2	0
Laser-cut sheet metal parts:			
Washers (outer φ = 16 *mm*; inner φ =12 *mm*, thickens = 1 *mm*)	1	4	4
Washers (outer φ = 4 *mm*; inner φ = 3 *mm*, thickens = 1 *mm*)	1	50	50
DOHMAN control unit enclosure (thickness = 1.5 *mm*)	50	1	50
Off-the-shelf electro-mechanical parts:			
Driving gears			
Maxon EC 22 φ22 *mm*, brushless motor, 100 *W* – #386674	#	4	
Maxon Gearhead GP 22 C – #143977	#	4	
Maxon Encoder MR 512 IMP, 3K 32P ASIC – #201940	#	4	
Maxon motor amplifier EPOS2 24/2 EC16/EC22 – #380264	#	4	
Overall manufacturing costs for all parts marked with (#)			3026
Linear slides and guides			
Schneeberger Minirail MNNL-SC 9-195-G1-V1 (guideway length= 195 mm)	"	2	
Schneeberger Minirail MNNL-SC 9-175-G1-V1 (guideway length= 195 mm)	"	2	
Schneeberger Miniscale (linear guideway with integrated encoder) MNNL-SC 9-195-G1-V1 (guide length= 195 mm)	"	2	
Schneeberger Miniscale (linear guideway with integrated encoder) MNNL-SC 9-155-G1-V1 (guide length= 195 mm)	"	2	
Overall manufacturing costs for all parts marked with (")			1266
Limit Switches			

Omron EE-SX911P-R photo microsensor	16	2	32
Omron D2F-01FL ultra subminiature basic switch	4	4	16
Belts, pulleys and bearings, cable tubes, fan blowers,			
High Torque Timing GT2 pulley 16 teeth, width 4 *mm*	15.46	15	231.9
High Torque Timing GT2 pulley 40 teeth, width 4 *mm*	17.52	2	35.04
Timing GT2 belt length 100 *mm*, width 4 *mm*	2.5	1	2.5
Timing GT2 belt length 558 *mm*, width 4 *mm*	3.7	1	3.7
Timing GT2 belt length 1228 *mm*, width 4 *mm*	2.83	1	2.83
Timing GT2 belt length 1524 *mm*, width 4 *mm*	3.2	1	3.2
SMB MR63 – Miniature bearing (3 *mm* x 6 *mm* x 2 *mm*)	0.7	50	35
Igus cable tube 10 x 10 (length = ~30 *mm*)	10	1	10
Fan blowers 40 *mm* x 40 *mm* x 25 *mm*	10	2	20
Parts for Ball Screw-Spline sub-assembly			
KSS Ball Screw-Spline component	2625	1	2625
Schunk 305626 MWPG 20 – gripping interface	100	1	100
EZO 6801 – Thin section bearing (12 *mm* x 21 *mm* x 5 *mm*)	3.4	4	13.6
Control Unit IO modules			
Beckhoff EK1818	1408	1	1408
Beckhoff EL5101	2068	2	4136
Beckhoff EL9011	30.8	1	30.8
Terminal blocks (one for current supply, one for GND)	10	2	20
Custom designed 3D printed parts:			
L-like profiles – type PG2BP	5	2	10
L-like profiles – type PG2TP	5	2	10
Curved part for *Z&W* homing	5	1	5
Washers (outer φ = 6; inner φ =2, thickness = 1)	2	8	16
Belt Tensioner Cover	5	1	5
Interfacing pin holder	5	4	20
Electronic components and mechanical fasteners:			
Precision rod (φ = 3 *mm*; length = 65 *mm*)	^	4	
Socket head cap screw M4x40	^	1	
Socket head cap screw M4x30	^	6	
Precision rod (φ = 3 *mm*; length = 25 *mm*)	^	3	
Flat head torx M2.5x8	^	~90	
Socket head cap screw M2.5x10	^	~35	
Socket head cap screw M3x8 / M3x10	^	~100	
Cable 10 wire twisted pair (1 m)	^	1	
Socket D-Sub-M Mixed Power 17w2	^	1	
Plug D-Sub-M Mixed Power 17w2	^	1	
Custom designed interface module for Flexible PCB plug	^	2	
DIN rail (length = 125 *mm*)	^	1	
Traco power TSR-1 Series, 1A, 24VDC to 5VDC convertor	^	1	
Overall manufacturing costs for all parts marked with (^)			100

Sub Total			18387
TOTAL = Sub Total + 0.1*Sub Total			**20226**

Beside the bill of materials the table contains the information about the cost of each or group of parts. This is considered as valuable information if one decides to repeat the work and/or compare the hardware costs in respect to other process modules or manipulators for microfactories. The added 10% margin to the sub total costs is costs due to delivery, reordering parts as a result of redesign, remanufacturing and repair.

APPENDIX 2: BILL OF MATERIALS OF CONTROL AND VISION MODULE

In a similar way as in Appendix 1, the bill of materials used in the development of the control and vision module is listed below:

Table 8-2 Bill of materials for CVM

Category/Assembley/Parts	Unit Price	Quantity	Total Price €
Custom designed metal parts:			
Parts for control and vision module enclosure			
Back CVM plate	**	1	
Left CVM plate	**	1	
Right CVM plate	**	1	
Top CVM plate	**	1	
Parts for camera mounting and positioning			
L-like camera support	**	1	
Camera holder	**	1	
Custom designed plexiglas parts:			
Top CVM enclosing plate	**	1	
Front CVM plate	**	1	
Overall manufacturing costs for all parts marked with (**)			1000
Off-the-shelf electro-mechanical parts:			
Controller and control modules			
Beckhoff controller CX2030	1436	1	1436
Beckhoff control power supply CX2100-0004	2145	1	2145
Beckhoff digital input module EL1819	657.8	1	657.8
Beckhoff digital output module EL2828	770	1	770
Beckhoff CANopen module EL6751	3454	1	3454
Beckhoff end terminal and EtherCAT extension EK1110	583	1	583
Beckhoff USB3.0 module CX2500-0070 – not installed	146	1	146
Terminal blocks (two for current supply, two for GND)	10	4	40
Camera, fan blowers and buttons			
Ximea MQ013CG-E2 1MP, USB 3.0 camera	330	1	330
Fan blower 40 *mm* x 40 *mm* x 10 *mm*	10	2	20
Push buttons with LED indicators	10	5	50
Electronic components and mechanical fasteners:			
Socket D-Sub-M Mixed Power 17w2	&	1	
CANopen self-made cable, length= ~25 *mm*	&	1	
DIN rail (length = 350 *mm*)	&	1	
Cable 14 wire twisted pair, length= ~350 *mm*	&	1	
Traco power TSR-1 Series, 1A, 24VDC to 5VDC convertor	&	1	
Socket head cap screw M2.5x8/ M2.5x10	&	~20	

Flat head torx M2.5x8/ M2.5x10	&	~10	
Socket head cap screw M5x6	&	2	
Overall manufacturing costs for all parts marked with (&)			100
Sub Total			10691
TOTAL = Sub Total + 0.1*Sub Total			**11760**

Along with the bill of materials the table contains the information about the cost of each or group of parts. This is considered as valuable information if one decides to repeat the work and/or compare the hardware costs in respect to other control and vision modules for microfactories. Due to delivery, reordering parts because of redesign, remanufacturing and repair, a margin of 10% is added to the sub total costs.

APPENDIX 3: PARTS IN THE *H'*-GANTRY MECHANISMS EMPLOYED IN DOHMAN

As mentioned in Chapter 3.2 each *H'*-bot consists of three linear guideways, a pi-like profile, four idle pulleys (referred as central idle pulleys) and two pulley holders. The linear guideways are off-the-shelf components selected from the Schneeberger, a company for linear motion systems; all the other parts are custom made. According to the product datasheets of the linear guideways, the lateral linear guideways are denoted as minirails [106] and the linear slide (mounted on the bridge i.e. the pi-like profile) with encoder on its carriage is denoted as miniscale [107]. The length of each minirail and miniscale is 195 *mm* in the upper *H'*-bot. In the lower *H'*-bot, however, the lengths of the minirails and the miniscale are 175 *mm* and 155 *mm* respectively.

The figure bellow contains sketched 3D drawings with several dimensions of the central pulley holder (a), the idle pulley sub-assembly (b) and the bridge which is designed as π-like profile (c). The illustrated bridge on the Figure 8-1 is the one of the upper *H'*-bot and the one of the lower *H'*-bot has length of 168 *mm* and six instead of ten M3 holes.
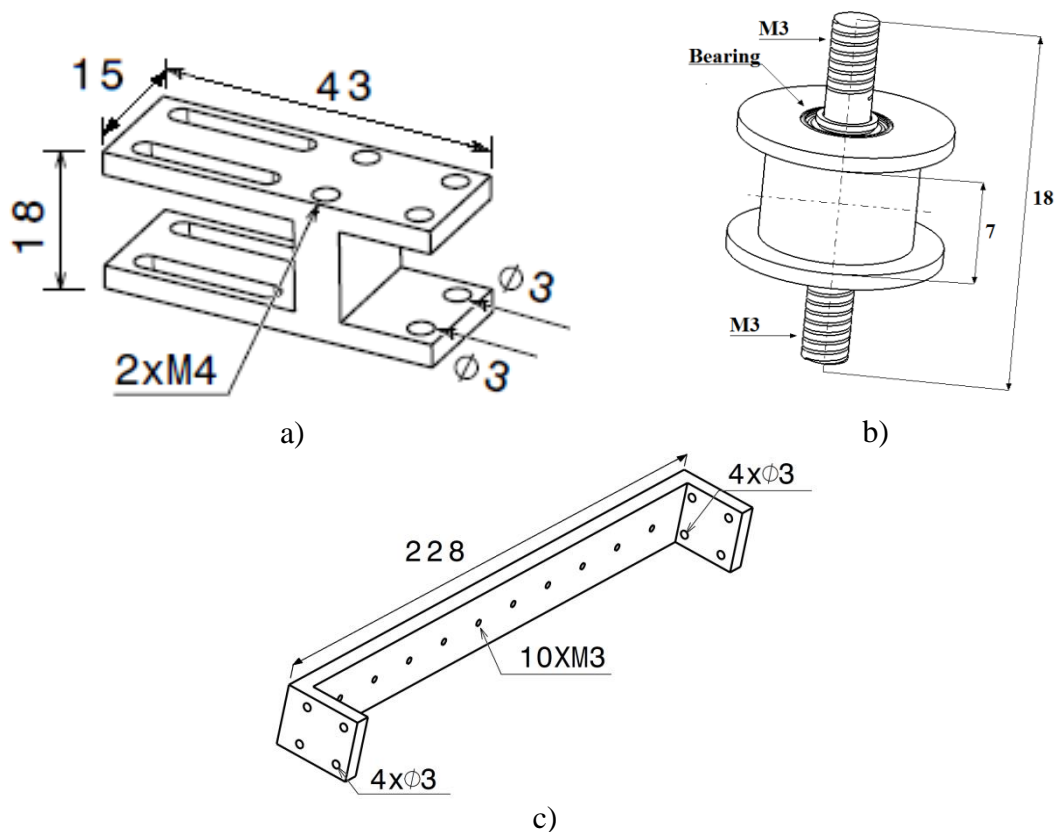
Figure 8-1 Holder for central idle pulleys (a) idle pulley (b) bridge [pi-like profile] (c); All dimensions are in millimeters

APPENDIX 4: BALL SCREW-SPLINE COMPONENT

The figure bellow contains a technical drawing with dimensional information of the selected BSS mechanism.
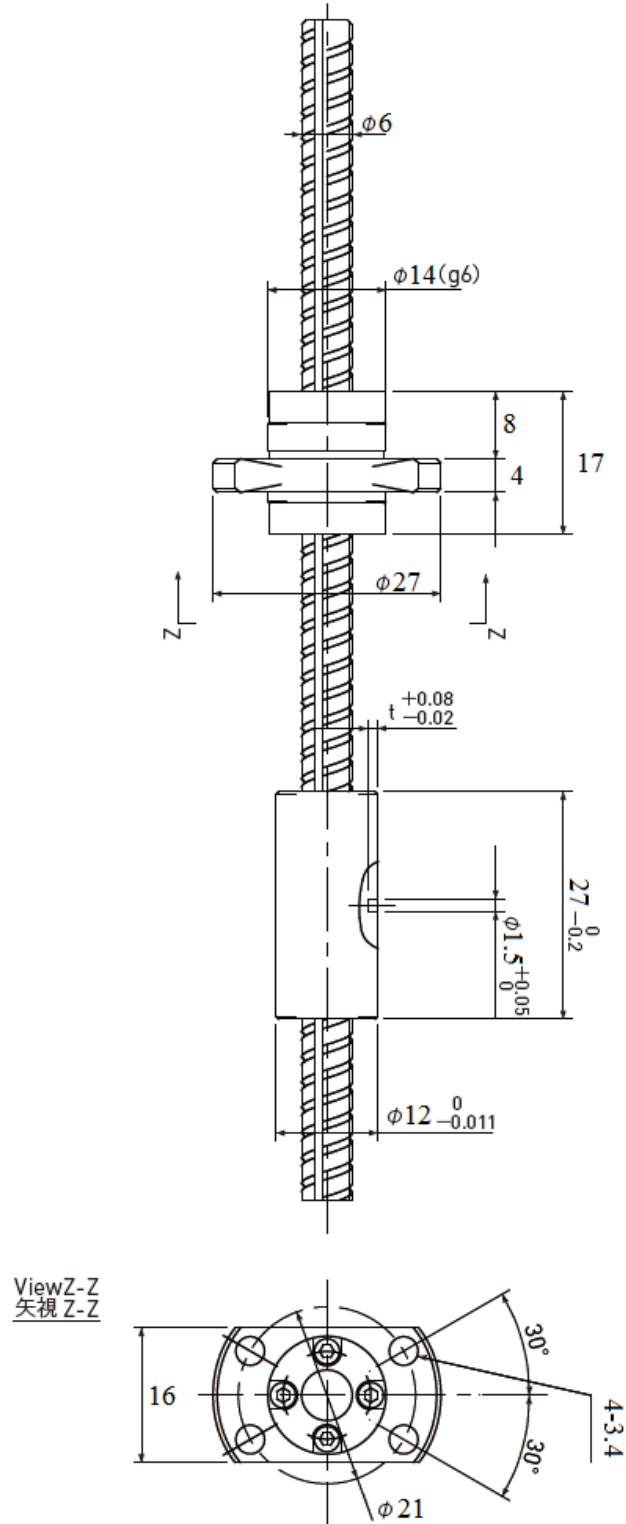
Figure 8-2 Technical drawing of the BSS component with ordered dimensions from Japanese Manufacturer KSS (Remodeled from [108])

The BSS is not functional alone itself, thus it should be integrated into a structure that will maintain the orientation of the lead screw as well as enable driving the nuts. Such integration is illustrated on Figure 8-3.
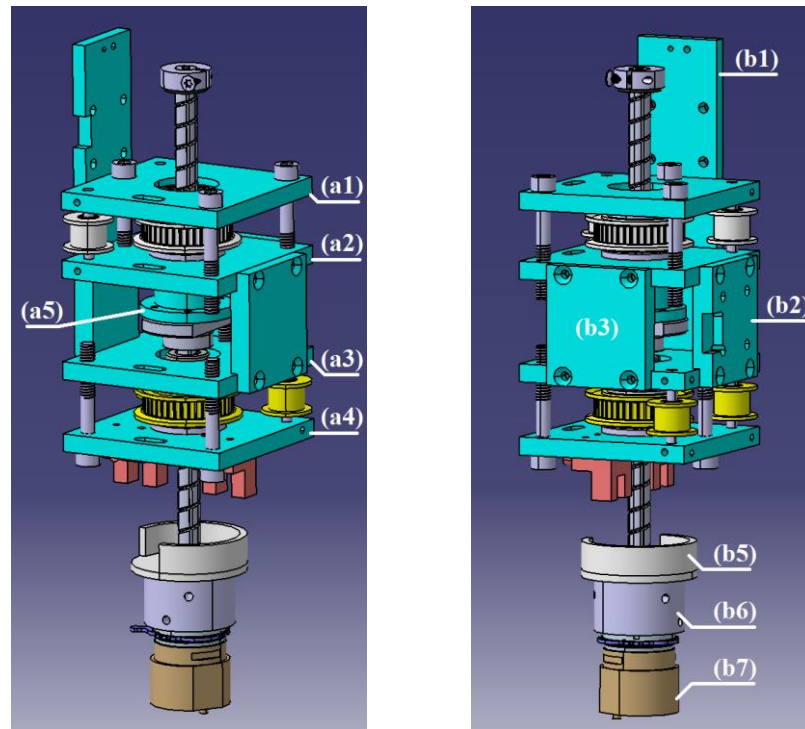
Figure 8-3 CAD model of the BSS sub-assembly from two different perspectives.

Horizontal plates (a1 to a4) and the vertical plates (b1 to b3) on the figure above form a structure that encompass the BSS that allow mounting possibilites for both nuts. Each horizontal plate is hollowed and it accomodates EZO 6801 thin-section bearing [109]. The spline nut resides directly onto the plates a3 and a4, however the screw nut fitting to plates a1 and a2 is realized through the bushing a5. The bushing in addition enables the torque from the upper big pulley (white in color) to be transferred to the screw nut. The first two as well as the later two plates are axially tightened by three M4x30 screws respectively. The vertical plates b1, b2 and b3 wedge the BSS structure. The b1 acts as interface plate to the linear slide of the upper H structure, and b2 as interface plate to the lower H structure.

A washing with tickness of 1 *mm* is positioned between each bearing and each big pulley. Redish fork-like parts on the bottom of a4 are photo microsensors that together with the 270° arc profile (b5) are used for homing of *Z* and *W* axes, described in greater detail in Chapter 3.9.

The end of the lead screw is fixed into a cavity hole of the part (b6). The (b6) enables the lead screw to have a pneumatic link with the miniature gripper interface SCHUNK MWPG 20 [110], i.e. the brown colored component (b7). This gripping interface enables gripping fingers to be attached on it in order to perform gripping/releasing operations. This component was already a property of Microfactory RG and as such did not undergo any selection process, but directly integrated into the design.

APPENDIX 5: MATLAB CODE FOR SELECTION OF DRIVING GEARS

The MATLAB code that aided the minimum required torque calculation for the driving gears is shown below.

```matlab
%%                  DOuble H-gantry MANiuplator (DOHMAN)
%%             driving gear(motor + gearhead) dimensioning
%%
%   Created by Zoran Cenev
%   07/2013
%%
clc
clear all
%%
% Definition of parameters
i_r = 81/4;             % Gearhead Reduction Ratio
eta_g = 0.7;            % Efficiency of Gearhead
g = 9.81;               % Gravitational acceleration
eta_bss = 0.9;          % BSS efficiency coefficient
i_bt = 0.9;             % Belt transmission coefficient
Ks = 2.0;               % Safety Factor (Reference Value from 1.5 to
2)
p = 0.006;              % BSS Lead Screw pitch

a_angle = 0;            % Angle of inclination
eta_lg = 0.85;          % Efficiency (0.85 - 0.95) of a linear guide

mu = 0.16 * 3;          % Steel to Steel friction for
                        % lubricated and greasy surfaces mu = 0.16
                        % factor 3 is added because the mass is moving
                        % along 3 guides
m_load = 0.15           % [kg] Mass of load
a_y = 2*g;              % [mm/s^2] Desired Linear Acceleration along Y
a_z = 2*g;              % [mm/s^2] Desired acceleration along Z axis
%%
% Motor dimensioning case 1

m_leads = 0.02;         % [kg] Mass of Lead Screw
m_mar = 0.02;           % [kg] Marginal Mass
% Overall mass that it shoud be picked upwards:
m_z = m_leads + m_mar + m_load;

%Required force to pick the load:
F_z = m_z*g + m_z*a_z;
%Required torque of the big pulley for having F_z:
T_z = F_z*p/(2*pi*eta_bss);
%Required torque of the driving small pulley for having T_z:
T_dg1 = T_z*i_bt*Ks
%%
% Motor dimensioning case 2

%Dimensions from datasheets and estimated masses from part's CAD mod-
els:
D_p = 0.010;            % [m] Small (Driving and Idle) Pulley Diameter
m_p = 0.002;            % [kg] Mass of Small (Driving and Idle) Pulley
D_bp = 0.025;           % [m] Big Pulley (Pulley on BSSP Nut) Diameter
m_bp = 0.007;           % [kg] Mass of Big (Pulley on BSSP Nut) Pulley
```

```matlab
m_b = 0.03;              % [kg] mass of belt for belt with length 1660 mm
m_bssa = 0.6662;          % mass of BSS sub-assembly
m_bss = 0.054;            % mass of BSS mechanism alone
% mass of X-gantry: m_x = 0.6240
% mass of Y-gantry: m_y = 0.6040
% For simplification purposes, we will assume that the mass of gantry
% along any direction, X or Y, is 0.6240. Thus:
m_axis = 0.6240;
% [kg] Mass of linearly displaced Load (m_ml) as sum of mass of BSS
% sub-assembly + mass of gantry along Y axis + mass of the load
m_ml = m_bssa + m_axis + m_load;
%-------------------------------------------------------
% Calculation of Inertias:
J_ml = (D_p^2 * m_ml)/4;     % [kg*m^2] Inertia of the moving mass
J_sp = (m_p * D_p^2)/8;      % [kg*m^2] Inertia of the small pulley
J_bp = (m_bp * D_bp^2)/8;    % [kg*m^2] Inertia of the big pulley
J_b = (D_p^2 * m_b)/4;       % [kg*m^2] Inertia of the belt
J_bss = (D_p^2 * m_bss)/4;   % [kg*m^2] Inertia of the BSS
J_m = 4.09 * 10^-3 * 10^-4;  % Moment of inertia of EC22,
                             % 100W brushless Maxon motor
J_gh = 0.5 * 10^-3 * 10^-4;  % Moment of inertia of a Maxon gearhead
GP22C

% Total Moment of Inertia:
J_t = J_ml + 10*J_sp + J_bp + J_b + J_bss + 2*(J_m + J_gh);
%-------------------------------------------------------
% Angular Acceleration [/s^-2]
alfa = a_y/(D_p/2);
% Acceleration Torque [N]
T_a = J_t * alfa;
%-------------------------------------------------------
% T_l Load torque:
T_l = (m_ml*g*D_p*(sin(a_angle) + mu*cos(a_angle))) / (2*eta_lg);
%-------------------------------------------------------
% Cumulative Torque:
T_c = T_a + T_l;
%-------------------------------------------------------
% Torque on Gearhead Shaft
T_dg2 = T_c * Ks;
%-------------------------------------------------------
% Required Motor Torque:
% T_m2 = T_g/(i_r * eta_g);
%%
T_dg = max(T_dg1,T_dg2)
```

APPENDIX 6: BELT SIZING DISTANCES

The values of the distances in the lower H belt structure are as follows:

- $x_{lh1} = 139\ [mm]$;
- $x_{lh2} = 165\ [mm]$;
- $x_{lh3} = 135\ [mm]$;
- $x_{lh4} = 19\ [mm]$;
- $x_{lh5} = 40\ [mm]$;
- $x_{lh6} = 35\ [mm]$;
- $x_{lh7} = 43\ [mm]$;

The values of the distances in the upper H belt structure are as follows:

- $x_{uh1} = 163\ [mm]$;
- $x_{uh2} = 27.5\ [mm]$;
- $x_{uh3} = 101.5\ [mm]$;
- $x_{uh4} = 19\ [mm]$;
- $x_{uh5} = 38\ [mm]$;
- $x_{uh6} = 35\ [mm]$;
- $x_{uh7} = 28\ [mm]$;
- $x_{uh8} = 54\ [mm]$;
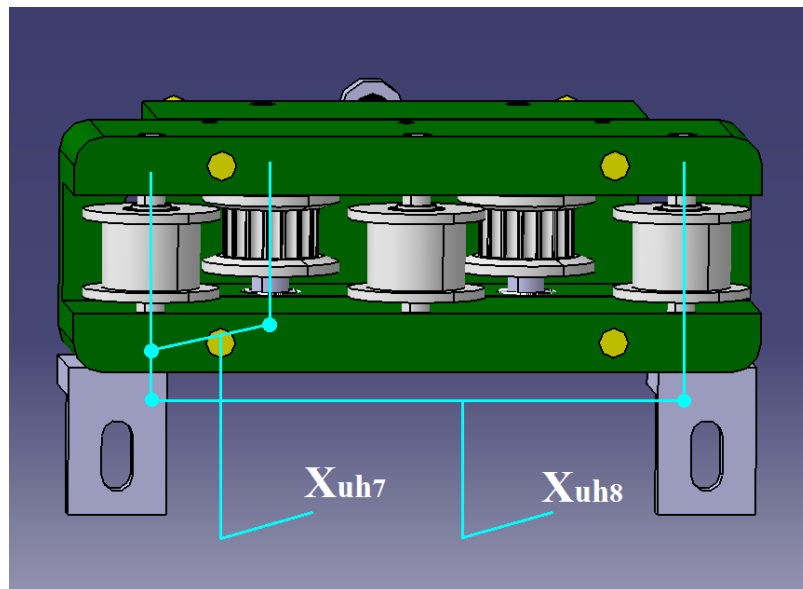
Figure 8-4 Illustration of belt tensioner dimensions X$_{uh7}$ and X $_{uh8}$ used for belt circumference estimation calculations

APPENDIX 7: ENCLOSUING OF DOHMAN MODULE

Figure 8-5 shows the enclosing of DOHMAN or the process module (PM). The front PM plate (1), right PM plate (2), left PM plate (3) and middle PM plate (4) are enclosing the space in which all mechanics of the robot are placed. The middle plate and the back PM plate (5), together with two Plexiglas plates (6) (other plate is visible on Figure 8-6) are enclosing the motors and their amplifiers.
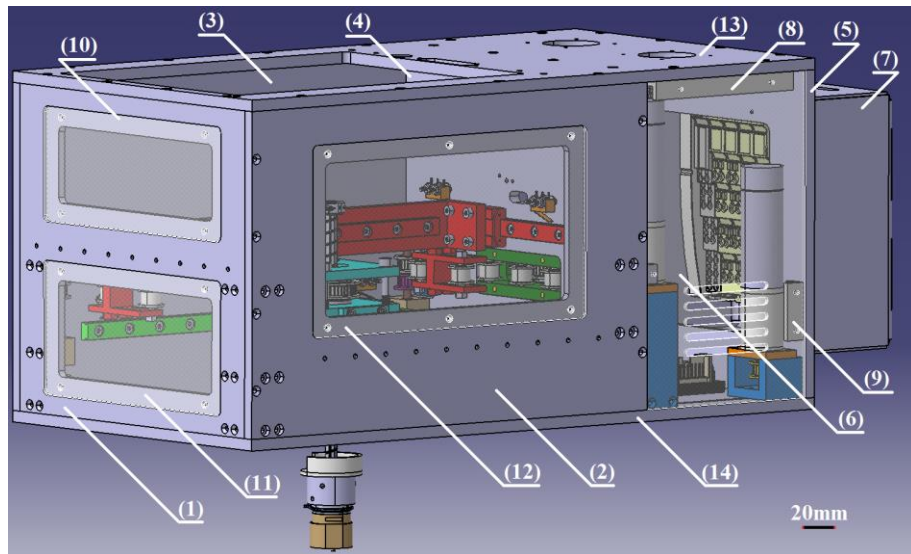
Figure 8-5 CAD of DOHMAN module with full enclosure

The control unit is placed in a rectangular cavity formed from 1.5 *mm* thick sheet metal and in the bill of materials is denoted as DOHMAN control unit enclosure (7). This control unit enclosure is attached to the back PM plate as shown on Figure 8-6.
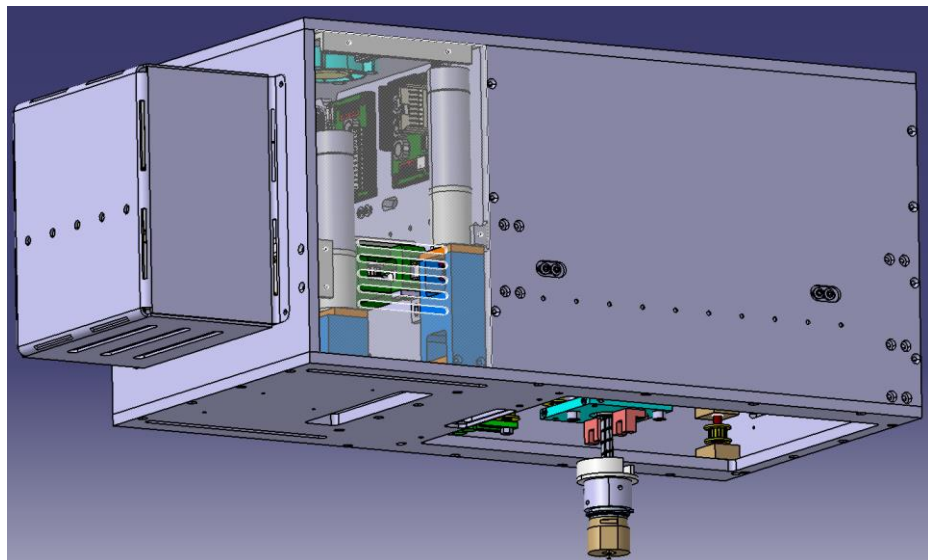
Figure 8-6 Different perspective of enclosed DOHMAN module

Overheating prevention of the motors, the amplifiers and the control unit is arranged by two fan blowers attached on the top plate (13). The fan blowers are blowing the hot air outside of the enclosed space and the new cooler air is entering in by the holes in the

Plexiglas plates and the control unit enclosure. The L-like profiles (8) and (9) are enabling the attachment of the Plexiglas plates (6).

Openings within the front and right plates are filled with the Plexiglas plates (10), (11) and (12), in Appendix 1 they are denoted as Plexiglas plates 1, 2 and 3 respectively. These openings are created to ease the assembly of the robot and also enable visual observation of the structure and working principle of the robot. The enclosing from below and above is realized by the top PM plate (13) and the bottom PM plate (14). Beside the enclosing role, they enable interfacing of the process module with the base module and control and vision module from below and above respectively.

Figure 8-6 provides different perspective of the enclosed process module.

APPENDIX 8: INPUT/OUTPUT LISTING FOR IO DIMENSIONING

Table 8-3 Input/output listing for dimensioning the IO modules

Location	Device	In-puts	Out-puts	Quan-tity	Total Inputs	Total Outputs	Operating Voltage [DCV]	Output Voltage [DCV]	Type of Output	Max. Pulse Frequency [Hz]
Complex inputs / outputs										
DOHMAN	Linear Encoder (pulses A,B,C)	1	0	2	2	0	5	5	pnp	~1 000 000
DOHMAN	Motor Driver (CANopen)	0	1	4	0	4	9 to 24	8.1 to 21.6	0.9*	1000
CVM	Camera	1	0	1	1	0	5	/	/	/
CVM	CANopen Interfce	0	0	1	0	0	/	/	/	/
Digital inputs and out-puts										
DOHMAN	Optical Fork Switch	1	0	2	2	0	5 to 24	/	pnp	5000
DOHMAN	Limit Switch	1	0	4	4	0	30	/	/	10
DOHMAN /CVM	Fan blower	0	0	4	0	0	5	/	/	/
DOHMAN	Vacuum valve	0	1	2	0	2	24		/	/
DOHMAN	Object sensor	1		1	1	0	5 to 24	/	/	/
DOHMAN	**Total**				**7**	**2**				
CVM	Buttons	1	0	5	5	0	24	/	/	/
CVM	LEDs for indicating buttons	0	1	5	0	5	24	24		
CVM	**Total**				**5**	**7**				
BM	Lights	0	1	1	0	1	24	24		
BM	**Total**				**0**	**1**				

APPENDIX 9: CAMERA SELECTION SHEET

Table 8-4 Camera selection data sheet

FOV		Distance from Object to Camera Sensor [mm]	Camera						Focal Length		Available FOV		Resulting Resolution		Price [€]
Width	Height		Sensor Width [mm]	Sensor Height [mm]	Sensor Width [pix]	Sensor Height [pix]	Pixel size [µm]	Aspect Ratio	Desired Focal Length	Available Focal Length	Width	Height	Spatial Resolution [pix/mm]	Smallest Measurable Feature [mm]	
Ximea MQ013CG-E2															~330
62.50	50.00	265.00	6.78	5.43	1280	1024	5.30	1.25	28.76	25.00	71.91	57.53	17.80	0.28	
62.50	50.00	265.00	6.78	5.43	1280	1024	5.30	1.25	28.76	35.00	51.36	41.09	24.92	0.20	
IDS UI-3240CP-M-GL															~630
62.50	50.00	265.00	6.78	5.43	1280	1024	5.30	1.25	28.76	25.00	71.91	57.53	17.80	0.28	
62.50	50.00	265.00	6.78	5.43	1280	1024	5.30	1.25	28.76	35.00	51.36	41.09	24.92	0.20	
Point Grey Flea3 FL3-U3-13Y3M-C															~500
62.50	50.00	265.00	6.14	4.92	1280	1024	4.80	1.25	26.05	25.00	65.13	52.10	19.65	0.25	
62.50	50.00	265.00	6.14	4.92	1280	1024	4.80	1.25	26.05	35.00	46.52	37.22	27.52	0.18	
Edmund Optics CMOS Machine Vision EO-1312M															~600
62.50	50.00	265.00	6.78	5.43	1280	1024	5.30	1.25	28.76	25.00	71.91	57.53	17.80	0.28	
62.50	50.00	265.00	6.78	5.43	1280	1024	5.30	1.25	28.76	35.00	51.36	41.09	24.92	0.20	
Basler Ace acA1300-30um Monochrome USB 3.0 Camera															~600
67.08	50.00	265.00	4.86	3.89	1296	966	3.75	1.34	20.61	16.00	80.49	64.40	16.10	0.31	
67.08	50.00	265.00	4.86	3.89	1296	966	3.75	1.34	20.61	25.00	51.52	41.21	25.16	0.20	

APPENDIX 10: IMAGES FROM DOHAMN AND CONTROL AND VISION MODULES

Figure 8-7 illustrates the implemented DOHMAN robot from two different perspectives.
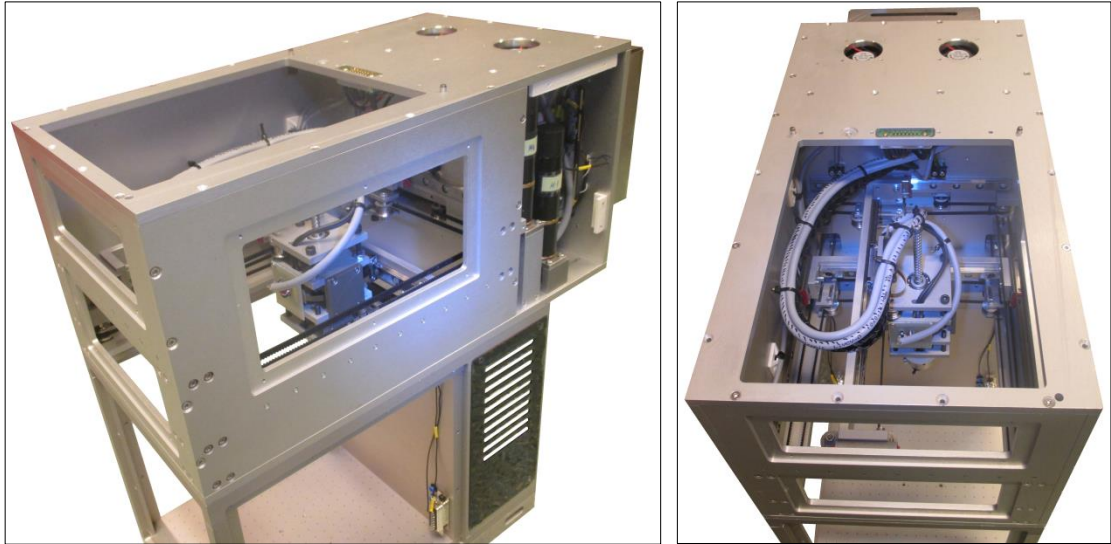
Figure 8-7 Two different perspectives of the DOHMAN robot prototype while being attached onto the base module

In similar fashion, Figure 8-8 illustrates the CVM from two different perspectives.

Figure 8-8 Two different perspectives of the CVM

APPENDIX 11: MODULES' INTERFACING

The interfacing among the modules is embraced from three different aspects, i.e. mechanical, electrical and pneumatic. However, since the latest one is not applied in this case, it will not be examined. The mechanical aspect refers to constraining the movements in two direction of one module in respect to the other one, e.g., for stack interfacing in *X* and *Y*. The electrical aspect refers to signal and power supply interfaces among the modules, meaning easy plug and play secure transfer of signals and electric current. The interfacings of the connectors also provide locking of the third axis (Z axis in case of stacking arrangement).

Two dowel pins (φ=4 x 16 *mm*) are fitted in 3D printed cavities and glued to the top plates of DOHMAN and base module, red circle on Figure 8-9.
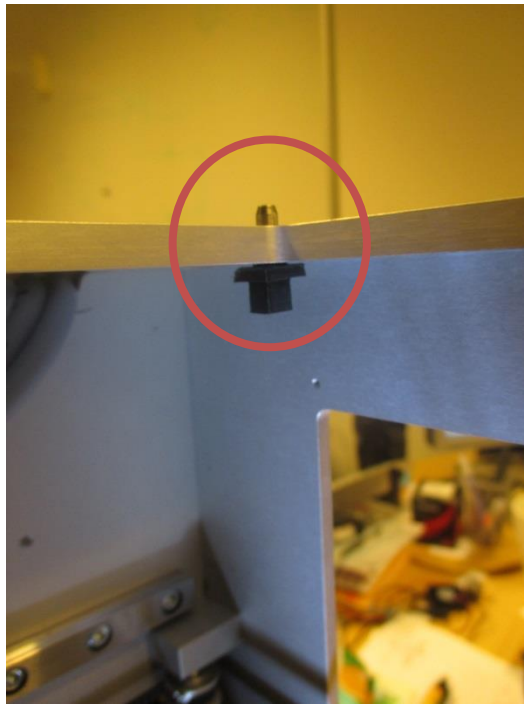
Figure 8-9 Dowel pin attached to the top PM plate

In the electrical linkage, the signals and current are carried to DB-17W2 connectors. Signals are passing through the smaller pins and current through the bigger pins: Figure 8-10, colored in orange ellipse illustrates male DB-17W2 connector.

Figure 8-10 Interface area of the top PM plate

When interfacing, the dowel pins are entering through two holes with tolerance H7; one through hole φ=4 and the other through elongated hole also with φ=4, blue rectangles on Figure 8-11. In addition the small and big pins from the male DB-17W2 connector are going through the female pins of the DB-17W2 connector, green ellipse.
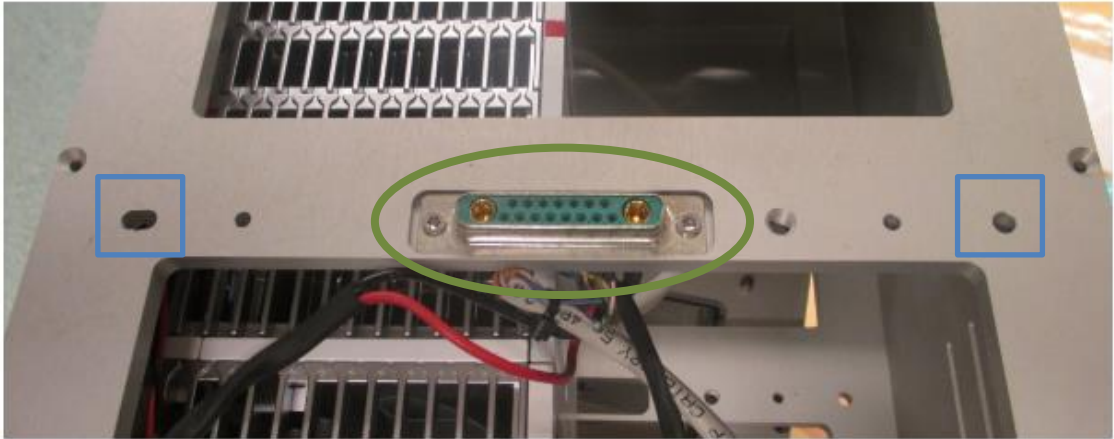
Figure 8-11 Interface area of the bottom CVM plate

An example of interfaced plates is illustrated on the image below.
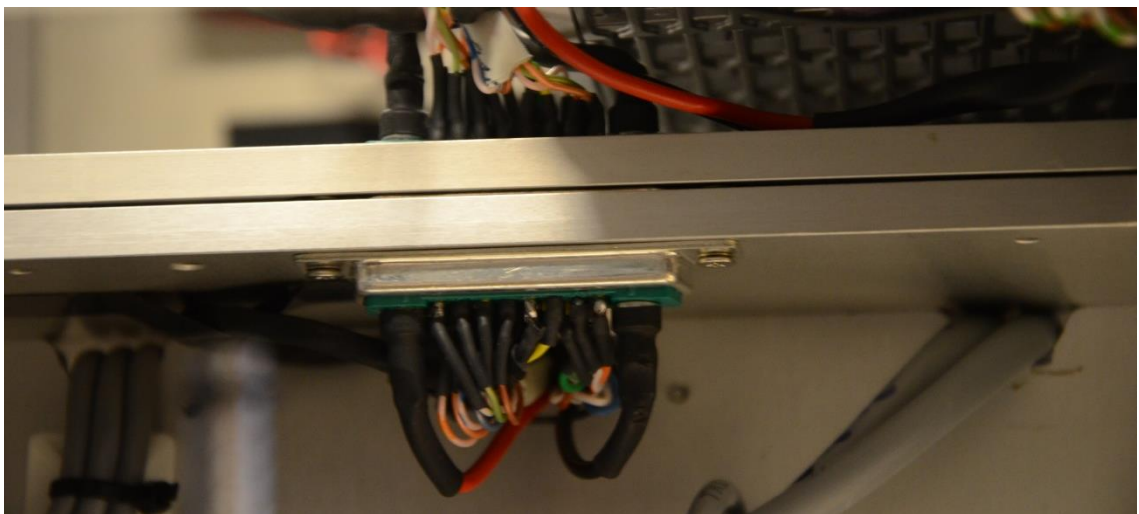
Figure 8-12 Interfaced plates. Top PM plate (down) and bottom CVM plate (up)

APPENDIX 12: WIRING

Figure 11-13 (left) illustrates a dense wiring nearby the motors and their amplifiers as well as within the DOHMAN control unit. The right image on the figure is zoomed portion of the left image and it illustrates notations (red ellipses) used for easier trouble shooting and debugging of the whole wiring arrangement.
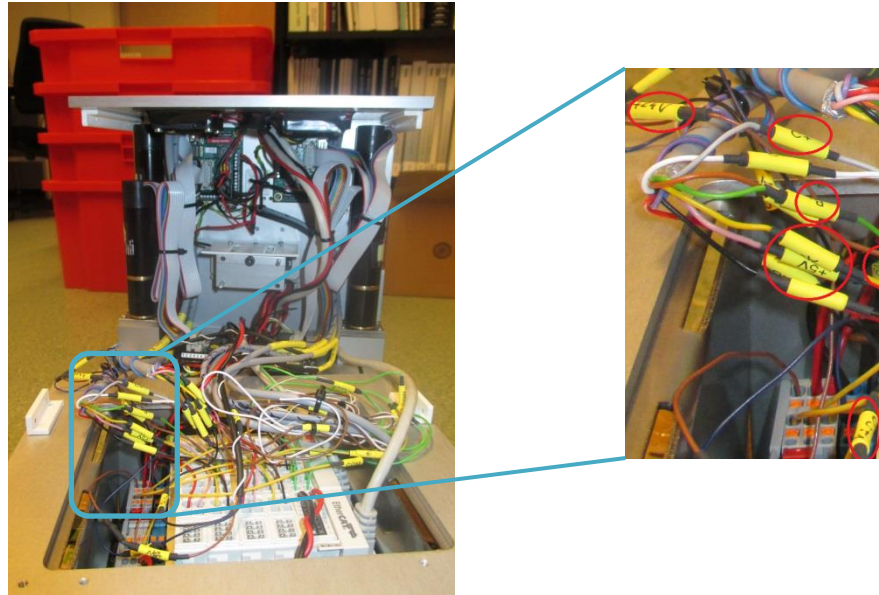
Figure 8-13 Wiring within the DOHMAN

Table 8-5 represents notations, enumerations and color coding of wires and cables of each device and how they are connected to the IO modules. This table is highly recommended to be used while doing certain rewiring, reconnections and/or maintenance work in any of the modules.

Table 8-5 Connections and wiring within CVM, DOHMAN, and base module, respectively.

Module	Function/ Device	Cable/ Wire ID	Wire Color	Module Position	Module Type	Port ID –	Port Number
CV	IO ground	No ID	BU	0	CX2100-0004	-	3
CV	IO ground	No ID	BU	0	CX2100-0004	-	7
CV	Ctrl ground	No ID	BU	0	CX2100-0004	0V	5
CV	IO supply	No ID	RED	0	CX2100-0004	+	2
CV	IO supply	No ID	RED	0	CX2100-0004	+	6
CV	Ctrl supply	No ID	RED	0	CX2100-0004	24V	1
CV	PE	No ID	YE/GN	0	CX2100-0004	PE	4
CV				0	CX2100-0004	PE	8
CV	Camera			-1	CX2100-0070	USB 3.0	1
CV				-1	CX2100-0070	USB 3.0	2
CV				-1	CX2100-0070	USB 3.0	3
CV				-1	CX2100-0070	USB 3.0	4
CV	E-stop button	W1	GY	1	EL1819	I1	1
CV	Reset button	W1	VT	1	EL1819	I2	2
CV	Start button	W1	PK/GY	1	EL1819	I3	3
CV	Stop button	W1	BK	1	EL1819	I4	4

CV	User button	W1	GN	1	EL1819	I5	5
CV				1	EL1819	I6	6
CV				1	EL1819	I7	7
CV				1	EL1819	I8	8
CV				1	EL1819	I9	9
CV				1	EL1819	I10	10
CV				1	EL1819	I11	11
CV				1	EL1819	I12	12
CV				1	EL1819	I13	13
CV				1	EL1819	I14	14
CV				1	EL1819	I15	15
CV				1	EL1819	I16	16
CV	E-stop light	W1	PK	2	EL2808	O1	1
CV	Reset light	W1	YE	2	EL2808	O2	5
CV	Start light	W1	BU/RD	2	EL2808	O3	2
CV	Stop light	W1	BN	2	EL2808	O4	6
CV	User light	W1	WH	2	EL2808	O5	3
CV				2	EL2808	O6	7
CV				2	EL2808	O7	4
CV				2	EL2808	O8	8
CV				3	EL6751	-	1
CV	CANopen	W2	YE	3	EL6751	CAN L	2
CV	CANopen	W2	BK	3	EL6751	CAN GND	3
CV				3	EL6751	-	4
CV				3	EL6751	Shield	5
CV				3	EL6751	CAN GND	6
CV	CANopen	W2	GN	3	EL6751	CAN H	7
CV				3	EL6751	-	8
CV				3	EL6751	-	9
CV	Supply +	No ID	RD				
CV	GND	No ID	BU				
PM	Ctrl Supply	W10		0	EK1818	24V	1
PM	Ctrl ground	W10		0	EK1818	0V	9
PM	IO Supply	No ID		0	EK1818	+	6
PM	IO ground	No ID		0	EK1818	-	14
PM	I_Limit_X_Pos	W3	GY[5]	0	EK1818	I1	2
PM	I_Limit_X_Neg	W4	GY[5]	0	EK1818	I2	10
PM	I_Limit_Y_Pos	W5	GY[5]	0	EK1818	I3	3
PM	I_Limit_Y_Neg	W6	GY[5]	0	EK1818	I4	11

[5] Limit switches along *X* and *Y* axes have three outputs: COM, NC and NO. The COM port is soldered to yellow wire and it is connected to the GND. In similar way, the NC port is soldered to green wire and connected to the input slot of the EK1818 IO module. The NO port (brown wire) remains as unconnected wire and it is wrapped around the sensor cable.

PM	I_Limit_Z_Pos_L	W7	BK[6]	0	EK1818	I5	4
PM	I_Limit_Z_Pos_R	W8	BK[6]	0	EK1818	I6	12
PM				0	EK1818	I7	5
PM				0	EK1818	I8	13
PM				0	EK1818	O1	7
PM				0	EK1818	O2	15
PM				0	EK1818	O3	8
PM				0	EK1818	O4	16
PM	Linear Encoder *X*	W1	BK	1	EL5101	A	1
PM	Linear Encoder *X*	W1	YE	1	EL5101	A/	5
PM	Linear Encoder *X*	W1	BN	1	EL5101	B	2
PM	Linear Encoder *X*	W1	GN	1	EL5101	B/	6
PM	Linear Encoder *X*	W1	GY	1	EL5101	C	3
PM	Linear Encoder *X*	W1	WH	1	EL5101	C/	7
PM		W1		1	EL5101	Latch	4
PM		W1		1	EL5101	Gate	8
PM	Linear Encoder *X*	W1	PK	1	EL5101	5V	1'
PM	Linear Encoder *X*	W1	RD	1	EL5101	GND	5'
PM				1	EL5101	24V	2'
PM				1	EL5101	24V	6'
PM				1	EL5101	0V	3'
PM				1	EL5101	0V	7'
PM				1	EL5101	I1	4'
PM				1	EL5101	Shield	8'
PM	Linear Encoder *Y*	W2	BK	2	EL5101	A	1
PM	Linear Encoder *Y*	W2	YE	2	EL5101	A/	5
PM	Linear Encoder *Y*	W2	BN	2	EL5101	B	2
PM	Linear Encoder *Y*	W2	GN	2	EL5101	B/	6
PM	Linear Encoder *Y*	W2	GY	2	EL5101	C	3
PM	Linear Encoder *Y*	W2	WH	2	EL5101	C/	7
PM		W2		2	EL5101	Latch	4
PM		W2		2	EL5101	Gate	8
PM	Linear Encoder *Y*	W2	PK	2	EL5101	5V	1'
PM	Linear Encoder *Y*	W2	RD	2	EL5101	GND	5'
PM				2	EL5101	24V	2'
PM				2	EL5101	24V	6'
PM				2	EL5101	0V	3'
PM				2	EL5101	0V	7'
PM				2	EL5101	I1	4'
PM				2	EL9011	Shield	8'
PM	Supply +		RD				

[6] Limit switches along *Z* axis have four outputs: +24VDC (brown), GND (blue), OUT1 (black) and OUT2 (white). The brown and black wires are connected to the power supply and the ground lines respectively. The black wire is connected to the appropriate digital input slot of EK1818 IO module and the white wire remains as unconnected and is wrapped around the sensor cable.

PM	GND		BU				
BM				0	EK1100		1
BM				0	EK1100		2
BM				0	EK1100		3
BM				0	EK1100		4
BM				0	EK1100		5
BM	LED stripes	No ID	Yellow sticker	1	EL2004	O1	1
BM	LED stripes	No ID	Yellow sticker	1	EL2004	O1	1
BM				1	EL2004	O2	5
BM				1	EL2004	O3	4
BM				1	EL2004	O4	8
BM				1	EL2004	0V	2
BM	LED stripes	No ID	BK	1	EL2004	0V	2
BM	LED stripes	No ID	BK	1	EL2004	0V	6
BM				1	EL2004	0V	3
BM				1	EL2004	0V	7
BM				2	EL9011		
BM	Supply +	No ID	RD				
BM	GND	No ID	BU				

The color coding shortcuts used in Table 8-5 are according to IEC 60757 and they are shown in Table 8-6, thus:

Table 8-6 Color coding with appropriate shortcuts according to IEC 60757

black	BK
brown	BN
red	RD
orange	OG
yellow	YE
green	GN
blue	BU
violet	VT
grey	GY
white	WH
pink	PK
turquoise	TQ

APPENDIX 13: G-CODE

% DOHMAN External validation
% TUT / MEI / Zoran Cenev, supported and supervised by Niko Siltala
% 27.01.2014

N01 G90 G71 G17
N03 G54   (activates adjustable zero offset shift)
N04 G58 X0 Y0   (programmable zero offset shift)

(Start Position)

N10 G01 Z=50 F=200
N20 G01 X=0 Y=90 Q1=0 F=1200

%--

(Displacements along Y, X, Z and W respectively)

N30 G90   (Absolute positions)
N32 M34   (Lights ON)
N40 G04 X2   (pause in sec)
N45 G01 Y=0 F=1000
N50 G04 X2
N52 G01 X=40 F=1000
N56 G04 X2   (pause in sec)
N58 G01 Z=20 F=200
N62 G04 X2   (pause in sec)
N64 G01 Q1=270 F=1400

%--

(Linear interpolation along XY)

N100 G90   (Absolute positions)
N110 G04 X2   (pause in sec)
N115 G01 X=0 Y=80 F=1000
N120 G04 X2   (pause in sec)
N125 G01 X=40 Y=80 F=1000
N130 G04 X2   (pause in sec)
N135 G01 X=0 Y=0 F=1000
N140 G04 X2   (pause in sec)

%---

(Emulation of Assembly Operation)

% Z and W in home position
N200 G01 Z=50 F=200
N210 G01 Q1=0 F=1200
N250 G04 X3   (pause in sec)

%Pick Position
N300 G01 X=20 Y=10 F=1200
N310 G01 Z=30 F=400
N330 G01 Z=25 F=200
N335 G04 X3   (pause in sec)
N340 G01 Z=30 F=200
N350 G01 Z=40 F=400

%Release position
N400 G01 X=35 Y=50 Q1=90 F=1200
N410 G01 Z=20 F=400
N420 G01 X=40 F=600
N430 G04 X2   (pause in sec)
N440 G01 X=35 F=600
N450 G01 Z=50 F=400

%Start Position
N500 G01 Z=50 F=200
N510 G01 X=0 Y=90 Q1=0 F=1200
N520 G04 X2   (pause in sec)
N600 M35   (Lights OFF)

M30 (program End)
%%

APPENDIX 14: DATA CD

A compact disk CD is enclosed to this thesis and it contains the following:

1. 2D drawing in .pdf and in .CATDrawing file format of each part used for the assembly of DOHMAN and CVM,
2. 3D CAD models in .stp and .CATpart file formats of every part used in each module
3. 3D CAD assemblies in .CATProduct file format
4. .dxf files for each plate manufactured from Plexiglas
5. Excel sheets used in the calculations, product datasheets
6. References
7. Digital format of this Master of Science thesis